The Dissertation Committee for Brendan Francis Murphy Certifies that this is the approved version of the following dissertation:

Dynamics of Noble Gas Cluster Expansion Driven by Intense Pulses of Extreme Ultraviolet Light

Committee:

Todd Ditmire, Supervisor

John Keto, Co-Supervisor

Manfred Fink

Boris Breizman

Michael Becker

Dynamics of Noble Gas Cluster Expansion Driven by Intense Pulses of Extreme Ultraviolet Light

by

Brendan Francis Murphy, B.A.

Dissertation

Presented to the Faculty of the Graduate School of
The University of Texas at Austin
in Partial Fulfillment
of the Requirements
for the Degree of

Doctor of Philosophy

The University of Texas at Austin
August, 2009

Dedication

For my parents and family

Acknowledgements

This work is the product of important contributions from many individuals over many years. I would first like to thank Todd Ditmire for his generosity in sharing expert knowledge directly relevant to every aspect of this thesis, for providing an excellent laboratory environment, and for providing opportunities to collaborate with top notch researchers worldwide in the study of laser-plasma physics. I would like to thank John Keto for sharing detailed skills necessary to perform experiments involving VUV and XUV light, molecular beam sources, and vacuum systems; also for his unflagging enthusiasm for hands-on laboratory work. I would especially like to thank Kay Hoffmann for his kindness, generosity, and dedication to finding creative solutions to laboratory challenges. Kay's sharp insight and tireless pursuit of good data has been an inspiration during my time at UT. I would like to thank Ditmire group members past, present, and future for contributing to the team effort which makes a laboratory of this quality possible.

Most of the equipment used in the experiments presented here was fabricated in the UT Physics Machine Shop, under the expert guidance of Allan Schroeder. I would like to thank Allan, Danny Boyd, Jack Clifford, Terry Cole, Roger Neideffer, Donnie Cannon, Jesse Trevino, and George Sandefur for their contributions to the fabrication of experiment apparatus. I would like to thank Lanny Sandefur and Ed Baez for assistance

with the many vacuum systems associated with this work. I would like to thank Gary Thomas and Robert Hasdorff for helping to resolve problems with electronic components.

I would like to thank Mike Downer for teaching an excellent laser physics course. I would like to thank Paul Bolton for recommending UT's physics program. I would like to thank the Stanford Linear Accelerator Center for inspiring dedication to experimental physics. I would like to thank David J. Griffiths for making mathematical physics exciting. I would especially like to thank Charlie Camp for making physics an outdoor activity. I would like to thank my parents for encouraging a lifelong interest in science. Finally and most importantly I would like to thank Hyein; without her support this work would not have been possible.

Dynamics of Noble Gas Cluster Expansion Driven by Intense Pulses of Extreme Ultraviolet Light

Publication No._____________

Brendan Francis Murphy, Ph.D.
The University of Texas at Austin, 2009

Supervisor: Todd Ditmire
Co-Supervisor: John Keto

The interaction of intense laser pulses with nanometer scale atomic clusters has been an active area of study since the advent of amplified femtosecond lasers. In the case of infrared irradiation of noble gas clusters, direct field-driven ionization results in the ejection of energetic electrons, high ion charge states, and Coulomb explosion of the ion core of the clusters. These processes result from electron motion driven by the cluster potential and the large ponderomotive potential of the laser field. When extreme ultraviolet (XUV) pulses interact with clusters, the mechanisms responsible for the infrared response are 'turned off' because the ponderomotive potential is very small.

We have conducted cluster experiments at 38nm using focused XUV pulses produced by high harmonic generation with a 15TW Ti:Sapphire laser. We measured the charge states and kinetic energy spectra of ions produced in the interaction, and observe

substantial ion population up to Xe^{5+}, with a small number of Xe^{6+}-Xe^{8+} ions produced by collisional ionization by hot plasma electrons. The ion kinetic energy spectrum indicates a hydrodynamic expansion at an ion temperature of 8eV. This is in stark contrast to intense infrared/cluster interactions, where clusters are stripped of electrons to a large degree and expand by Coulomb forces, resulting in far higher ion kinetic energy for similar degrees of ionization.

Table of Contents

List of Tables

List of Figures

Chapter 1: Introduction

Prior to the development of intense, coherent light sources, human experience with optical phenomena was limited to a linear regime, where the optical response of material is proportional the intensity of the applied light. The advent of lasers in 1960 was followed the next year by the first demonstration of a nonlinear optical effect, the 'gluing together' of red photons to make blue photons in a quartz crystal [1,2]. The focused intensity of the laser in the quartz crystal in the latter experiment was about 10^7 W/cm^2, or roughly 10^8 times the intensity of the sun at noon on earth's equator. The process by which the photons are glued together in that experiment is physically described by a weak perturbative Hamiltonian (the laser field) added to the intrinsic Hamiltonian of the quartz medium. In the perturbative regime, the intensity of the second order response scales with the square of the intensity of the fundamental laser light, the third order with I^3, and so on, and calculating the quantum mechanical responses of simple systems is fairly straightforward using the static basis states of the system. Early laser science explored the perturbative regime, limited mainly by the laser technology available.

In the last twenty years, pulsed optical and near-infrared lasers have advanced dramatically in pulse energy and spectral bandwidth, allowing production of pulses of one to one hundred Joule energy and pulse duration of tens to hundreds of femtoseconds [3,4]. When such a pulse is brought to a focus, the laser electric field strength can easily overwhelm the electric fields binding together ordinary matter, resulting in responses strongly influenced or even dominated by the laser field. At these high intensities electrons are ionized from neutral atoms, allowing production of interesting plasmas in a laboratory setting.

As the intensity of the laser field increases, the mechanisms involved in laser-matter interactions vary. Two useful parameters help determine what models best explain the observed physics: the ponderomotive (or quiver) potential and the Keldysh parameter. The ponderomotive potential U_p (1.1) describes the average kinetic energy of a free electron in laser's oscillating electric field, defining distinct regimes of laser-matter interaction.

$$U_p = \frac{e^2 E_0^2}{m_e \omega_l^2} \qquad \text{(SI units)} \qquad (1.1)$$

When U_p is small with respect to the laser photon energy $\hbar\omega_L$, linear or perturbative processes will dominate. In the opposite extreme, when U_p exceeds $\hbar\omega_L$ and approaches the electron rest mass, relativistic effects are important[1]. In the region between, U_p crosses the ranges of atomic binding potentials, and various forms of non-perturbative nonlinear optical effects occur including high harmonic generation, generation of multiply charged ions, x-ray production, and generation of plasmas capable of supporting deuterium fusion [5-12]. In this intermediate regime, the laser field does not completely suppress the atomic potential, but reduces it enough to allow a significant fraction of electrons to tunnel through the Coulomb barrier during a single laser cycle. An estimate of the rate of tunneling rate proposed by Keldysh based on the average time an electron in the unperturbed atom would take to traverse the potential barrier accurately models the observed thresholds for tunnel ionization [13, 14]. For an atom or ion with

---

[1] All physical processes considered in this work are nonrelativistic, so the relativistic case is not addressed.

ionization potential I_p, the Keldysh parameter γ is the ratio of laser frequency ω_l to the instantaneous tunneling rate given by:

$$\gamma = \omega_l / \omega_t = \sqrt{I_p / 2U_p} \tag{1.2}$$

If both $\hbar\omega_l$ and U_p are much less than I_p ($\gamma >> 1$), electrons and ions are produced by multiphoton absorption, which is described by the same perturbative quantum mechanics as second harmonic generation in quartz. Ignoring energy levels other than the ground state and ionization limit, ionization occurs via the simultaneous absorption of N_{min} photons of energy $\hbar\omega_l$, where N_{min} is the lowest integer such that $(N_{min}\hbar\omega_l) > I_P$. For isotropic materials, only processes involving the absorption of odd numbers of photons are allowed by angular momentum conservation. For anisotropic materials (crystals lacking inversion symmetry, interfaces) both odd and even ordered processes are allowed.

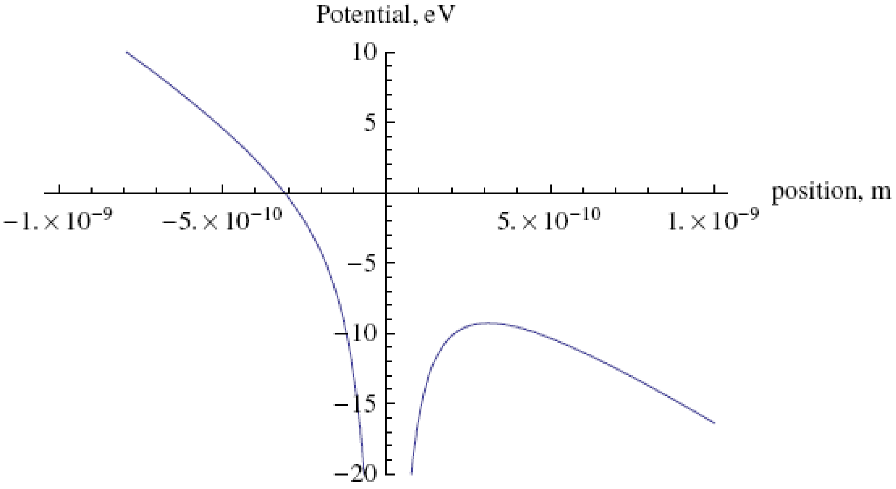

Figure 1.1: Distortion of the atomic potential by the laser field. The finite barrier to the right of the figure makes tunneling possible.

When γ approaches one, the perturbative model no longer holds. The applied electric field distorts the atomic potential enough that an electron has a significant chance of tunneling through the Coulomb potential into the continuum during each laser cycle (Fig. 1.1). This mechanism, distinct from multiphoton ionization, is characterized by the observation of electrons with kinetic energies above ($N_{min}\hbar\omega_l$-I_P), and is termed 'above threshold ionization' (ATI) or tunneling ionization [14, 15]. After being ionized, an electron gains energy from the laser field, and may return to the parent ion after the laser field reverses sign. Recombination of these electrons with their parent ions can produce odd harmonics of the laser field of very high order, in a process called high harmonic generation (HHG) which is described well by a three-step model [16, 17]. Harmonics produced by this process have an intensity dependence 'plateau' where the intensity of harmonics is relatively flat across many orders, with the single atom response scaling as $(I_{laser})^{5\text{-}8}$. Scaling this single atom response to macroscopic harmonic production requires consideration of the interaction of the laser pulse with the background plasma accumulated during the pulse propagation. Phase-matching and scaling can increase the photon yield in HHG, providing compact sources of high intensity extreme ultraviolet (XUV) pulses [18, 19].

In extended targets composed of clusters of 10-10^6 atoms, collisions become significant, and processes besides ATI and HHG must be considered. If the laser field is strong enough, all electrons can be tunnel-ionized from the target, which subsequently explodes by the Coulomb forces on the ions. For large clusters (or slightly lower intensity) and $\gamma \approx 1$, rescattering tunnel-ionized electrons rapidly thermalize the electron population, and the high energy tail of this population escapes the cluster, increasing the net cluster charge until the cluster Coulomb potential is comparable to U_p. This allows efficient coupling of energy from the laser field into the electrons and ions at high intensity, and is associated with production of keV x-rays and electrons, and up to MeV ion energies resulting from the Coulomb explosion of the partially charged cluster [9]. Researchers have studied laser-cluster interactions with near infrared to near ultraviolet lasers extensively (fig. 2). For optical laser fields, the ponderomotive potential is the dominant factor in weighting the physical processes which describe the laser-cluster interaction.

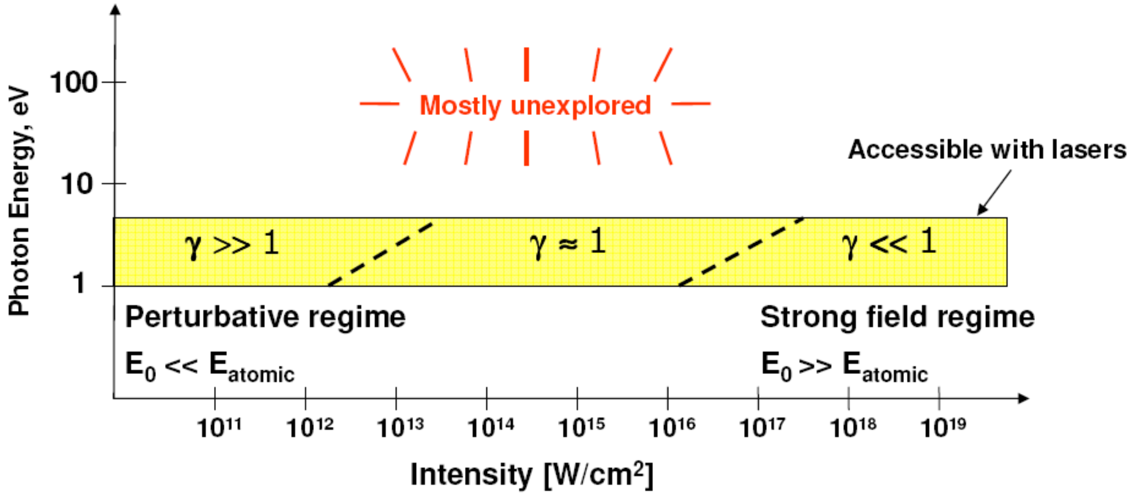

Figure 1.2: Regimes of high intensity laser-matter interactions.

The response of clusters to short wavelength radiation differs dramatically from the optical response. If the intensity is held constant while the laser photon energy is increased, the ponderomotive potential vanishes as $(\hbar\omega_l)^{-2}$. Electrons are no longer directly accelerated by the ponderomotive force, and the degree of cluster ionization is reduced. Single photon ionization is the dominant absorption process when $\hbar\omega_l > I_p$, but for sufficiently short pulse durations and high intensities, the cluster environment may change enough during the pulse that the ionization potential I_p (and absorption cross-section) differs significantly from standard values. A major motivation to study the physics of intense short wavelength interactions with clusters relates to diffraction-imaging of isolated biomolecules by x-ray free electron lasers [20-22]. A better understanding of the coupling of energy from the light pulse to the atoms and electrons in large clusters will provide needed information about the motion of biomolecule atoms during the x-ray exposure.

Experiments involving the interaction of intense short wavelength light with matter can supply data in a regime where until recently almost none existed. This work reports on observations of intense XUV-cluster interactions using high harmonics produced by UT's THOR laser. Chapter 2 explores the physics of HHG with the aim of developing intense XUV pulse sources suitable for XUV-cluster experiments. Chapter 3 describes the design and operation of the THOR laser, including modifications relevant to the harmonics experiment. Chapter 4 discusses the construction and performance of the HHG beamline producing intense XUV pulses. Chapter 5 discusses the results of experiments involving the response of xenon and argon clusters to XUV light at intensities where nonlinear effects occur. Mathematica and Matlab codes used for analysis are included as Appendices A-D.

Chapter 2: High Harmonic Generation

In order to perform XUV-cluster experiments, we first need a source of intense XUV pulses. This chapter discusses the physics of atomic media interacting with laser pulses at ponderomotive energies of the same order as the atomic binding potential, focusing on the generation of XUV harmonics of the laser field. In particular, the interaction of intense near-infrared pulses with argon is modeled, though the approach presented is valid for other noble gases. The classical model of electron trajectories contributing to high harmonic generation is considered in the single-atom case. Optimization of harmonic yield by quasi-phase matching is introduced. Ionization-induced blueshifting of the fundamental laser frequency is modeled using the instantaneous ADK ionization rate. The dependence of the spatial and angular distribution of harmonics on the fundamental laser parameters is explained for low and high order processes. Off-axis phase matching conditions relevant to harmonic generation using annular beams are detailed. Time-dependent spectral structure of the harmonic radiation and the potential of forming attosecond pulse trains by XUV compression in thin films is considered.

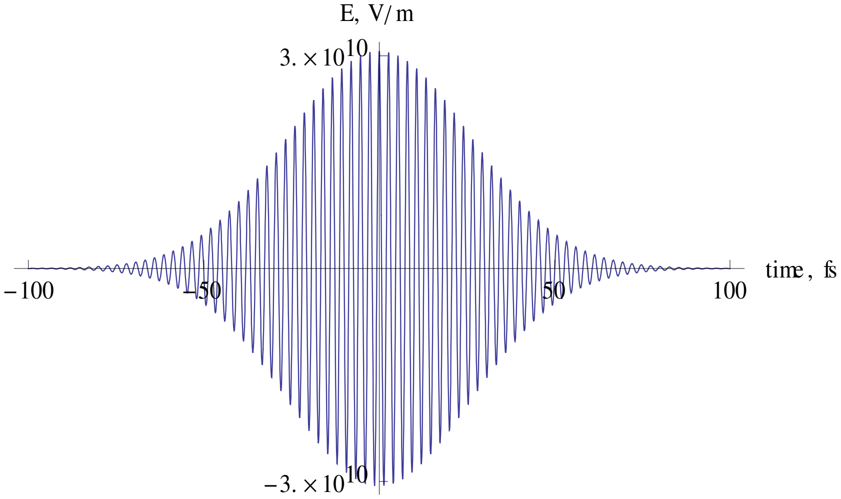

Figure 2.1: Electric field of a 37fs FWHM laser pulse at 5x10^{14} Wcm^{-2} peak intensity.

2.1 Above threshold ionization and high harmonic generation

When the laser pulse duration is sufficiently short and the intensity sufficiently high (see fig.1), multiphoton ionization no longer describes the dominant ionization process. In the nonperturbative regime, the electric field of the laser pulse suppresses the atomic potential enough that an electron can tunnel through the reduced barrier into the continuum. This tunneling was described for hydrogenic atoms by Keldysh and later for complex atoms by Ammosov, Delone, and Krainov (ADK) [13, 14]. Electrons produced by ATI can radiatively recombine with their parent atoms after gaining energy from the laser field, resulting in high harmonic generation. Numerical modeling of the HHG process helps establish the parameters required for optimum harmonic generation.

Averaged over angular momentum states, the ADK ionization rate for a single atom is:

$$w(t) = \frac{I_p}{\hbar} \left| C_{n^*} \right|^2 \left(\frac{4 I_p}{\hbar \omega_t} \right)^{2n^* - 1} \exp\left[- \frac{4 I_p}{3 \hbar \omega_t} \right] \tag{2.1}$$

where

$$\omega_t = \frac{e \mathrm{E}_L(t)}{(2 m_e I_p)^{1/2}}$$

$$n^* = Z \left(\frac{I_H}{I_p} \right)^{1/2}$$

$$\left| C_{n^*} \right|^2 = \frac{2^{2n^*}}{n^* \Gamma(n^* + 1) \Gamma(n^*)}$$

At the peak of a cosine-like laser pulse, the ADK rate can be stated in terms of the laser frequency and the ponderomotive potential:

$$w(t) = \frac{I_p}{\hbar} \left| C_{n^*} \right|^2 \left(\frac{2^{5/2} I_p^{3/2}}{\hbar \omega_L \sqrt{U_p}} \right)^{2n^* - 1} \exp\left[- \frac{2^{5/2} I_p^{3/2}}{3 \hbar \omega_L \sqrt{U_p}} \right] \tag{2.2}$$

Values of the peak ADK ionization rate for the laser pulse shape shown in Fig.1 are plotted versus the ponderomotive potential in Fig. 2, illustrating the sharp onset of above threshold ionization.

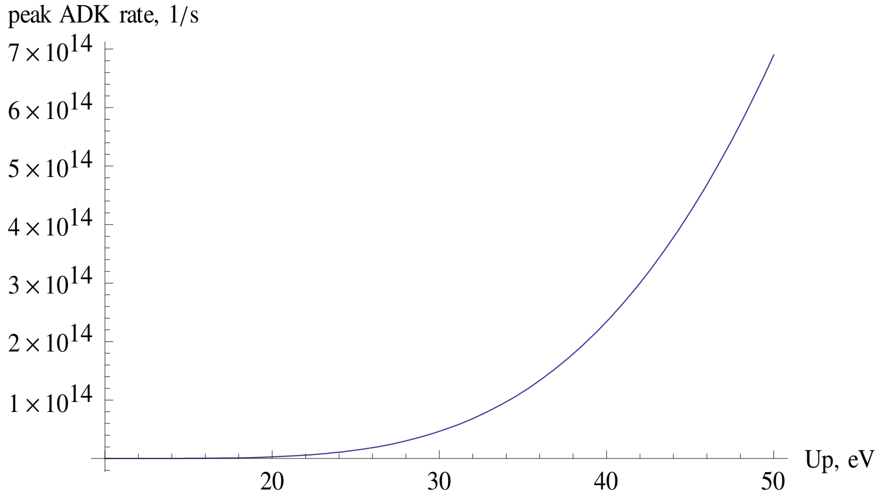

Figure 2.2: ADK tunneling ionization rate versus ponderomotive potential U_p for argon at 1.55eV photon energy and 37fs pulse duration

The ADK ionization rate for argon gas in the laser pulse of Fig.1 is roughly $5x10^{13}s^{-1}$, resulting in 18% ionization of the argon by the end of the pulse.

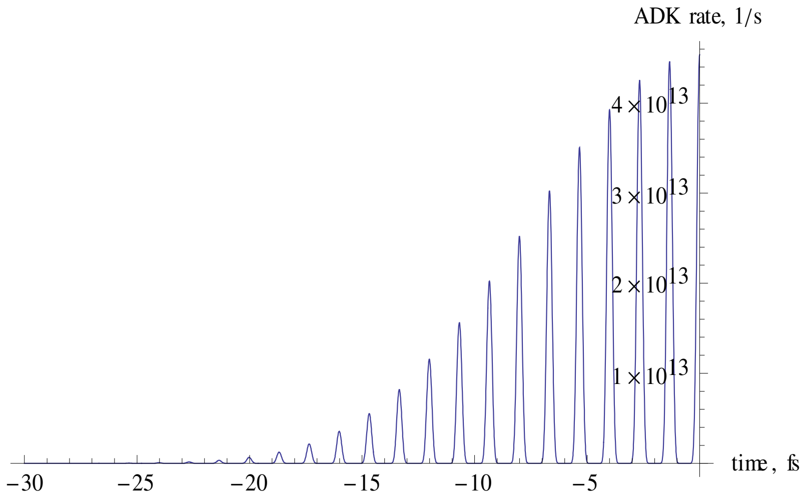

Figure 2.3: Time dependent ADK rate of Ar in the laser field from Fig. 2.1

2.2 Recombination times for ATI electrons

When an atom is tunnel ionized, an electron is ‘born’ into the continuum states at some phase of the laser electric field, which will determine its fate. After launch into continuum, ADK electron motion can be accurately modeled classically [17]. The equations of motion of the electron in the laser field are:

$$m\frac{d^2x}{dt^2} = -eE_0\cos(\omega t) \tag{2.3a}$$

$$\frac{dx}{dt} = \frac{eE_0}{m\omega}\left(\sin(\omega t) - \sin(\omega\tau)\right) \tag{2.3b}$$

$$x(t) = \frac{eE_0}{m\omega^2}\left(\cos(\omega t) - \cos(\omega\tau) + \omega\sin(\omega\tau)(t-\tau)\right) \tag{2.3c}$$

Electrons ionized from two distinct laser phases can recombine with their parent ions after either a ‘short’ or a ‘long’ excursion in the continuum. Recombination occurs only when the electron-ion distance is zero, at which time the electron has some kinetic energy depending on its launch phase. This necessary condition can be expressed as follows:

$$K_1 = 2U_p\left(\sin(\omega t_r) - \sin(\omega\tau)\right) \tag{2.4a}$$

$$K_2 = \cos(\omega t_r) - \cos(\omega\tau) + \omega(t_r - \tau)\sin(\omega\tau) \tag{2.4b}$$

An electron returns to its parent ion with kinetic energy K_1 when K_2 is zero. Figure 4 shows the electron kinetic energy upon return to its ion as a function of launch and recombination times. Not all launch and recombination times are physically realized in the interaction- the global maximum of the kinetic energy, for example, occurs for an electron which is ionized when the laser field zero, an unrealistic picture. Half the electrons ionized never return to their parent ion. Figure 5 plots the electron position as a function of launch and recombination times, in units of ponderomotive length. K_2 displays a saddle point near the middle of the plot, with two paths along which $K_2 = 0$.

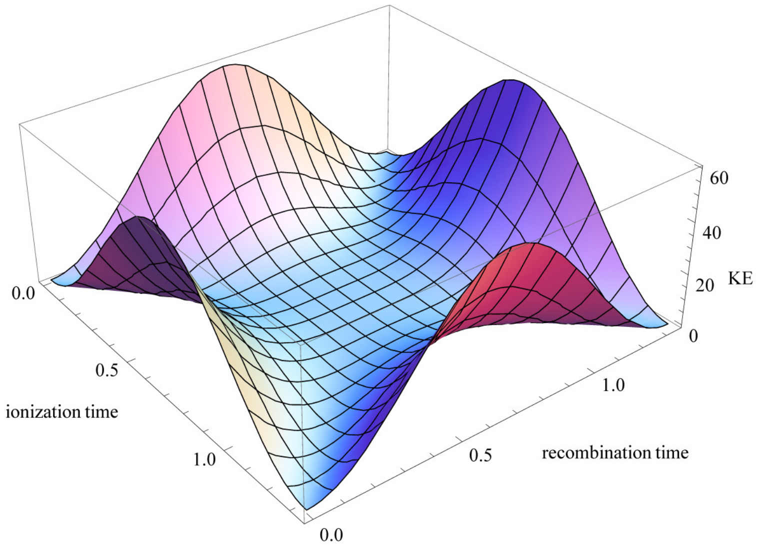

Figure 2.4: Electron kinetic energy on return vs. ionization and recombination time plotted over half a laser period. KE is in eV; times are in femtoseconds.

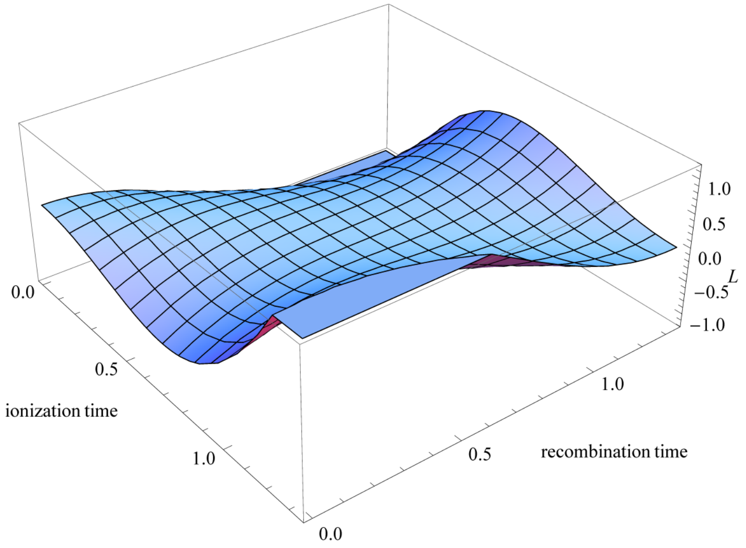

Figure 2.5: Electron position relative to parent ion verses ionization and recombination time. Units of L are ponderomotive lengths; times are in femtoseconds.

Plotting the two functions together helps clarify the ionization and recombination times which contribute to HHG. Figure 6 is an overlay plot of K_1 and $1/(K_2^2 + \delta^2)^{1/2}$ above, to illustrate where K_{two} passes through zero[2]. The broad ridge where the ionization time equals the recombination time corresponds to zero kinetic energy, and therefore zero HHG. The narrower ridge represents the electron trajectories contributing to HHG. The 'short' and ' long' trajectories correspond to the portions of the narrow ridge above and below the broad ridge, respectively. The maximum kinetic energy with which the electron can return to its parent ion is $KE_{max} \approx 3.17 * U_p$; these recombination events lead to the cutoff frequency of the high harmonics $\hbar\omega_{max} \approx I_p + 3.17 * U_p$. This maximum occurs on the ‘short’ trajectory side.

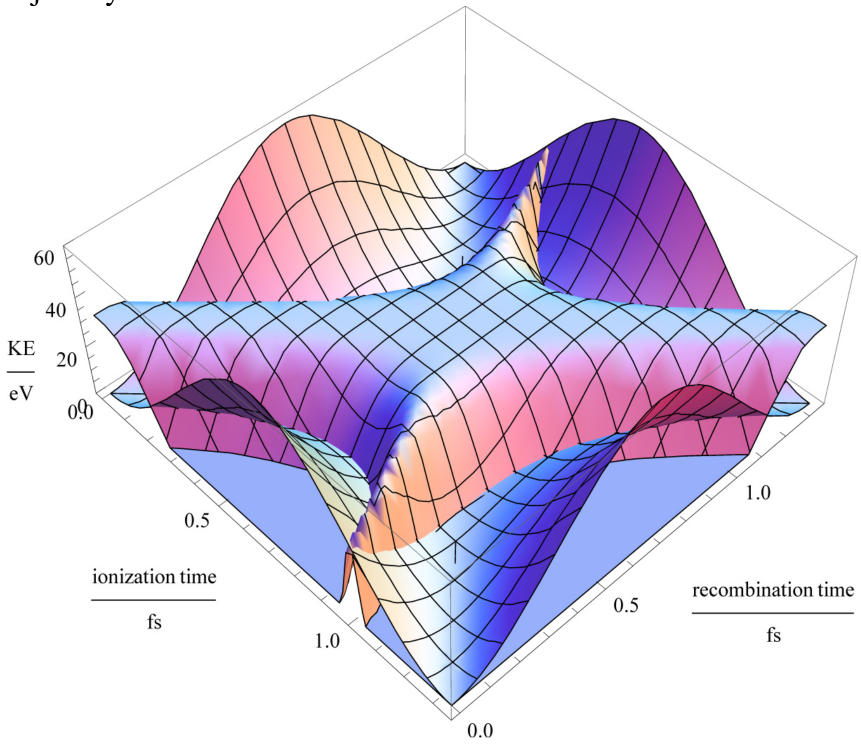

Figure 2.6: Electron trajectories contributing to HHG in argon with the laser pulse from Fig 2.1. The inverse of the electron-ion distance shows paths involved in HHG.

---

[2] δ is a small parameter to keep $1/K_2$ from diverging near zero

2.3 Quasi phase matched HHG

Scaling HHG from the single-atom response to macroscopic systems involves tracking the infrared and harmonic phase. The harmonic signal will grow as the square of the interaction medium length if the mismatch is kept to zero. The phase of the laser field results from geometrical factors, the nonlinear dipole response of the atoms in the HHG gas, and the plasma generated by the laser:

$$\varphi(q) \sim \varphi_{Gouy}(q\omega) + \varphi_{nl}(q\omega) + \varphi_{plasma}(q\omega) \qquad (2.5)$$

$$\Delta\varphi \equiv \varphi(\omega) - \varphi(q\omega)$$

2.4 Gouy phase

The first term, the Gouy or geometrical phase, is given for the infrared field by

$$\varphi_{Gouy}(\omega_L) = Tan^{-1}\left(z/z_R \right) \qquad (2.6)$$

Where z_R is the Rayleigh range of the infrared focus:

$$z_R = \pi\lambda(f/d) \qquad (2.7)$$

The Gouy phase [23, 24] varies rapidly in the range [-zR , zR] and quite slowly outside this range. Foreseeing that we will put the hhg medium well outside the focus, we will be in the slow-variation range. For the harmonics, the Gouy phase variation away from the focus is negligible. The sign of the Gouy phase mismatch is negative when the HHG medium is placed before the laser focus, and positive when the HHG medium is placed after the focus.

2.5 Intensity dependant dipole phase

The second term in (2.5) results from the nonlinear dipole polarizibility of the atomic medium [25-30]. This term results in a ‘slowing’ of the infrared wave, and therefore always negative, as the phase of the fundamental lags behind the harmonic phase. The nonlinear dipole’s effect on the harmonics is negligible in all cases. Balancing the Gouy mismatch with the nonlinear dipole mismatch has been used to phase-match harmonics by placing the harmonics medium after the infrared focus [27], but is a valid approach only when the ionization level is low. At high intensities (above single-ion saturation,) the nonlinear dipole phase dominates the Gouy phase mismatch, leading to the infrared phase lagging behind the XUV phase as the harmonics propagate through the generating medium. Obtaining quantitative estimates of the nonlinear dipole phase for specific experimental geometry is a formidable task, because the propagation of the infrared light is strongly influenced by nonlinear effects in the HHG gas.

2.6 Integrated plasma effects on infrared propagation

The last term in (2.5) results from the influence of plasma accumulated during the laser pulse. The index of refraction of plasma is less than one, meaning that phase velocity is increased from vacuum:

$$n_p = \sqrt{1-\left(\omega_p(t)\right)^2/\omega^2} \approx 1 - \frac{e^2}{2\varepsilon_0 m_e \omega_L^2} n_e(t) \tag{2.8}$$

$$\Delta\varphi_{plasma} \approx qt\left(\frac{e^2}{2\varepsilon_0 m_e \omega_L}\right)n_e(t) \tag{2.9}$$

Where the approximation is valid for $\omega >> \omega_p$. Again the influence on the phase of the high harmonics is negligible. When the HHG medium is ionized significantly during the laser pulse, the plasma index of refraction will decrease during the pulse, leading to a positive contribution to the phase in (2.5).

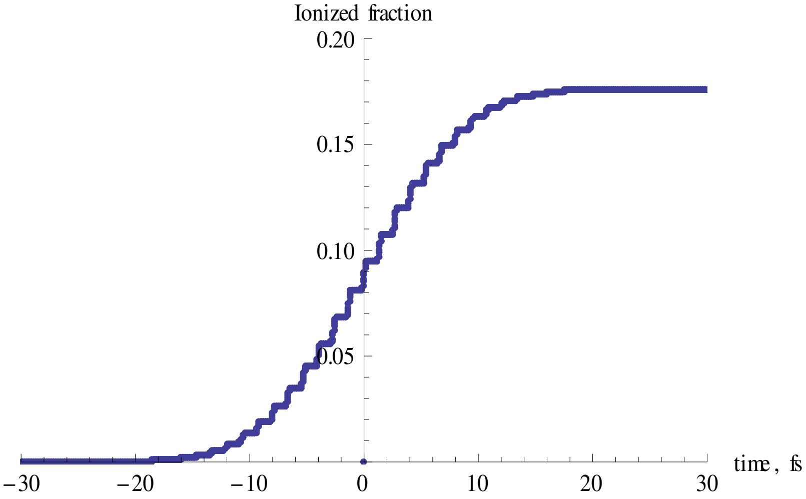

Figure 2.7: Ionized fraction of Ar atoms as a function of time for the pulse in Fig. 2.1.

Placing the HHG medium before the focus allows the balancing of the plasma term by the Gouy and nonlinear dipole terms at some time during the pulse, leading to transient phase matching of the harmonic production. At high intensity, this occurs on the leading edge of the pulse, and tends to suppress harmonic production late in the pulse when the plasma contribution to the phase mismatch becomes large.

2.7 Quasi-phase matching by HHG medium longitudinal position

When the phase matching condition is nearly met, the intensity of the qth harmonic depends on the wave vector mismatch integrated over the length of the harmonic generating medium:

$$N_q \propto \left| \frac{\sin(\Delta k L)}{\Delta k L} \right|^2 \; ; \; \Delta k \equiv k(q\omega) - qk(\omega) \tag{2.10}$$

In practice, all contributions to phase mismatch should be minimized- in the general sense this improves the odds for good phase matching, given that the nonlinear dipole and plasma contributions to phase mismatch are time-dependent. If the total phase mismatch assumes a value close to π/2 during a cycle of the laser pulse, the resulting harmonic yield during that cycle will be poor. Transient phase matching can be used to isolate single attosecond pulses, but it tends to impair the overall harmonic energy. [31]

2.8 Ionization blueshift effect on the laser pulse

Traversing ionizing plasma also induces a blueshift on the laser pulse proportional to the instantaneous ionization rate [32], which is plotted in Fig. 2.8. The blueshift can be kept small by increasing the interaction length while maintaining a constant length-pressure product. The effect of the infrared blueshift is maximum when the ADK rate is highest, corresponding to electrons which do not contribute to HHG; this reduces the impact of ionization blueshift on the harmonic spectra. Blueshifting of harmonics has been observed [33] directly. If the blueshift is large enough, the bandwidth of XUV optics should be considered when planning experiments.

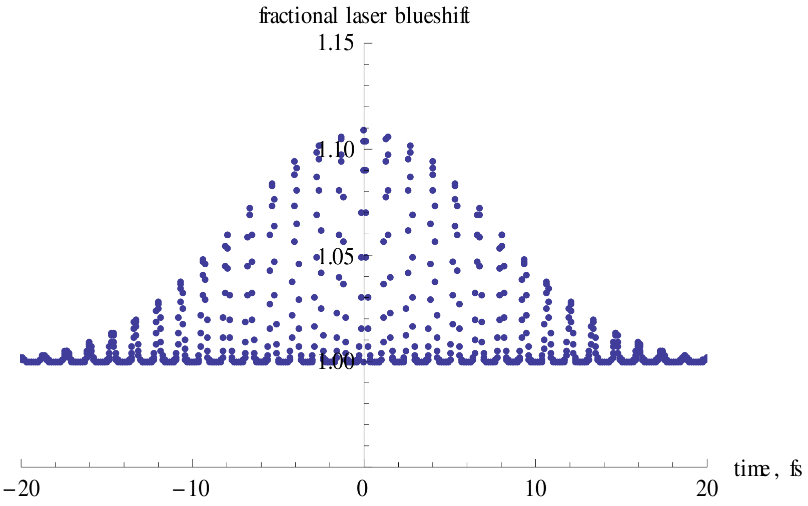

Figure 2.8: Fractional ionization blueshift of the laser pulse in Fig. 2.1 passing through 5mm of argon at 10^{18}/cm^3 density.

2.9 Spatial properties of harmonics

The spatial and angular distribution functions of the harmonics follow a power law similar to the plateau intensity dependence of the harmonic energy [35, 36]. Near the cutoff order, the effective harmonic spot size is given by:

$$\left(\sigma_q\right)_{\bar{r},\bar{k}} = \frac{\sqrt{p}}{q}\left(\sigma_{Laser}\right)_{\bar{r},\bar{k}} \tag{2.11}$$

where $\sigma_{\bar{r}}$ and $\sigma_{\bar{k}}$ refer to spot size and angular divergence, respectively. For the lowest order harmonics, the factor in (2.11) is replaced by $q^{-1/2}$. Because of (2.11), the harmonic beam tends to diverge very slowly with respect to the fundamental, and can be focused to high intensity due to it’s small effective spot size. The harmonics are transversely coherent, so that the harmonic wavefront tends to smooth out at long distances.

Harmonic Order	Effective Spot size, microns	Angular Divergence, mrad
1	53	20
5	22	8.9
19	7.0	2.6
21	6.3	2.3

Table 2.1: Estimated harmonic divergences and effective spot sizes

2.10 HHG with an annular laser beam; off axis phase matching

The separation of the infrared laser light from the XUV harmonics is a significant impediment to XUV experiments when the infrared focal length is extended. Thin (~100-200nm) self-supporting metal films offer 10-50% transmission in the XUV range and ~10^{-9} transmission in the infrared. These filters are very fragile when made with large apertures, and can be torn if exposed to significant infrared fluence. Placing the filter as far away from the laser focus helps, but puts severe demands on lab space, and risks infrared transmission through pinholes in the filter.

Another separation method employs an annular infrared profile and exploits the forward-scattering bias of the harmonics [37]. A mask in center of the laser beam upstream of the focusing optic produces a dark spot in the center of the laser beam after the HHG jet. The high harmonics are highly collimated in the dark spot. All direct infrared light can be separated from the harmonics, with only indirect scattered light hitting the thin film filter. The scattered light intensity is estimated to be less than 10^{-3} of the total infrared light; with an HHG conversion efficiency of 10^{-6}, using an annular profile and a filter can produce an XUV/IR contrast ratio of 10^6. This contrast can be further improved by baffling and proper choice of XUV mirror materials.

Harmonic production in the annular-beam geometry will be optimized when off-axis phase matching is possible. The best off-axis phase matching conditions occur when the laser beam passes through the harmonic medium before it comes to a focus [27, 38]. An exact analysis of the phase matching conditions for the parameters in this experiment is beyond the scope of this work. The harmonic energy produced is optimized by varying the jet-focus position, the pressure in the jet, the energy in the laser, and the outer diameter of the mask which produces the annular profile.

2.11 Temporal structure of harmonics

The total duration of the HHG pulse is significantly shorter than that of the fundamental infrared laser pulse. The ‘short’ and ‘long’ electron trajectories from section 2.2 result in a series of intensity spikes in the XUV pulse, corresponding to the optimal infrared phases for harmonic production. Modeling the harmonic bandwidth in the plateau as in (2.12),

$$\frac{\Delta\lambda_q}{\lambda_q} \cong \frac{\sqrt{p}}{q}\frac{\Delta\lambda_{ir}}{\lambda_{ir}} \tag{2.12}$$

we see that the bandwidth of the 21st harmonic for an 800 nanometer wavelength laser with 40 nanometer bandwidth is about 0.24 nanometers, corresponding to a bandwidth-limited pulse duration of 9 femtoseconds. As evident in Fig. 2.7, almost 90% of the ionization events occur within the 10 laser cycles around the peak infrared laser intensity.

Blueshifting of the harmonics generates time-correlated bandwidth which can be compressed to produce ~200 attosecond spikes within the pulse train [39]. It has been observed that harmonics produced by the short paths in the plateau have a positive ‘chirp’; the harmonic contributions from these paths diverge less, allowing isolation of these the chirped harmonics by placing an iris in the XUV beam far from the generation point. The group delay dispersion of the Al thin film filter is negative in the spectral region of interest, allowing compression of the spikes in the XUV pulse train from high harmonic generation. The time structure of the harmonics used in the XUV-cluster experiments was not measured directly; based on ionization rate and dynamic phase mismatch modeling, the duration of the 21st harmonic is estimated to be 10 femtoseconds.

Chapter 3: Design of a high harmonic beamline on UT's THOR laser

3.1 High Intensity Lasers for High Harmonic Generation

Chapter 2 examined the laser intensity necessary for optimized high harmonic generation in argon with 37 femtosecond pulses with wavelength centered on 800nm. Now we will consider the design of an XUV high harmonic source producing sufficient energy for XUV-cluster experiments. A variety of laser architectures are commonly used for HHG experiments, but the vast majority are based on chirped pulse amplification (CPA) in titanium doped sapphire (Ti:Al_2O_3 or Ti:sapphire) [3, 58]. In this type of laser, a mode-locked oscillator produces low energy (~nJ) ultrashort (~25fs) pulses at high repetition rate (~100 MHz), which are then 'stretched' to nanosecond duration in a dispersive system (typically a grating stretcher [59].) The pulses are then amplified to milliJoule levels in a multipass or regenerative amplifier, at reduced repetition rate (~10Hz-10kHz).[3] The amplified pulse can then be amplified further, or compressed in a dispersive system designed to exactly compensate the dispersion induced in the stretcher, plus the dispersion contribution propagation through the laser chain. The compressor is often located in a vacuum chamber evacuated to microTorr levels, because nonlinear effects resulting from propagation of the compressed pulse through air can distort the pulse in time and space.

---

[3] Typically, higher repetition rate systems have lower pulse energy, as thermal loading is significant in the laser amplifier stages.

3.1.1 Geometry of Laser Interaction with HHG Gas

To produce harmonics, the compressed infrared laser pulse is then focused into the harmonic medium to achieve the necessary intensity. For sub-milliJoule pulse energies, the laser must be tightly focused to fulfill γ~1. This results in small interaction volumes, and limits the harmonic yield possible. To avoid this limitation, gas-filled capillary fiber waveguides have been employed to increase the laser-gas interaction length [60]. HHG systems employing capillary fibers have produced pulses of ~nJ energy at kHz repetition rate. The capillary fiber geometry has two drawbacks relevant to our interest in performing XUV-cluster experiments. First, the fiber does not allow us to use an annular infrared profile, because it will not couple well to the fiber and the annular profile will not be preserved at the fiber exit. Second, scaling up the input laser energy requires increasing the fiber diameter; the fiber soon is not a waveguide at all, and acts just like a gas-filled tube. Two alternate geometries are more suited to HHG with high energy laser pulses- a quasi-static cell (basically a gas-filled tube, with holes at each end often bored using the laser pulse itself) and a pulsed jet (basically a modified automotive fuel injector supplied with pressurized noble gas.) [18, 19] Both of these approaches allow the annular beam profile desired for isolating the XUV pulse from the infrared. Both approaches can be scaled to use tens of milliJoules of laser energy; such scaling requires weak focusing with long focal length optics, to produce a large volume in which the conditions for efficient high harmonic generation are met.

3.1.2 Harmonic Generation on UT's THOR laser

This chapter addresses the construction of a high harmonic beamline on the Texas High-intensity Optical Research (THOR) laser at The University of Texas at Austin. The beamline design results from optimization of the conditions for harmonic generation on the THOR laser subject to the requirements imposed by XUV-cluster experiments and taking advantage of all of the physical space available for the beamline.

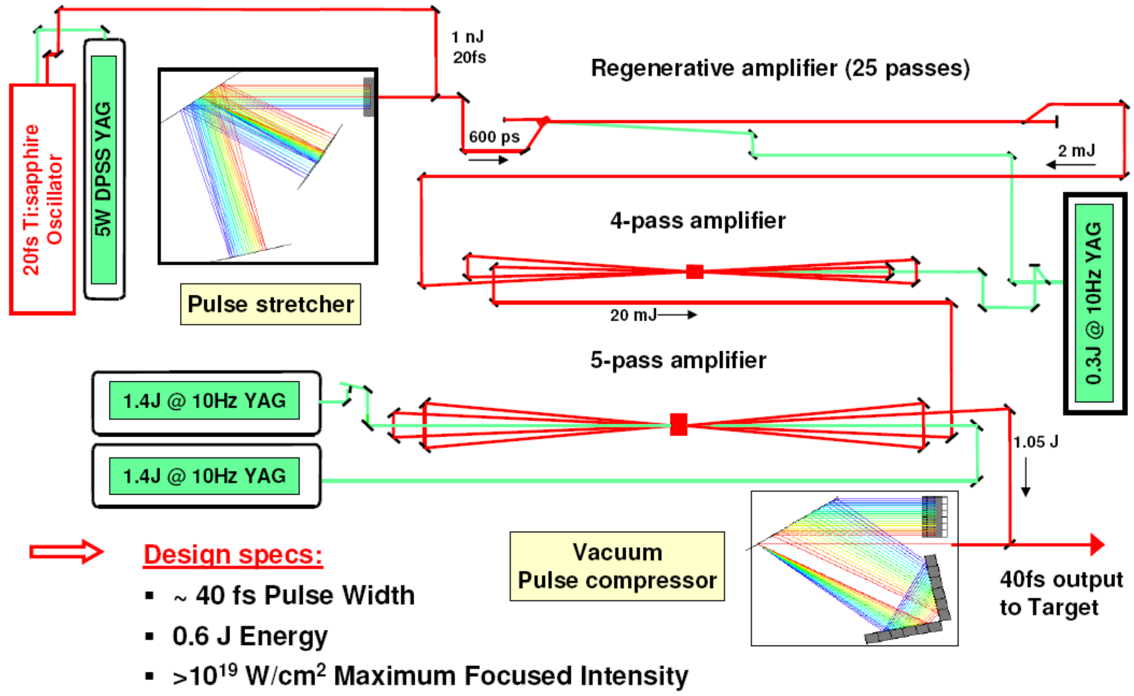

Figure 3.1 THOR laser schematic, including pump lasers, amplifier stages, and stretcher/compressor pair.

3.2.1 Texas High-intensity Optical Research (THOR) Laser

The THOR laser, built in 2001 by the Ditmire group,[4] is based on chirped pulse amplification in Ti:Al_2O_3 capable of producing 0.6 Joule, 37 femtosecond pulses of light centered at 800nm wavelength, at a repetition rate of 10 Hertz (Figure 3.1). A high repetition rate oscillator producing 25 femtosecond pulses provides the broadband seed pulse and the laboratory's base timing clock at 73 MHz. A Pockels' cell and polarizer

---

[4] Primarily Will Grigsby, Greg Hays, Gilliss Dyer, and Todd Ditmire

select pulses out of the oscillator pulse train at 10Hz for amplification. These pulses are then stretched to 600 picoseconds in a folded-path grating stretcher of the Banks-Perry type, based on a gold coated diffraction grating. A length of single-mode fiber compensates the dispersion to 5th order. The stretched 10Hz oscillator pulses then seed a regenerative amplifier with a Ti:Al_2O_3 crystal pumped by 532nm light from a Q-switched Nd:YAG laser, where they are amplified to 3-4mJ. An additional Pockels' cell and multiple polarizers after the regenerative amplifier suppress pre- and post-pulses. The regen output is expanded and relayed to another Ti:Al_2O_3 crystal, pumped by the remainder of the light from the regen pump laser. The laser pulse is passed through the crystal 4 times in a bow-tie geometry multipass amplifier, and amplified to about 20mJ. This output is again expanded and relayed to a second multipass amplifier Ti:Al_2O_3 crystal, pumped on either face by 532 nanometer light from two large q-switched Nd:YAG lasers. The laser pulse passes this crystal 5 times, and is amplified to up to 1.1 Joule pulse energy. This pulse is passed through a vacuum spatial filter to eliminate high spatial frequency features, then it enters a vacuum chamber containing a folded-path grating compressor matched to dispersion the stretcher plus the dispersion of the laser optics. The compressed pulse duration is 37 femtoseconds, limited mainly by gain narrowing in the amplification stages. Extensive modeling and design considerations of the THOR laser are contained in the dissertations of Will Grigsby and Greg Hays.

3.2.2 Oscillator and Timing System

The first element in the THOR laser chain is a Ti: Sapphire oscillator [Femtosource]pumped by a Spectra-Physics Millenia V diode-pumped solid state laser. The pump laser operates in continuous-mode, and delivers ~4.5 Watts of 532 nanometer wavelength light to a small Ti:sapphire crystal within the oscillator's cavity. The oscillator's folded cavity length is set to result in a 73 MHz round trip time for 800 nanometer light. The cavity is mode-locked by the Kerr-lens method. In this technique, the oscillator cavity is first optimized for peak high power continuous wave operation, in which the millions of longitudinal cavity modes are in direct competition for the gain in the laser crystal. In this configuration a few of the most efficient modes will dominate all others, and the cavity modes have no defined phase relationship. The cavity is then intentionally perturbed from this optimized configuration in such a way that a small amount of additional focusing would increase the round-trip cavity gain. This creates an unstable mode configuration, where the mode competition is more democratic. A small jolt to the system from this perturbed configuration (specifically, changing the cavity length for ~1 second then returning it to normal) biases the competition for round-trip gain in favor of those longitudinal modes which can cooperate by having a well defined phase relationship which is stable in time. Once these modes start cooperating, the only way for modes not phase-locked to this longitudinal cavity mode 'team' to survive is to join the team, otherwise they will lose gain to the collective. This modelocking technique produces extremely stable short pulse systems with no active modelocking components, and supports pulse durations down to about 25 femtoseconds when the intracavity dispersion is managed by use of chirped mirrors [62].[5] Once the laser is modelocked, it produces these pulses at the 73 MHz cavity round trip rate (13.7 nanosecond round trip time) with energy up to 720 milliWatts. It is important to note that the group delay dispersion (GDD) introduced by the output coupler is enough to significantly increase the duration of the oscillator pulse. This GDD is very predictable and can be corrected later,

---

[5] A chirped mirror is a multilayer mirror in which the periodicity varies with depth, in order to reflect different wavelengths with different temporal delays. Multilayer mirrors will be further discussed in reference to XUV optics.

however, so preservation of bandwidth is the only requirement for compressibility of the amplified pulse. See figure 3.2 for the oscillator spectrum.

The stability of this oscillator also makes it an excellent clock; therefore it is used as the base timing for the entire laser system. A small portion of the oscillator signal is diverted to a fast photodiode, whose electrical output is diverted to a precise downsampling counter [Medox Twin Peaks] which steps the 73 MHz phododiode signal down to 10 Hz, while maintaining accuracy relative to the oscillator pulses under 1 nanosecond. The 10 Hz output trigger is then supplied to a set of digital delay generators [Stanford Research Systems DG535] which supply all trigger timing to the laser systems, and coarse timing to experiment stations.

3.2.2 Pulse Slicer and Oscillator Isolation

In order to achieve Joule-scale pulse energy at the end of the laser chain, the 73 MHz oscillator pulse train must be reduced to 10 Hz for amplification. This is done by rotating the polarization of selected oscillator pulses by 90 degrees using a fast rise-time Pockels' cell [Lasermetrics 5046SC FastPulse Technologies Inc.] proceeded and followed by high-extinction ratio calcite Glan-Taylor polarizers. Pulses which do not have their polarization rotated are disposed of on a beam dump, while back reflections are suppressed by the gated transmission window of the pulse slicer. A Faraday rotator [EOT Inc.] is installed just before the first polarizer in order to further isolate the oscillator from potential damage by back reflections of the amplified pulse. For alignment purposes, a halfwave plate may be inserted before the Pockels' cell to permit passage of the pulses which are normally dumped; their relatively high average power makes them a far easier alignment reference then the 10 Hz signal.

3.2.3 Stretcher

Ultrashort laser pulses necessarily have broad bandwidth. Because the material dispersion typically varies with wavelength, the phase of different components of the laser pulse spectrum may be delayed or advanced as the pulse propagates through the laser chain, broadening the pulse duration. Careful management of the spectral phase is necessary for the production of femtosecond laser pulses. The spectral phase of the laser pulse can be expanded in a Taylor series:

$$\varphi(\omega) = \varphi_0 + \sum_{n=1}^{\infty} \frac{\beta_n}{n!} (\omega - \omega_0)^n \tag{3.1}$$

The zero order phase term has no effect on the pulse shape. The first order component of the spectral phase determines whether the pulse is cosine-like or sine-like, or something in between. The second order component is the group velocity dispersion (GVD) which describes the rate of accumulated time delay as a function of frequency. Higher order terms are referred to by their order. Correction of the spectral phase contributions of each successive order results in bandwidth-limited pulse duration.

The key to CPA is the stretching of broadband pulses out to long duration prior to amplification, which prevents nonlinear effects from distorting the laser beam or even damaging laser optics. The stretcher employed in the THOR laser is based on the Banks-Perry geometry [59]. This stretcher essentially mirrors the compressor geometry, except that the low intensity of the oscillator pulses allows operation at atmospheric pressures, and an all-reflective M=-1 telescope system inverts the overall dispersion of the system, resulting in path lengths for the ‘red’ end of the spectrum which are shorter than the path lengths for the ‘blue’ end of the spectrum. The 10 Hz pulses from the oscillator, now about 80 femtosecond in duration due to material dispersion, are now stretched to ~600 picoseconds, with the red end of the spectrum leading the blue. The intensity of the pulse is reduced by a factor of order 10^4 in the stretcher, allowing safe amplification to milliJoule levels in the regenerative amplifier.

3.2.4 High Order Phase Compensation by Optical Fiber

The Banks-Perry stretcher geometry allows perfect phase correction up to 3rd order with an all-reflective, single grating compressor. Phase variations of fourth and fifth order are compensated using a length of fiber optic cable whose dispersion characteristics balance the dispersion introduced by the rest of the laser chain. The output of the stretcher is coupled into a silica 4.5 meter polarization-maintaining single-mode fiber. The choice of a 4.5 meter fiber resulted from precise calculations of GDD due to optical elements of the THOR laser by Will Grigsby, with the dispersion model described in detail in his dissertation [61]. The fiber additionally acts as a spatial filter, providing a very smooth Gaussian transverse profile for the input to the regenerative amplifier. Alignment of the fiber should take account of the narrow range of coupler-fiber distances which allow high transmission, and the orientation of the fiber which results in passage of the correct polarization to the fiber output.

3.2.5 Regenerative Amplifier and Pulse Cleaner

The output of the fiber is seeded into the first amplification stage in the laser chain, the regenerative amplifier. This stage consists of a secondary laser cavity, which the stretched oscillator pulse traverses 25 times as it is amplified in a Ti:sapphire crystal before it is switched out for further amplification. The cavity is defined by two high reflectivity end mirrors, one planar, the other spherical concave with 5 meter radius of curvature to balance the diffraction of the Gaussian laser profile, resulting in a stable laser spatial mode. The cavity length is 2.3 meters, leading to a 15.5 nanosecond round trip time. Three optical elements are present within the cavity: the laser crystal, a fast Pockels' cell with a specially tailored pulse, and a thin film polarizer. Pulses are switched into and out of the regenerative amplifier cavity by the Pockels' cell and thin film polarizer, according to the sequence below.

The Ti:sapphire crystal is 5mm high, 10mm wide, and 10mm long and is mounted at Brewster's angle with respect to the laser cavity axis. The crystal is pumped by 45mJ of 532 nanometer wavelength light from a flashlamp-pumped Q-switched Nd:YAG laser [BigSky CFR-400] focused to 2mm diameter on the crystal face. The crystal has an absorption coefficient of 2.6cm^{-1}, so nearly all of the pump light is absorbed. It is mounted in a copper heat sink to avoid thermal lensing arising from the significant average power delivered to the crystal.

The term 'ultrashort laser pulse' is generally held to mean a pulse which has a very high contrast with the light which comes before or after it. Regenerative amplifiers can act as laser cavities even when not seeded, and amplified spontaneous emission (ASE) can produce significant intensity before or after main pulse known as pedestal, or 'foot' when it proceeds the main pulse. The thin film polarizer suppresses ASE buildup in the regen cavity for s-polarized light prior to seeding with the stretched oscillator beam. Seed pulses are injected with s-polarization by reflection off the crystal, and are 'stored' by halfwave rotation in the Pockels' cell [Medox Twin Peaks]. Given that the cavity round trip time is only 15.5 nanoseconds, the rise and fall times of the Pockels' cell must be less than half this value. The Pockels' cell is located at the cavity center so that the temporal separation of pulses passing through it from either direction is maximized. The Pockels' cell is triggered just before the seed pulse arrives, and rotates it to p-polarization so that it transmits through the thin film polarizer and is stored. The pulse then makes 24-25 passes through the Ti:sapphire crystal, and is amplified from ~0.5 nanoJoules to several milliJoules. The Pockels' cell is then triggered again, restoring the seed pulse to s-polarization, so that it reflects off the thin film polarizer and is extracted from the cavity with an amplification factor of nearly 10^7. The cavity switch-in and switch-out trigger times must be set carefully to maximize the amplified seed pulse energy while minimizing spectral distortion due to the beam traversing the Pockels' cell during the rise and fall of the high voltage pulse. The height of the two high voltage pulses to the Pockels' cell are not independent of one another, so optimization includes some compromise. Spectral bandwidth is lost in the regenerative amplifier due to gain narrowing, as seen in figure 3.3.

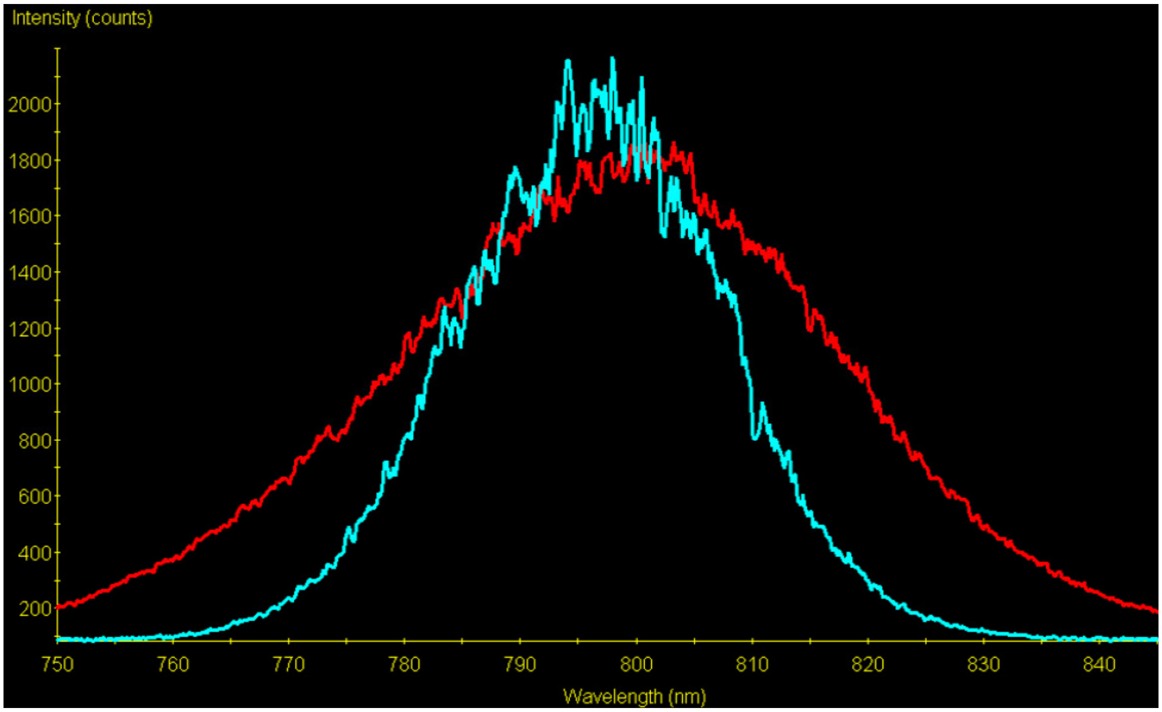

Figure 3.2: Spectrum of the laser pulse from the oscillator (red) and after the regenerative amplifier (blue). Gain narrowing during amplification reduces the spectral bandwidth.

Because ASE rejected from the cavity follows the same path, further pulse cleaning is necessary to achieve high temporal intensity contrast. Some small percentage of the seed pulse also leaks out along the beam path each pass, producing pre- and post-pulses at the 15.5ns cavity round trip time. An additional thin film polarizer after the regenerative amplifier rejects residual p-polarized light. Pre-pulses and post-pulses are removed by another polarizer-Pockels' cell-polarizer combination [Lasermetrics 5046SC FastPulse Technologies Inc.]. The contrast ratio (main pulse to largest pre- or post- pulse, nanosecond scale) after the pulse cleaner is better than 10^6, and the infrared pulse energy is 1-2 milliJoules. A mechanical shutter which accepts TTL triggers is installed before then next amplification stage, allowing rates for experiments from 10 Hz to single-shot.

3.2.6 Four-pass and Five-pass Amplifiers

The regenerative amplifier output is magnified in a Galilean telescope to reduce laser fluence and relayed to a round, 10mm diameter, 20mm long Ti:sapphire crystal in the next amplification stage. This stage is comprised of 4 passes through the crystal, in a 'bow-tie' or multipass amplifier configuration. The crystal is pumped by the remainder of the Big Sky YAG laser which pumps the regenerative amplifier, about 0.11 Joules. The crystal is mounted at brewster's angle to reduce ASE. The crystal is doped to a lower level (absorption coefficient 1.05cm^{-1}) to allow uniform absorption. After the fourth pass, the laser pulse is fed into a spatial filter with a large aperture, to remove any high spatial frequency distortion of the laser wavefront. Because the laser energy at that stage is ~20 milliJoules, the focus of this spatial filter is held at vacuum to prevent ionization-induced degradation of the laser pulse. After passage through the spatial filter the laser beam is recollimated to a larger (~1cm) beam size for futher amplification.

The output of the spatial filter then supplies the main amplification stage of the THOR laser, a 20mm diameter by 20mm long Ti:Sapphire crystal (absorption 2.30cm^{-1}). This stage is comprised of 5 passes through the crystal, again in a ‘bow-tie’ geometry. The crystal is pumped on either face by 1.2-1.3 Joules of 532 nanometer light from two Spectra-Physics PRO-350 Q-switched Nd:YAG lasers. Pumping on both faces allows the higher absorption coefficient while maintaining gain uniformity. Due to the significant power deposition (over 25 Watts) on the crystal, it is mounted in a copper jacket supplied with cooling water to prevent runaway thermal lens distortion of the amplified pulse. Because power is deposited on the center of the crystal and cooling supplied at the edges, a weak thermal lens develops (~100 meter focal length) which helps to maintain beam collimation during the 5 passes, allowing overfilling of the gain region for maximum energy extraction. The circumference of the crystal is painted black with a Sharpie marker to prevent parasitic transverse lasing. The crystal is mounted in a goniometer so that its crystalline axis may be aligned with the polarization of the laser; this prevents the formation of pre- or post- pulses through the crystal’s birefringence. In the five pass amplifier the infrared pulse energy increases by a factor of 50, to about one Joule. Compressing this pulse to under 40 femtoseconds with a 1 cm beam size would likely damage the compressor grating, so it is expanded in a second vacuum spatial filter to 5 cm in a superGaussian pulse shape (figure 3.3).

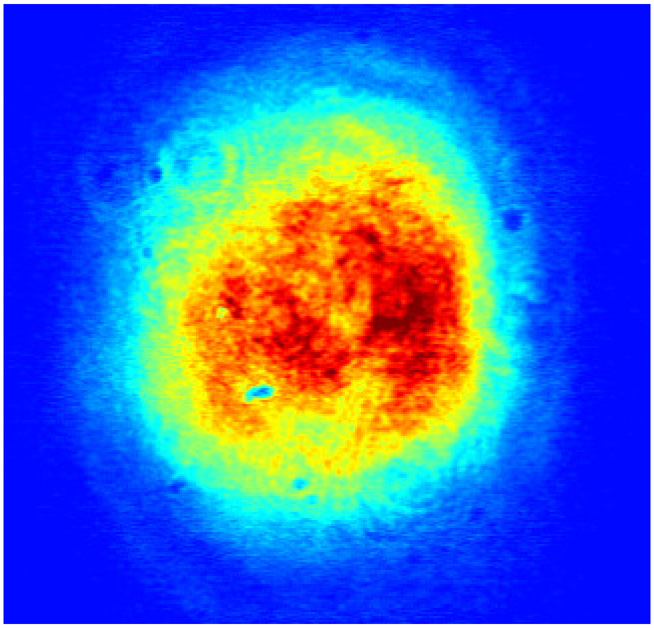

Figure 3.3: THOR amplified profile. Intensity increases from blue to red. The small dark spots are damage on the camera filters, and are not present on the laser beam itself.

3.2.8 Dust Suppression and Humidity Control

Due to the high intensities present on surfaces at particular parts of the laser system, airborne dust can be ‘burnt’ onto the face of high fluence optics. Feeding dry nitrogen into the laser enclosures, particularly of the large PRO lasers and the oscillator cavity, help prevent damage by dust contamination. The multipass amplifier enclosure is supplied with a positive pressure of air which has been passed through a hydrophilic filter (Dry-Rite) to remove humidity. Because the five-pass crystal is maintained below room temperature by its chilling water, high humidity can lead to condensation on the crystal face which can microlens the pump laser beams and burn tracks into the crystal permanently.

3.2.9 Vacuum Compressor

Compression of the fully amplified THOR laser pulse takes place in a large vacuum chamber maintained at a pressure near 20 microTorr. The 8-pass optical geometry of the compressor is shown in Figure 3.1, and basically represents the inverse of the stretcher in dispersion, with a slight adjustment to correct for the dispersion which the pulse accumulates in the amplifier chain. The gold grating has 1480 lines/mm, 40cm diameter, and was manufactured by Jobin Yvon. The GVD is controlled by translating the rooftop mirror tangent to the laser beam, and can be controlled externally in order to minimize the pulse duration at an experiment endstation; this allows correction of phase introduced by transmissive optics after the compressor. The 3rd order dispersion is corrected by fine-tuning the grating angle; this angle is set by minimizing the pulse duration versus grating angle, and is not typically adjusted for particular experiments. The overall transmission of the compressor upon installation was above 60%; it is now approximately 50%, due to accumulated laser-assisted contamination.[6] The fluence on the grating on the last pass is about 22 milliJoule per cm^2, well below the damage threshold of the gold surface for 37 femtosecond pulses. THOR can be operated with the vacuum compressor at atmospheric pressure, if the pulse energy at the compressor input is maintained below ~200 milliJoules. In this operating condition, the compressor rooftop needs to be adjusted to minimize the pulse duration using the vacuum autocorrelator. This corrects for the dispersion introduced in air; without compensation the pulse width exceeds 100fs.

---

[6] When the laser hits the grating on its final pass, it is at sufficiently high intensity to assist in photocatalyzed adsorption of vacuum chamber contaminants (hydrocarbons) onto the grating surface. This has resulted in the accumulation of a blemish on the grating where the last pass lands. This blemish has been treated over the years by UV-assisted ozone cleaning, which improves the compressor transmission to some degree.

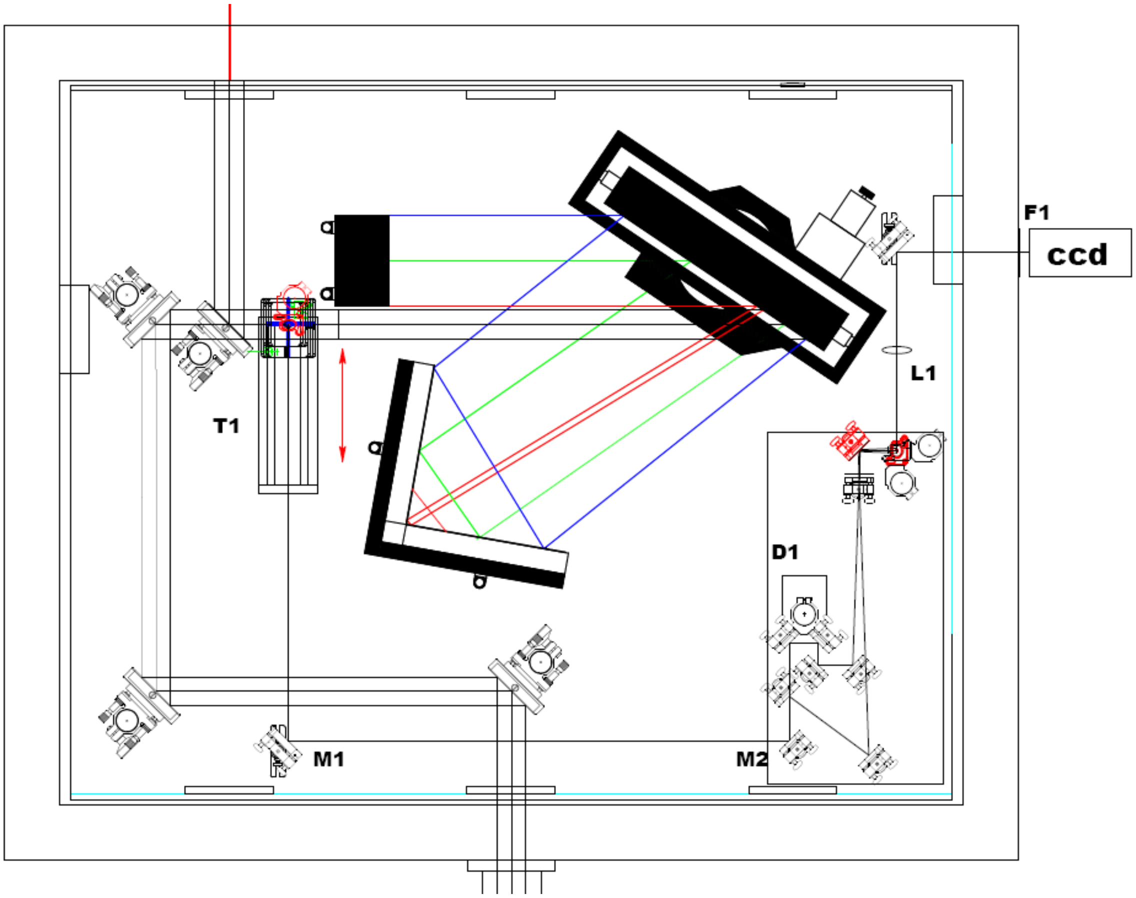

Figure 3.3: Vacuum compressor, autocorrelator pickoff mirror on translation stage, Vacuum 2nd order autocorrelator. See text for details of operation

Compressor vacuum is maintained by a large oil-lubricated turbomolecular pump [Sergeant-Welch] backed by a rotary pump/ Roots' blower combination [Edwards QDP40/QMB250]. The rotary pump is used to rough the chamber down to the ~10 Torr level, at which point the Roots blower can be turned on. The Roots blower rapidly brings the pressure down to sub-Torr levels. If the pressure does not reach ~100 milliTorr within an hour of the start of pumpdown, a leak is likely present. Once the pressure is below this level, the turbomolecular pump can be engaged at low speed. Typical compressor base pressure is 20 microTorr.

3.2.10 Mask for Annular Profile and Autocorrelator Pickoff

To produce the annular profile for HHG, an elliptical mirror with 0.5” minor and 0.707” major axes is suspended on wires in an open frame large enough to transmit most of the beam. The mirror is held at 45° with respect to the laser axis, and reflects the central portion of the beam down to transport mirrors, which supply light to a 2^{nd} order autocorrelator also installed in the compressor vacuum chamber. Although the center of the laser spot is more intense than the wings, the superGaussian profile leads to a fairly uniform intensity between the 0.25” inner radius and an outer radius of about 0.75”. Some clipping of the laser spot on the frame that holds the elliptical mirror occurs at a radius near 1” from the laser axis. The mirror is mounted on a translation stage built by myself and Alexei Belolipetski in the Physics Student Machine Shop in 2005. The stage employs a single vacuum-compatible piezoelectric motor [Thorlabs, Inc. Picomotor], gears to obtain a mechanical advantage, and rack-and-pinion gearing to allow translation over arbitrary distances.

3.2.11 Vacuum Autocorrelator

A single shot second order autocorrelator [63] in the vacuum compressor chamber allows pulse duration measurement under vacuum. The autocorrelation is imaged to a CCD camera outside the vacuum system for simple data acquisition. The autocorrelator was installed in 2006 by Alexei Belolipetski, Irina Churina, Woo Suk Bang, and myself. When the autocorrelator pickoff mirror is in place, it diverts an 0.5” diameter portion of the compressed THOR pulse down to a periscope mirror, from which it is steered by mirrors M1 and M2 in to the autocorrelator (Fig. 3.3). The autocorrelator begins at a thin beamsplitter which produces two nearly identical copies of the laser pulse. The reflected copy is directed to a beta-barium borate (BBO) cryatal, at a slight horizontal angle with respect to the optimum phase matching angle of for second harmonic generation in the BBO crystal. The transmitted copy is directed to delay line D1, then brought to the BBO crystal, again with a horizontal tilt with respect to the optimum phase matching angle, opposite the tilt of the reflected copy. In this configuration, each beam will create some collinear second-harmonic light on its own, and the crystal can be tilted to balance the intensity of the second harmonic beams. The delay line is then adjusted so that the path lengths of the two copies are identical to within a few microns; making phase matching conditions ideal for harmonics produced by the sum of the two copies (the 2nd order autocorrelation function.) The spatial width of the sum signal is a function of the duration of the two copies, convolved with their crossing angle (Fig. 3.4).

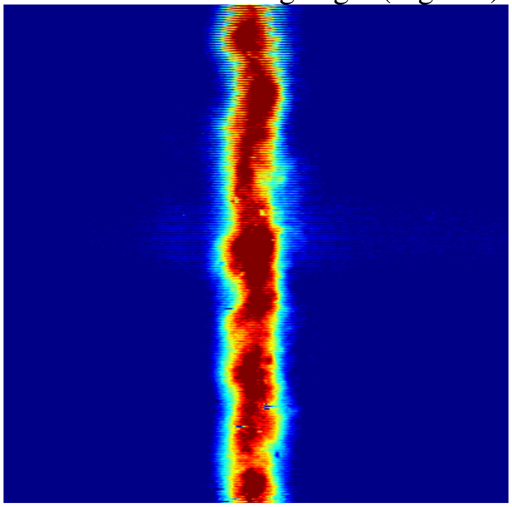

Figure 3.4: Autocorrelation of compressed pulse. Distortions come from dust contamination on the BBO crystal, without which the stripe would be vertically uniform.

This sum signal (a vertical stripe) is relay imaged to the CCD camera outside the vacuum chamber by lens L1. Calibration of the CCD camera in pixels/femtosecond is accomplished by translating delay line D1 over known distances and recording the centroid displacement of the autocorrelation signal on the CCD (Fig 3.5).

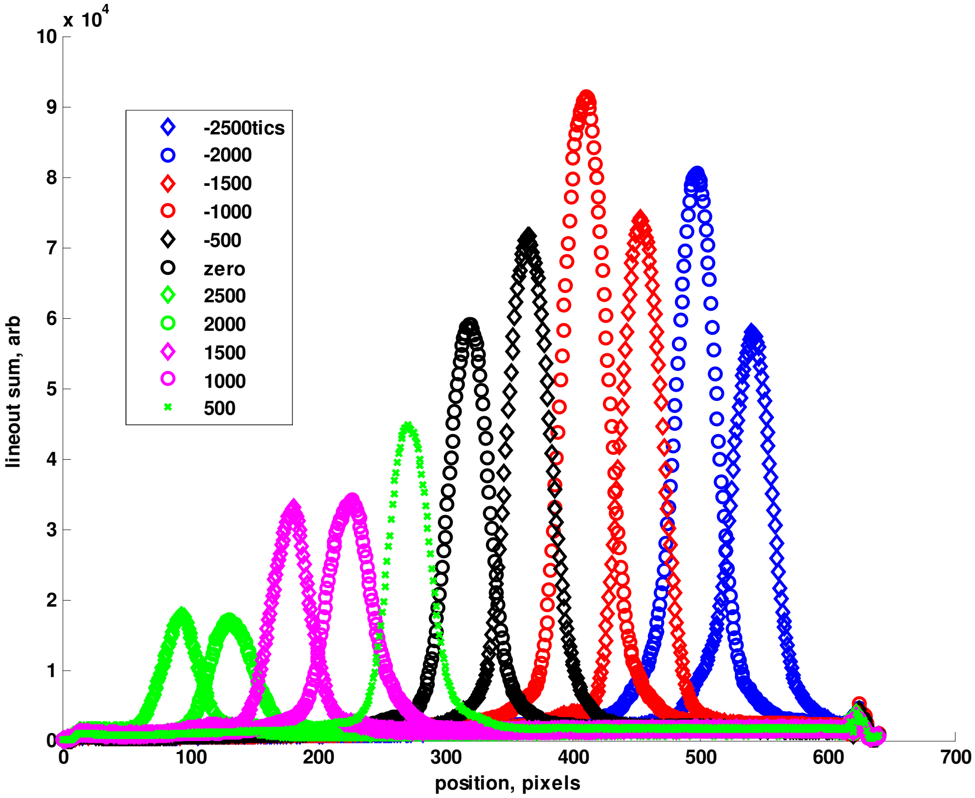

Figure 3.5: Vacuum autocorrelator CCD calibration. Centroid shift versus delay gives CCD calibration in pixels/femtosecond.

Once calibrated, the delay line is set so that the signal is centered on the CCD. The thin beamsplitter introduces a small amount of dispersion to the transmitted copy, too little to significantly distort pulses above 30fs duration. Alignment, calibration, and operation of the autocorrelator can be accomplished with 10 to 30 milliJoule infrared pulse energy at the compressor input.

3.2.12 Vacuum Variable Iris

In order to make the outer diameter of the annular infrared profile adjustable, a vacuum compatible motorized variable-aperture iris was built, again based on simple gearing and piezoelectric motors. A 100mm aperture iris [Rolyn Optics] is mounted in an aluminum block (Fig. 3.4) holding a geared picomotor. A length of stainless-steel gear rack which has been softened with an oxy-acetylene torch and hammered to the curve of the iris' outer diameter[7] is attached to the iris adjustment point with a small screw, and meshes with the gears of the picomotor. This allows full control of the outer diameter of the infrared beam from outside the vacuum chamber, an important parameter for optimizing HHG with an annular beam.

---

[7] This work was performed in the Physics Student Machine Shop, with valuable assistance from Jack Clifford.

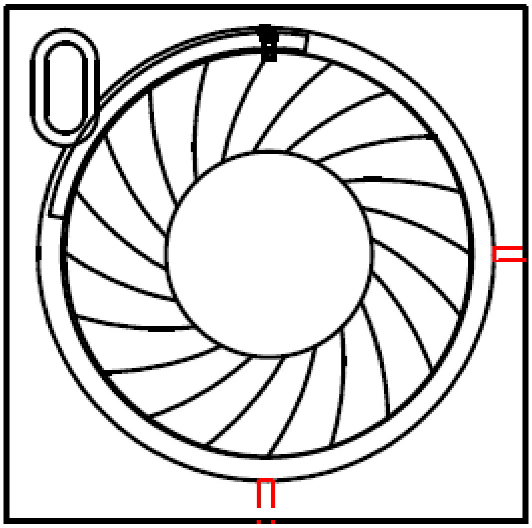

Figure 3.4: Variable vacuum iris.

Chapter 4: High Harmonics Beamline on THOR

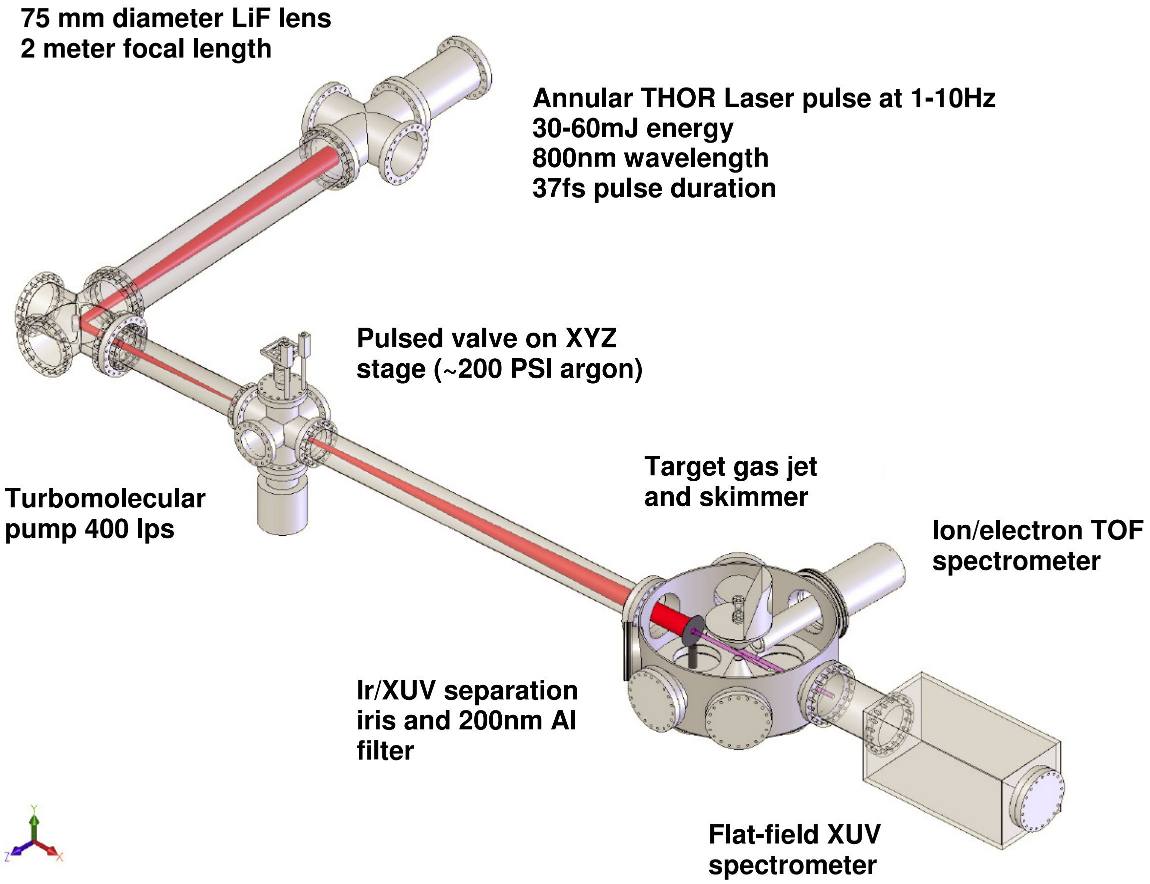

Figure 4.1: THOR HHG beamline, target chamber and diagnostics

4.1.1 Beam Transport and Imaging

The THOR laser hosts multiple experiment stations, so the beamline design needed to be compatible with other experiments. Due to the favorable scaling of high harmonic yield with the focal length of the infrared focusing optic, the HHG beamline was designed to use the maximum available lab space (Fig. 4.1). The annular mask described in chapter 3 is relay imaged by a 2 meter focal length, 75 millimeter diameter LiF lens to an iris 4 meters after the lens, with -1 magnification. The lens material was chosen to avoid self-focusing and white light generation due to accumulated B-integral as the compressed infrared pulse passes through the lens. A motorized 45° mirror located 1 meter after the lens acts as the final steering optic before the infrared focus.

After the beam diverges from the focus, the infrared is blocked in the image plane by an iris; the central portion of the annular profile, containing the XUV harmonics and scattered infrared light, is incident on a thin Al film mounted on a vacuum manipulator, which makes a light-tight seal with the iris when in the filter is in position. A HeNe laser coaxial with the infrared annulus allows alignment of the XUV optics when the filter is removed.

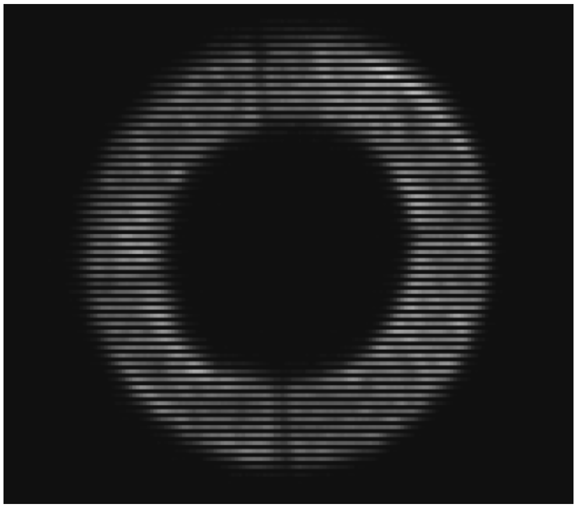

Figure 4.2: Annular infrared profile in image plane, with suspension wires visible. Inner diameter is 12.5 mm, outer diameter ~25 mm. Image is taken slightly off-normal.

The outer diameter of the annular infrared laser profile can be varied using the motorized iris described in chapter 3. The harmonic yield was optimized as a function of the outer diameter in the experiments described in this chapter in 4.2, and in every case resulted in substantial reduction of the outer diameter to maximize harmonic yield. An example beam profile in the image plane of the mask (Fig. 4.2) reveals the uniformity of the superGaussian THOR profile when clipped to an outer diameter of ~25mm. The transmission of the iris-mask system was measured to be about 25% when optimal.

4.1.2 Vacuum pumps

The HHG vacuum chamber is separated from the vacuum compressor by the LiF lens on the ‘upstream’ side, and from the target chamber by a gate valve on the ‘downstream’ side before the target chamber. The HHG chamber is evacuated by a water-cooled turbomolecular pump [Alcatel 5402-CP] backed by a mechanical pump [Edwards E2M18] equipped with a molecular sieve oil trap. The turbomolecular pump is mounted on a 6-way 6” CF-sealed vacuum cross, directly opposite the HHG pulsed valve. When isolated from the target chamber, and when no gas is introduced, the base pressure of the chamber is ~0.5 microTorr as observed on an ion gauge mounted on the 6-way cross. Firing the HHG valve under normal operating conditions causes the chamber pressure to spike to the milliTorr level. The turbomolecular pump was chosen because its relatively high maximum sustainable inlet pressure (~100 milliTorr) enables it to effectively dispose of the HHG gas between laser pulses. A 5mm diameter aperture was added at the ‘downstream’ side of the 6-way cross to restrict gas conductance from the HHG jet to the target chamber without clipping the laser beam. A secondary turbomolecular pump [SEIKO-SEIKI STP301-H] located after the infrared-XUV separation iris provides additional differential pumping between the HHG jet and the target chamber, reducing argon leakage into the target chamber. When the gate valve to the target chamber is open, under normal operating conditions the HHG jet introduces ~5 microTorr partial pressure of argon gas into the target chamber.

4.1.3 Timing

Variable triggers for the gas jets and mechanical shutter are provided from the THOR timing system via the target room delay generator [Stanford Research Systems DDG535]. The large time delays (~0.1 s) required for these slow, mechanical devices lead to ~100ns trigger jitter. A fast photodiode located at the final steering optic provides sub-nanosecond trigger jitter for time-of-flight detection, and is used to monitor the delay between pulsed valve firing times and the arrival of the infrared pulse.

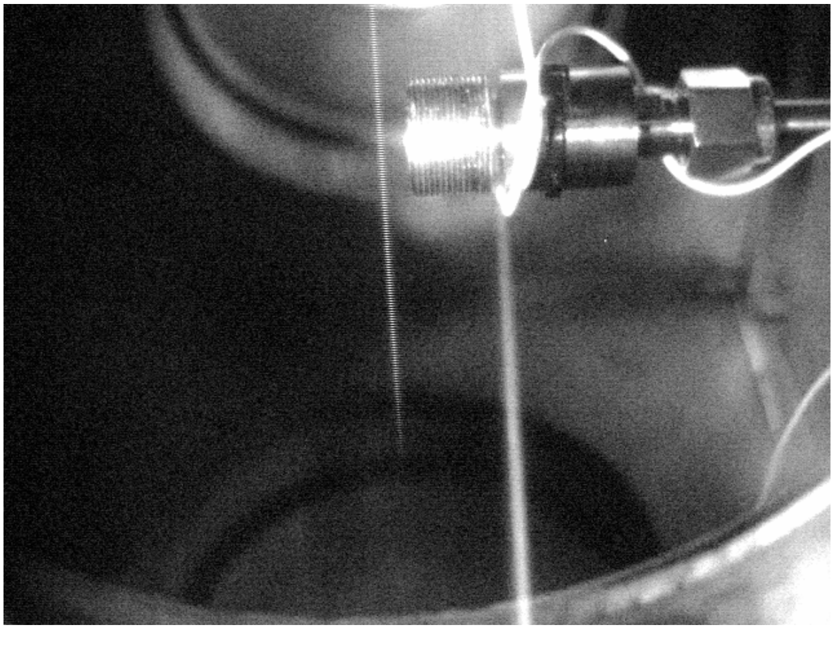

Figure 4.3: HHG nozzle at infrared focus with N_2 static fill. Valve body and wiring visible in upper right; laser induced breakdown along laser axis visible (thin central stripe.)

4.1.4 HHG jet

Argon is delivered to the HHG interaction region by a solenoid-driven pulsed valve [Parker-Hannifin General Valve Series 9] fired before the laser pulse arrives. Valves used in the HHG optimization experiments had throat diameters of 500 and 750 microns, and were supplied with argon at stagnation pressures of 100-200 PSI. The optimal opening trigger time for HHG was found to be ~0.5 milliseconds before the laser pulse, with a 500-800 millisecond open duration. The 750 micron valve had a short conical nozzle after the poppet, while the 500 micron valve was essentially a 'flat-plate' nozzle. Figure 4.3 shows the 500 micron valve (top right) near the infrared focus (vertical stripe, center top) when the chamber was backfilled with ~10 milliTorr N_2 to induce visible breakdown. The infrared intensity is near-constant over the vertical stripe (~50mm) while the gas column interacts with the infrared over a far shorter distance (~1mm.) The HHG jet is mounted near the infrared focus on a 3-axis vacuum translation stage allowing optimization of jet-focus position.[8] Translations over ±0.5" along the laser axis require breaking vacuum and changing tube lengths.

In the range of argon pressures used for HHG, clustering of the argon gas will be minimal [82] The argon density in the region beneath the nozzle will follow a $\cos^2$ angular distribution with both nozzle types, and falls off roughly as $(y/d)^2$ with distance from the nozzle. The base pressure in the HHG region is proportional to the product of the valve repetition rate, valve open time, and argon stagnation pressure; limiting the repetition rate allows use of high pressures and longer open times. Partial pressure of argon in the target chamber interaction region is proportional to the HHG region pressure,

---

[8] This stage was designed by the author in 2004, and built by the Physics Machine Shop with off-the-shelf parts costing under $800.

so HHG jet operating parameters are limited by the vacuum requirements of the target chamber.

4.1.5 XUV Filtering

Given the low conversion efficiency (~10^{-6}) of HHG, careful disposal of the infrared light used to make XUV pulses is essential. A mask was made using an iris and a shroud of anodized aluminum foil, which blocks all direct infrared light. Light which is refracted in the HHG plasma or which makes multiple bounces through the HHG beamline is prevented from entering the target chamber by positioning a 200 nanometer thick, 1 cm diameter free-standing Al filter [Luxel Corp.] in the annular region of the infrared profile. The transmission spectrum of this filter, with 7.5 nanometer Al_2O_3 oxidation layers on both sides, was calculated using the CXRO database[9] and is shown in Figure 4.4. Due to the large aperture and lack of mesh support, the filter is extremely fragile and must be handled with caution on installation. All venting of the HHG chamber is done in a controlled manner using dry nitrogen, to prevent dust ("shrapnel") or strong air currents from destroying the filter.

---

[9] http://henke.lbl.gov/optical_constants

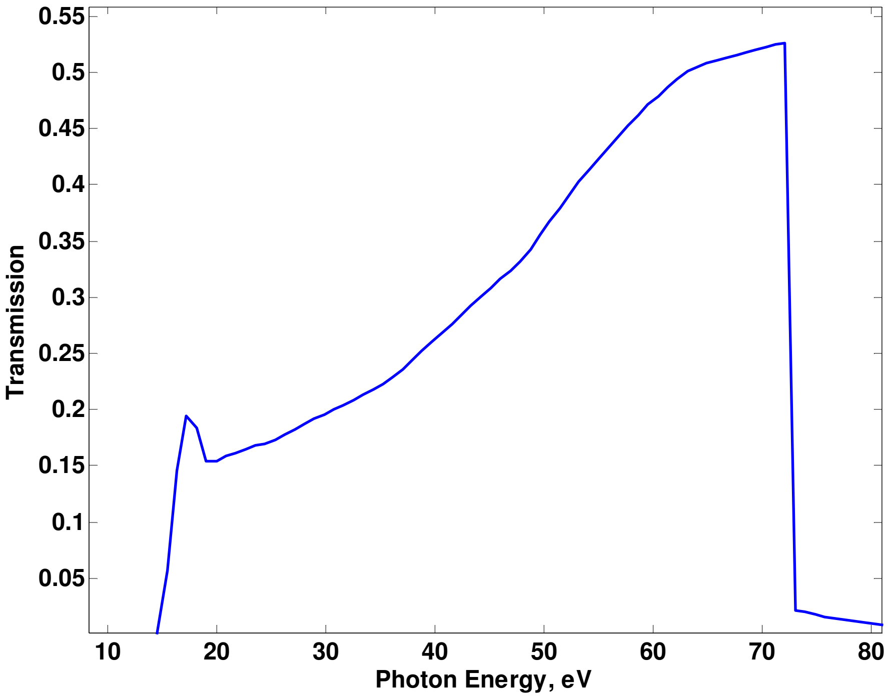

Figure 4.4: Aluminum thin film filter transmission including 15nm oxide layer. Data from CXRO database.

Filter transmission measurements were performed using an XUV photodiode [IRD Inc. AXUV-10] and two filters, one of which could be removed, and indicate a filter transmission of 20% for the 21st harmonic at 32.6 eV photon energy, consistent with 15nm average oxide thickness. Infrared transmission is essentially zero, and would result only from pinholes in the filter. The absorption of Al at 800nm is nearly 20% at normal incidence, meaning that power deposition into the thin film is a serious consideration. When significant laser energy is incident on the filter due to misalignment, the filter absorbs enough energy to create temporary distortions or ripples on the mirror-like filter surface. If these ripples become too violent they can result in tearing of the filter.

Following the Al filter, the XUV beam passes into the target chamber. A fused silica microscope slide on a linear translator can be inserted in the XUV beam path to determine if any observed signals result from infrared light (the slide will block all harmonic light, while having very little effect on infrared.) This slide was used along with an XUV photodiode in the target chamber to determine the overall divergence of the 21st harmonic (~2.5 milliradian full angle or ~5mm spot diameter at the target chamber.) For the data presented in this work, inserting the microscope slide identically reduced XUV photodiode, electron, and ion signals to zero.

4.1.6 Target Chamber

After the XUV light is separated from the infrared, it passes through a gate valve into the XUV target chamber. The target chamber originally planned for the XUV-cluster experiments was not available in time for the experiments reported here. Instead, a 6-way 8” CF-sealed chamber held all diagnostics other than the XUV spectrometer (which has its own chamber.) Multiple layers of anodized aluminum foil baffling block scattered light from the target chamber. The Sc/Si multilayer mirrors used to select and focus individual harmonics, the target cluster beam source, and the time of flight spectrometer all mount inside the target chamber. Details of the target chamber components are presented in later sections.

4.1.7 XUV Multilayer mirrors

One of the major challenges to experiments employing XUV light is the lack of flexibility in choosing materials for focusing optics. Although many traditional coatings (Al, Ag, Au, Pt) have high grazing incidence reflectivity, the normal incidence reflectivity is reduced dramatically [65]. Unprotected[10] Al mirrors have normal incidence reflectivity as high as 90% for VUV radiation down to 100 nanometer wavelength, but their reflectivity is dramatically reduced by the formation of an oxide layer if the mirror is ever exposed to air. Unprotected Ag or Au mirrors have normal incidence reflectivity of 5-10% in the wavelength range of our harmonics; Pt has a reflectivity peak above 20% around 60 nanometers. More exotic materials (Ir, Os, W) have peaks as high as 35%, also near 60 nanometers. Such mirrors can be custom-fabricated, but their broad reflectivity bands would necessitate use of a diffraction grating if experiments require well-defined photon energy. Multilayer mirrors can solve both problems simultaneously, providing a high reflectivity in a bandwidth narrow enough to isolate individual harmonics.

Multilayer coatings for XUV optics function on the same ‘quarter-wave stack’ principle used with common multilayer-dielectric laser mirrors. In this scheme, 2 or more materials are deposited on an optical substrate in alternating layers of well-defined thickness of several nanometers. The first layer (for XUV optics, most often Si) is essentially transparent to the incident light. The second layer material is chosen to have a high dielectric function at the frequency of the incident light. The contrast between the two layers causes some reflection to occur at the interface. Light which passes through the second layer sees another transparent layer, and another high-dielectric layer, and so on. By choosing the layer thicknesses carefully, the phase advance of the light reflected from adjacent layer boundaries causes the reflections to add constructively. Thus although the reflectivity of any single layer is low, constructive interference leads to net reflectivity as high as 70% for 14 nanometer light and Mo/Si mirrors. The interference effect also acts as a narrow bandpass filter, allowing isolation and focusing of individual harmonics using a single optic.

---

[10] ‘Unprotected’ refers to the lack of a durable overcoat of MgF or similar material, applied by default to almost all commercial laser optics.

In the 35-50 nanometer wavelength range, Mo/Si mirrors have low reflectivity, and Sc offers a better choice for the high contrast layer. Mirrors based on Sc/Si multilayers have normal incidence reflectivity of 30-45% for light of 35-50 nanometer wavelength [67, 68]. The Sc/Si mirror used in this work was coated for 38.1nm light by Igor Artyukov at the Lebedev Physical Institute in Moscow, Russia. The mirror radius of curvature is 250mm. The coating consists of ~10 periods of Sc/Si with thickness ratio L_{Sc}/L_{Si}~0.25 and bilayer thickness ~19.5 nanometers. The reflectivity of this mirror optimized for the 21st harmonic at 38 nanometers (blue) and the 23rd at 35 nanometers (black dash) was modeled using the CXRO database and is plotted in Fig. 4.9. The measured reflectivity was 0.35±0.05.

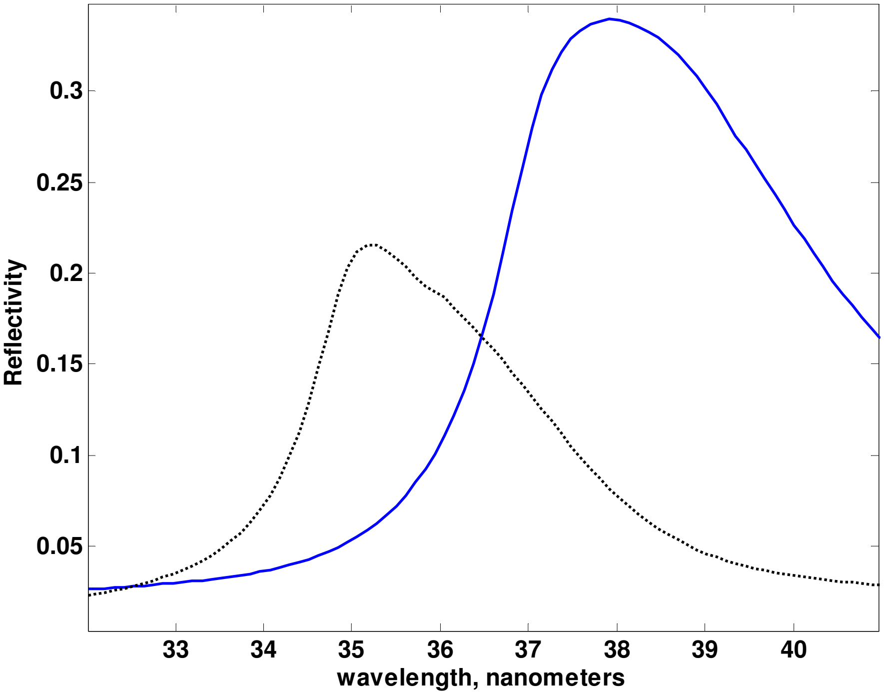

Figure 4.9: Calculated reflectivity of Sc/Si mirrors, using CXRO database.

4.2 Harmonics beamline performance

Commissioning of the harmonics beamline followed three major themes: verification of harmonic generation, optimization of the XUV pulse energy yield, and characterization of the focus. Verification consisted of imaging the harmonics on a grazing incidence flat field XUV spectrometer coupled to an imaging microchannel plate (MCP). Phase matching conditions were optimized by varying the HHG medium position with respect to the infrared focus while monitoring the 21st harmonic energy in the XUV focus. The harmonic signal dropped off rapidly when the gas jet distance to the laser axis was increased. The scaling of the pulse energy with HHG medium density showed yield saturation and gradual decline at high argon density. The combination of the above two factors led to the design of a nozzle body intended to increase HHG medium uniformity and lengthen the interaction region. The spot size of the focal point of the 21st harmonic was measured by scanning a razor blade across the focus transversely and measuring the obscuration on the XUV photodiode. With a reasonable guess at the pulse duration, the peak XUV intensity in the focal volume is estimated to be above 10^{11} Wcm^{-2}.

4.2.1 XUV Harmonic Spectrum

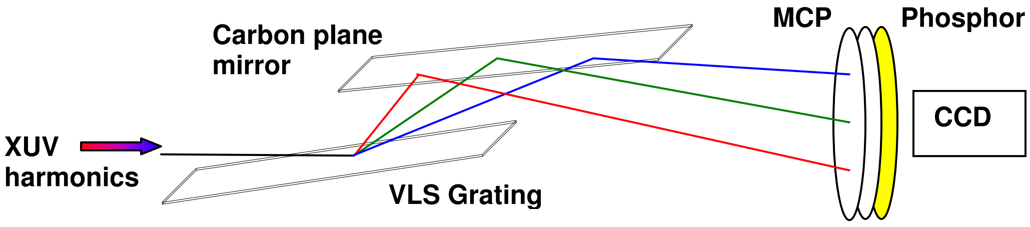

Figure 4.5: Cartoon of grazing incidence XUV spectrometer

Harmonic spectra were recorded using a grazing incidence XUV spectrometer based on a concave, gold coated variable line spacing (VLS) grating [Hitachi Corp.] shown schematically in Fig. 4.5. The image forming properties of this grating were described by Harada and Kita [70] and feature a region of 'flat' focal plane. The flat field enables spectra to be recorded on a planar imaging detector, in this case a multichannel plate coupled to a phosphor screen [Burle Instruments]. The grating's focal "plane", modeled in Appendix A, actually has significant 2nd order curvature, see Fig. 4.6.

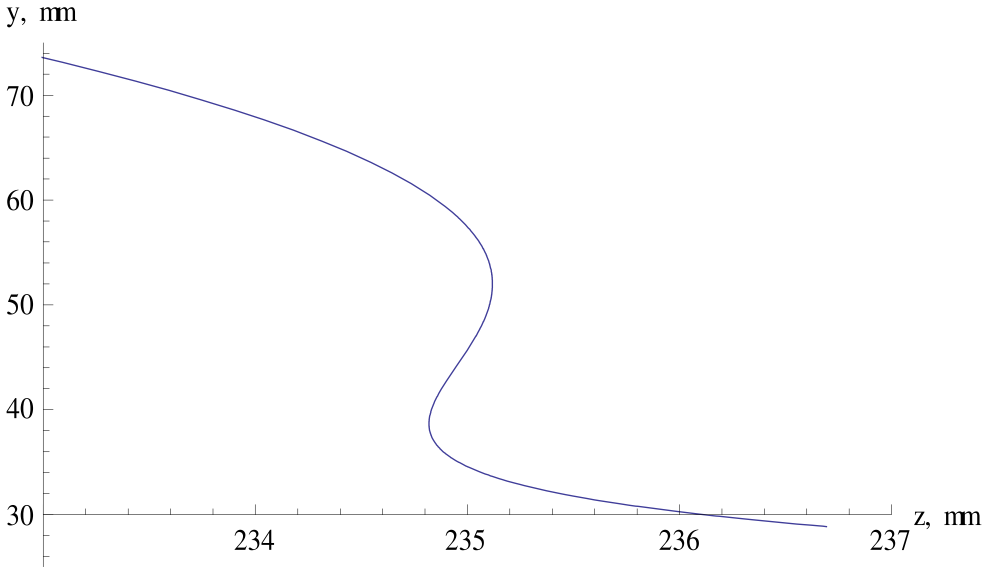

Figure 4.6: Focal curve of Hitachi VLS grating for wavelengths from 50nm (upper left) to 5nm (lower right) based on calculations in Appendix A. The MCP is located at 235mm, where the focal curve of the grating is nearly vertical.

In this implementation, a grazing incidence planar carbon mirror steers the diffracted beam back onto the laser axis. The grating is blazed for 3° grazing incidence. Both the grating and the carbon mirror can be translated The spectrometer can be aligned using a HeNe laser by allowing a small portion of the HeNe beam to pass over the top of the grating, and monitoring the distance between the zero order (specular) diffraction and the undeflected beam. Anodized aluminum foil baffling at appropriate angles prevents specular and scattered light from reaching the MCP. The phosphor screen inside the vacuum chamber is coupled by an imaging fiber bundle plate to the outside of the chamber, then imaged with a CCD camera connected to a frame grabber for triggered image acquisition.

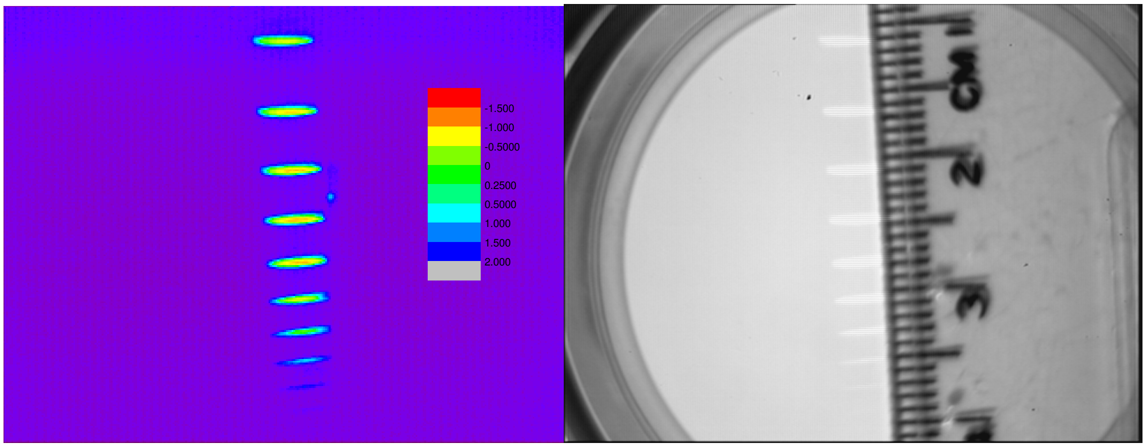

Figure 4.7: Harmonic spectrum in argon (left) and spatial calibration (right). Wavelength increases from bottom to top. The small spot to the right of the harmonic spots near the image center is due to a crack on the MCP, and can be subtracted out as background.

The spectrometer was calibrated using the harmonics themselves, given the lack of line radiation sources of 30-40 nanometer radiation. First, a spectrum is acquired as shown in Fig. 4.7. Second, spatial scale is established by imaging a ruler at the fiber bundle plate surface (Fig. 4.7 right). Finally, the distance between harmonics is compared with the predicted spacing along the focal curve of the grating calculated using the equations for Harada VLS gratings (see Appendix A.) This results in a ‘comb’ of unequally spaced harmonic peaks, which only matches up at one position, allowing identification of harmonic orders. Spectra were acquired at low infrared energy without an Al filter, so that the observed spectrum results from the convolution of the generated harmonic spectrum with the spectrometer efficiency.[11] Additionally, the annular beam mask was removed so that the spatial distribution of the harmonics could be observed. The lowest order harmonic (top of Fig. 4.7) is the 15th, while the highest order observed (bottom of figure) is the 33rd. Although lower harmonic orders were observed, the geometrical limits of the spectrometer prevented simultaneous recording of low- high-order harmonics.

The spatial distribution of the harmonics follows the predictions of chapter 2. The high-order cutoff implies a ponderomotive energy around 10eV (Keldysh $\gamma = 0.9$), and the intensity in the plateau region is indeed roughly constant. The angular distribution of the harmonics also narrows at high orders as predicted, and remains roughly constant in the plateau. A lineout of the XUV spectrum with harmonic orders labeled is presented in Fig. 4.8.

---

[11] The efficiency of first-order diffraction from the VLS grating drops off for wavelengths above 30nm, as does the reflectance of the carbon mirror, as light at long wavelengths is incident at large grazing angles.

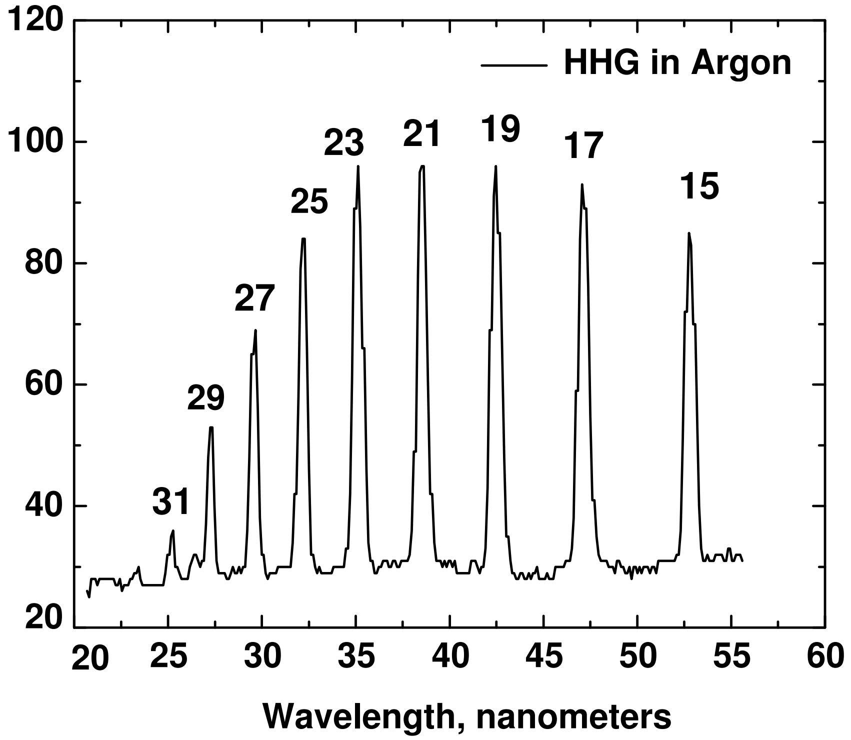

Figure 4.8: Lineout of XUV spectrum generated in Ar. Vertical axis is intensity in arbitrary units.

4.2.2 HHG yield optimization

In an attempt to increase harmonic pulse energy by improving phase matching conditions, we investigated the dependence of harmonic yield on the density of the HHG medium and its position with respect to the infrared focus. HHG yield showed strong dependence on the longitudinal jet-focus position, with a factor of five improvement when the jet is moved from the infrared focus to a position approximately one confocal length away from the focus. The improvement was more dramatic on the ‘upstream’ side, where the harmonic medium interacts with the infrared pulse before the infrared reaches focus. The density and interaction length were varied by changing the stagnation pressure in the pulsed valve, and the distance from the nozzle to the laser axis. Stagnation pressure scans in ‘optimized’ and ‘non-optimized’ longitudinal configurations showed saturation and gradual rolloff of HHG yield, with no peak or resonance. In all cases, the harmonic yield dropped off very rapidly as the HHG nozzle was moved away from the laser axis, suggesting that the effective coherence length is short and favors sharp transition between the medium and the background vacuum. The dropoff in HHG yield was so abrupt as to imply that only the part of the laser profile closest to the jet contributes to harmonic production. This led to the design of a nozzle adapter to increase the uniformity of the argon HHG medium and to increase the useful interaction length. The net result of optimization was an increase in the usable HHG signal by an order of magnitude.

To optimize HHG yield, an XUV photodiode [IRD Inc. AXUV-10] was positioned in the target chamber at the focus of the Sc/Si multilayer mirror. The filter and microscope slide described in section 4.1.5 could be moved in and out of the XUV beam to verify that no infrared contributed to the photodiode signal. The XUV pulse energy is proportional to the integrated photodiode current, and for a given photodiode the pulse energy is proportional to the photodiode peak voltage, because the XUV signal is very short with respect to the photodiode response times. XUV photodiode signals were averaged for 200 shots per point using a digital sampling oscilloscope [LeCroy Waverunner LT354].

4.2.3 Longitudinal phase matching

Harmonic yield as a function of HHG nozzle position along the axis of laser propagation is plotted in Fig. 4.5. Nozzle position is defined as positive when the laser interacts with the harmonic medium after the laser has reached a focus (“downstream” of the focus) At each nozzle position, the infrared energy is increased from the threshold for harmonic signal to the point where saturation effects become significant. XUV photodiode response is given for infrared energies 80 (dash magenta), 100 (dash blue), 150 (dash green), 200 (dash red), 250 (dash black), 300 (green), 350 (red), 400 (blue), and 500mJ (black) at vacuum compressor input.[12] Data marked by asterisks and diamonds indicate iris-optimized measurements at 300mJ and 350mJ. Data marked with diamonds were taken with the 500 micron nozzle; all other data was taken with the 750 micron conical nozzle. The Ar stagnation pressure is 200 PSI, with an open time of 450 microseconds. The ‘gaps’ in the data in Fig. 4.5 result from the limited lengths of 6” CF-sealed vacuum piping available; for each tubing configuration, the nozzle was scanned ±0.5”.

A fused silica lens was used to create the infrared focus for the data presented in this section; white light generation was observed originating from the silica lens for pulse energy over 300mJ, suggesting that accumulated B-integral and self-phase modulation in the lens would distort the infrared pulse and reduce harmonic yield. After the optimization experiments, the lens was replaced with a LiF lens to reduce nonlinear effects; no white light generation was observed below 400mJ infrared energy at the compressor input. However, at infrared energy over 350mJ, visible damage to the final steering optic coating was observed. Because of this damage, the infrared energy was ultimately limited to 350mJ at the compressor (~50mJ at the HHG focus.)

---

[12] After considering the transmission of the compressor and the mask/iris, this corresponds to 14 mJ pulse energy at the HHG nozzle. For convenience, all energies are reported as measured at the compressor entrance. Overall amplifier-to-IR focus transmission of 13% is typical at optimal variable iris diameter.

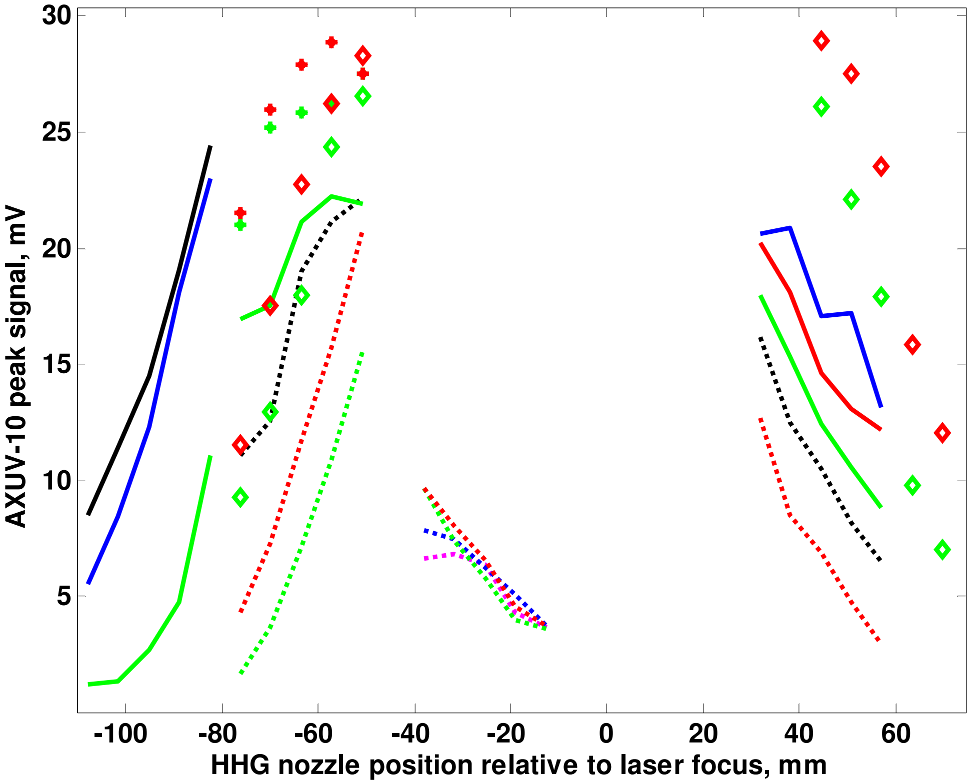

Figure 4.9: Harmonic yield versus nozzle position on laser axis.

When the nozzle is positioned close to the focus, saturation begins at very low yield for infrared energy around 100mJ at the input to the vacuum compressor. Changing the variable iris diameter at this position had little effect on the yield, and even for the lowest infrared pulse energy the yield increases with distance from focus. The spread in yield around z = -40mm suggests that moving well outside the focus is necessary to allow high infrared pulse energy with good XUV conversion efficiency.

Major improvements in conversion efficiency and total yield were found on either side of the infrared focus. On the ‘upstream’ side the peak occurs farther from the focus (z ~ -50mm) than on the 'downstream' side (z ~ 25mm). Overall, the yield versus nozzle position curve is shaped like an 'M'. Saturation of harmonic yield is evident in the peaks on both sides, as the harmonic signal increase is less than linear with infrared energy. Declining conversion efficiency leads to a limit on XUV pulse energy where increasing the infrared energy has little effect. Because of the damage to optics observed when the infrared energy exceeded 350mJ, effort was directed to finding jet-focus positions with high XUV pulse energy for infrared energy below this threshold. Optimizing the variable iris diameter resulted in substantial improvements in 21st harmonic energy for 300-350mJ infrared energy (asterisks and diamonds in Fig. 4.9, compare to red and green lines.) The yield from the 500 micron flat nozzle (diamonds) was comparable to the 750 micron conical nozzle yield (asterisks) in the 'peak' region, but significantly worse when the nozzle-focus distance was increased. This suggests that the larger nozzle is more appropriate for the large transverse infrared profile when the interaction point is far from the focus.

4.2.4 Pressure dependence of harmonic yield

The nonlinear dipole and plasma phase-matching contributions to HHG depend on atomic density. It may be possible to control these contributions and improve harmonic yield by tuning the stagnation pressure in the HHG valve. The pressure dependence of the 21st harmonic yield for 300mJ infrared energy is presented in Figure 4.10 for an 'optimized' longitudinal position (z=+50mm, blue dash) and a 'detuned' longitudinal position (z= -80mm, black) far from the focus. In both cases, the harmonic signal rises as the pressure is increased from zero, then rolls off at high pressure. We see no sharp peak in the harmonic response versus HHG gas pressure.

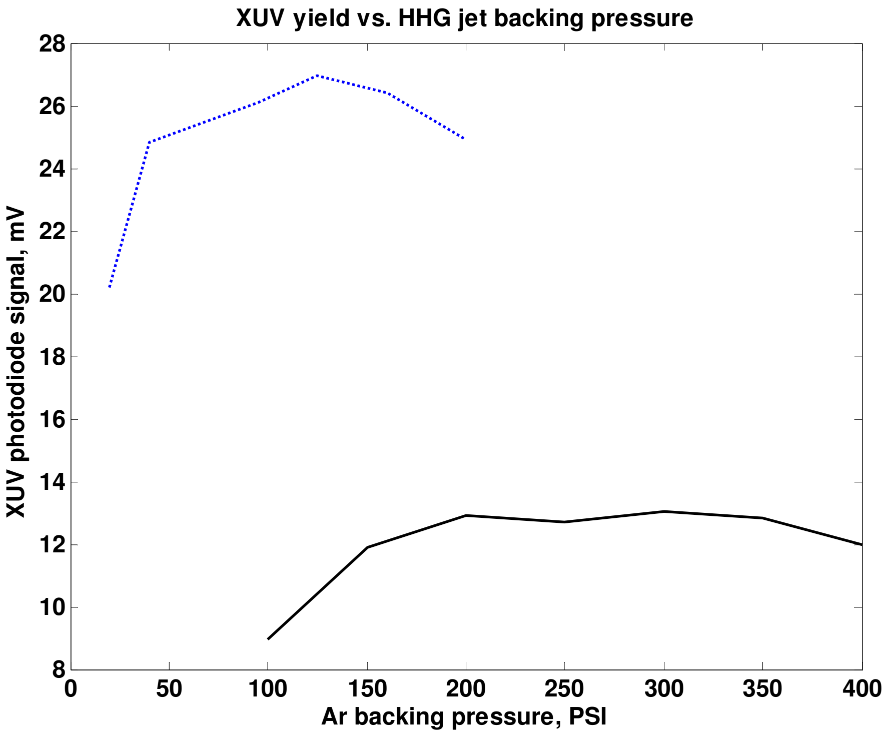

Figure 4.10: Harmonic yield versus argon stagnation pressure. Measurements were made at z=+40 jet-focus position (blue dash) and at z=-80mm (black).

4.2.5 HHG Nozzle distance to laser focus

The measurements presented in section 4.2.3 and 4.2.4 were acquired with the HHG nozzle as close to the laser axis as possible without inducing visible plasma from the nozzle body. For both nozzle types, the harmonic yield drops very rapidly as the nozzle is moved away from the laser axis. Figure 4.11 presents the harmonic yield as a function of nozzle-laser axis distance for an ‘optimized’ longitudinal position z = -50mm, 200PSI argon and 300mJ infrared pulse energy. The decline is significant over a distance comparable to the infrared spot size at that location, suggesting that the gas profile is not uniform over the area in which harmonics are generated.

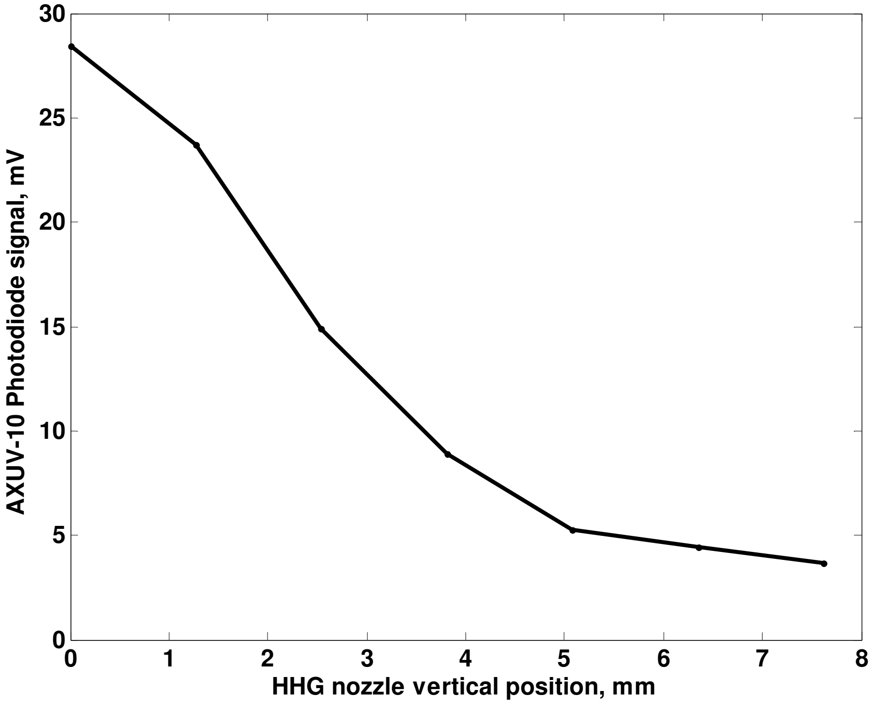

Figure 4.11: Harmonic yield versus nozzle distance from laser axis.

4.2.6 Modified nozzle body

The sensitivity of the harmonic signal to longitudinal and transverse nozzle position described in 4.2.3 and 4.2.5 suggested that improvements could be made to the spatial profile of the HHG gas. With this in mind, a modified nozzle body was designed to produce a more uniform gas distribution, especially along the axis of the gas nozzle itself. The nozzle body consists of a steel block mounted underneath the General Valve Series 9 nozzle, with a 0.25” diameter blind hole centered on the valve nozzle, and a 0.25” diameter through hole cut perpendicular to allow passage of the infrared pulse (Figure 4.12).

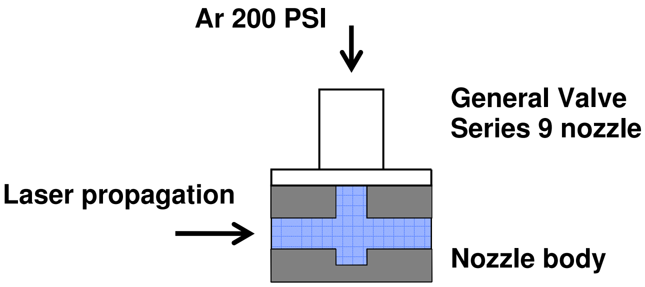

Figure 4.12: Schematic of modified nozzle body.

At the ‘downstream’ longitudinal yield maximum near z= +40mm, the yield with the modified nozzle body was one fifth the yield from the simple jet. At the ‘upstream’ maximum near z= -50mm, the harmonic yield with the nozzle body was more than double the best yield obtained with the simple jet. This improvement required increasing the valve opening time to ~880 microseconds and firing the valve one millisecond before the laser pulse arrived. With the modified body in place, the sensitivity of the harmonic yield to nozzle position was dramatically reduced, with no significant change in yield until the laser begins to clip the edge of the nozzle body aperture. An image of the nozzle body with visible argon plasma produced by the laser is shown in Figure 4.13.

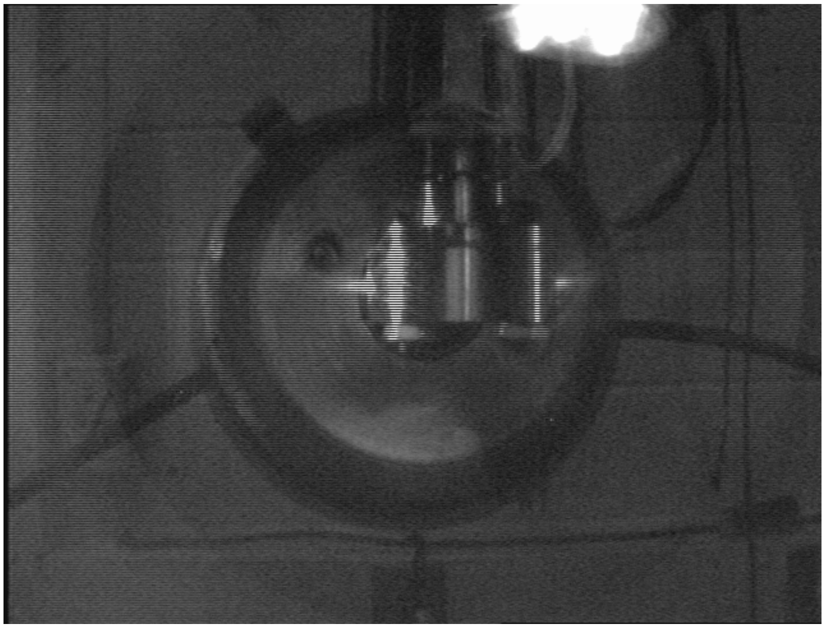

Figure 4.13: CCD image of modified nozzle body with laser plasma visible.

The XUV photodiodes used in this work have absolute calibration standards registered with NIST. Because the XUV energy is delivered as a delta function on the time scale of the photodiode, the signal voltage as a function of time is characteristic of the $(RC)^{-1}$ time of the detector circuit. The capacitance of the photodiode is proportional to its area, so the 1mm by 10mm AXUV-10 diode responds with 10 times the peak voltage in a pulse $1/10^{th}$ as long as that from the 10mm by 10mm AXUV-100. Using the manufacturer's listed value for the photodiode responsivity (0.2 Amperes photocurrent per Watt incident XUV power, or 0.2 Coulomb per Joule) the peak pulse energy of the XUV light delivered to the focus is 1nJ. Accounting for the transmission of the Al filter and the reflectivity of the Sc/Si mirror, this corresponds to a 3×10^{-7} conversion efficiency from the infrared to the 21st harmonic. A sample single-shot trace of the AXUV-100 photodiode signal corresponding to 0.5nJ is shown in Figure 4.14.

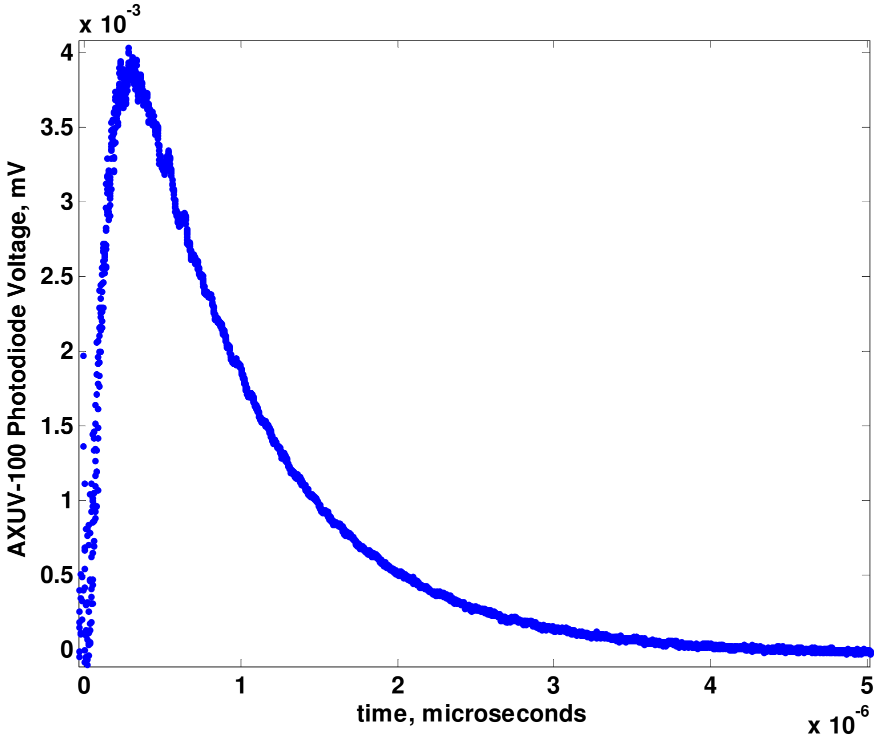

Figure 4.14: XUV photodiode oscilloscope trace

4.2.7 Knife edge spot size measurement

The multilayer mirror is mounted in the target chamber on an encoded micrometer stage [Zymer Inc.] with 2-axis tilts so that the XUV beam waist can be moved with respect to the chamber center. The focal length is of the mirror is 125mm. The mirror is mounted at a small angle (~2º) with respect to the incident XUV light. In order to measure the XUV spot size at the focus, a razor blade was mounted on an encoded micrometer perpendicular to the propagation direction of the XUV beam. The AXUV-10 photodiode was mounted after the razor blade to monitor the pulse energy. The razor blade could by translated in 1 micron steps, to gradually obscure the XUV light from hitting the diode. At each razor position, 200 shots were averaged to produce one data point. The transverse intensity profile is the derivative of the photodiode signal with respect to the razor position. Fitting the profile at best focus with a Gaussian yields an intensity full width at half maximum (FWHM) of 8 microns. (Fig. 4.15).

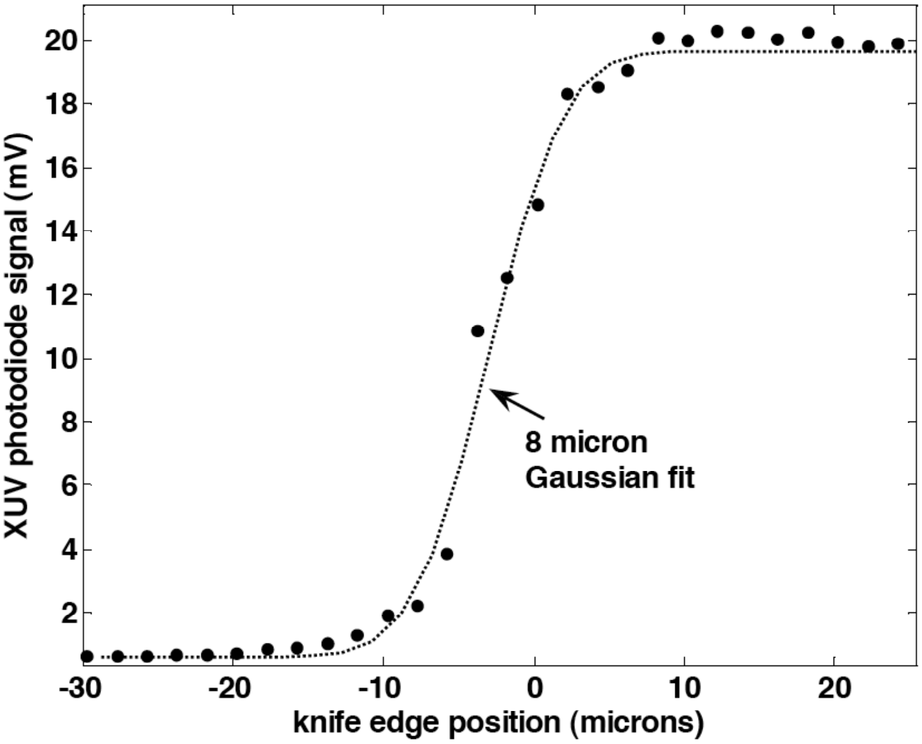

Figure 4.15: XUV spot size measurement

The divergence of the XUV beam near the focus corresponds to a confocal parameter of 800 microns (Fig. 4.16). The diffraction limited spot size (neglecting astigmatism) for 38 nanometer light in this focusing configuration (f/26) is 1 micron, with a confocal parameter of 160 microns, so the spot is about 8x the diffraction limit. For comparison, 800 nanometer light would have a 20 micron diffraction limited spot size and a confocal parameter over 3 millimeters.

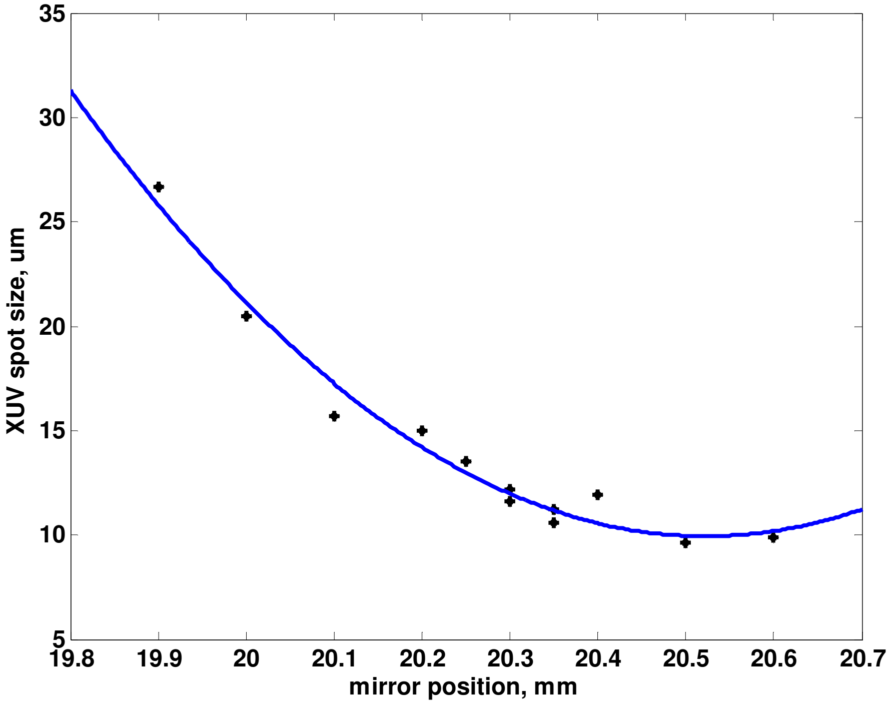

Figure 4.16: Beam waist scan of 21st harmonic

4.3 Estimated intensity of focused 21st harmonic

The intensity of the XUV focus can be estimated using the pulse energy and spot size measurements, with an estimate of the pulse duration. Measurement of the pulse duration is a significant challenge beyond the scope of this work [71]. The harmonics are generated as attosecond pulse trains as discussed in chapter 4, but whether this structure is destroyed by selecting a single harmonic is not clear, as the bandwidth limited duration of individual harmonics is still quite short with respect to infrared laser pulse. We estimate the pulse duration to be 10 femtoseconds [71-75, 39]. Given this estimate, the peak intensity in the focus of the 21st harmonic is about 10^{11} $\mathrm{Wcm^{-2}}$.

4.4 HHG Beamline upgrades

Data from the HHG beamline commissioning suggest that major improvements in yield would require major beamline modifications. Only one third of the available infrared laser energy could be used in the design presented here. The design includes constraints (transmissive infrared focusing optic, 2 meter lens focal length, fold mirror after lens) due to the limited space available and the need for high vacuum in the target chamber. A redesigned beamline using all-reflective optics would remove the infrared energy limits imposed by B-integral accumulated as the compressed pulse passes through the lens. While an off-axis parabolic mirror could be used to focus the infrared, they are not commonly available with focal length longer than 1 meter. Spherical mirrors are commercially available in focal lengths from 1 to 10 meters, and can be mounted slightly off-axis so that the infrared light hits a 45° turning mirror before the spherical mirror, and passes over it on the way to the focus. A hole-drilled turning mirror would allow the spherical mirror to be used on-axis in a very compact beamline layout. After the focusing optic, the beamline should have a straight path as long as possible so that the infrared can diverge enough to avoid destroying the Al filter. This also resolves the issue of damage to the final infrared turning mirror observed in the current design. Large turbomolecular pumps at the harmonic jet and in the infrared-XUV separation region would allow a large HHG gas volume while maintaining tolerable target chamber pressure. Due to the sensitivity of harmonic yield to the nozzle-focus position discussed in 4.2.3, provision should be made to vary the nozzle-focus position continuously over a distance of several infrared confocal parameters. By implementing these modifications, a redesigned HHG beamline using infrared energy over 1 Joule with high conversion efficiency in annular geometry is feasible.

Chapter 5: Time-of-Flight Spectroscopy of XUV Interactions with Noble Gas Clusters

5.1 Time-of-flight spectroscopy of laser-matter interactions

When a large amount of energy is rapidly deposited in a limited volume of material, the material quickly disassembles.[13] Depending on the dynamics of the rapid interaction and the subsequent material relaxation, the energy is distributed among the constituent components (electrons, ions, excited states, radiation field) of the material to varying degree. In the laboratory, high energy density states of matter are created in very small volumes and on very short timescales, due to energetic constraints. Therefore when we study the distribution of energy among the constituents, we observe late-time and/or long-range interaction products. While we do not observe the physical processes of the interaction directly, much can be inferred about the original conditions based on the interaction products. When isolated systems of $10\text{-}10^5$ molecules (hereafter called clusters) are heated to 1-100eV temperature on a femtosecond time scale, thermal equilibrium may not be reached before the system disassembles to the point that electron-ion recombination ceases. This can "freeze" the statistical distribution of ion charge states into the ion ensemble, once densities are low enough that inelastic electron-ion and ion-ion collisions are unlikely. Long range Coulomb forces can still influence the energy distribution of the cluster electrons and ions even after the cluster disassembles. By measuring the charge state distribution of cluster ions and the kinetic energy distribution

---

[13] 'Large amount' here should be taken to mean large with respect to the binding energies of the material involved.

of cluster electrons and ions, we can better understand the condition of the cluster at the end of the energy deposition. This has direct bearing on interesting challenges in modern physics, such as understanding sample damage timescales in x-ray free electron laser biomolecule imaging.

5.1.1 Cluster formation by gas expansion into vacuum

When gas is expanded through a nozzle at high pressure into vacuum, the expansion occurs isentropically and adiabatically, with rapid decrease in temperature and density as the gas accelerates into vacuum. Under proper conditions, condensation can occur in the expanding gas, leading to nucleation and growth of clusters in the jet of gas flowing from the nozzle [77-87]. While an analytic solution for this condensation in generalized nozzle geometry is not tenable, an empirical model put forward by Otto F. Hagena provides useful scaling of cluster size with nozzle parameters [81]. The Hagena clustering parameter Γ^*, which depends on the nozzle opening angle Θ and diameter d, gas species parameter k, temperature T, and stagnation pressure P_0 , predicts the average size of clusters in an expanding gas jet (eqns. 5.1). Values of k for several gases are listed in table 5.1 [80].

$$\Gamma^* = k\frac{(d/Tan\,\theta)^{0.85}}{T^{2.875}}P_0 \qquad (5.1a)$$

$$\langle N \rangle = 33\left(\Gamma^*/1000\right)^{2.35} \qquad (5.1b)$$

Gas Species	k
H_2	184
He	3.85
CH_4	2360
N_2	528
Ne	185
Ar	1650
Kr	2890
Xe	5500

Table 5.1: Gas species parameter k for various gases in Hagena cluster model [80,84].

The Hagena formulation was developed for continuous sources, which require vast pumping speed (many 1000's of liters per second) to maintain the pressure differential between the gas source and the vacuum. Most modern cluster sources use fast pulsed nozzles (e.g. General Valve Series 9, Lavie-Even nozzle) with duty cycle 10^{-6}-10^{-2} so that gas is only injected into the vacuum system when needed, reducing vacuum system demands. When the nozzle open time is comparable to the timescale of an atom's transit through the nozzle body, the equilibrium conditions used to obtain eqns. 5.1 may not be reached, resulting in smaller clusters. Studies of the cluster sizes obtained with pulsed nozzles similar to ones used in this work recommend modification of eqns. 5.1 for pulsed valves when Γ^* is small [83] or when Γ^* is large [82]. In either case the correction comes as a change in the factor outside the parentheses in 5.1b and the power to which the contents of the parentheses are raised:

$$\langle N \rangle = 38.4\left(\Gamma^*/1000\right)^{1.64} \qquad \Gamma^* > 10^4 \tag{5.2}$$

$$\langle N \rangle = 100\left(\Gamma^*/1000\right)^{1.8} \qquad 350 < \Gamma^* < 1800 \tag{5.3}$$

Following [90] in applying the results of [124], the size distribution of clusters within the jet is modeled as log-normal. The abundance of clusters of N molecules is

$$n_{clusters}(N) = \frac{n_{clusters}^{total}}{N\sigma\sqrt{2\pi}} Exp\left[-\left(\ln N - \mu\right)^2 / 2\sigma^2\right] \tag{5.4}$$

where μ is the mean and σ the standard deviation of the logarithm of N. Applying the value σ obtained in [90], the size distribution for <N> ~ 100 is plotted in Fig. 5.1.

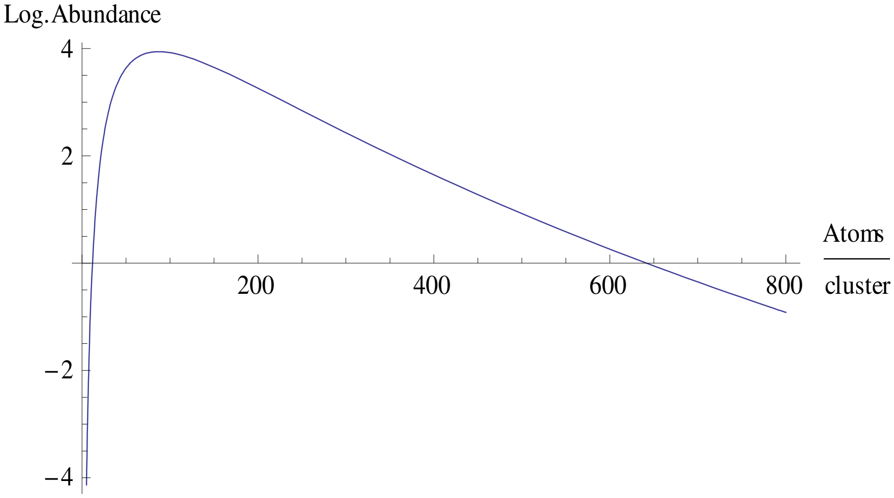

Figure 5.1: Log-normal cluster size distribution with <N> ≈ 100.

5.1.2 Cluster photoabsorption mechanisms

When clusters are exposed to intense coherent light with photon energy below the ionization potential of the cluster constituents, three ionization mechanisms contribute to absorption of laser energy by the cluster [6]. First, the above threshold ionization discussed in chapter 2 generates free electrons and ions in almost the same way as for atoms, with modifications due to the distribution of ionic cores in the cluster. These electrons move in the field of the laser pulse, leaving the cluster to large radiuii before being swept back through the cluster when the laser field changes sign. These electrons tend to heat as they are driven by the laser field while undergoing elastic collisions, and the heated electrons can subsequently acquire enough energy to collisionally ionize atoms in the cluster, the second ionization mechanism. The rate for this collisional ionization can be accurately modeled using the empirical formula by Lotz [97]. Thirdly, free electrons can acquire enough energy directly from the laser field to produce ions if the ponderomotive potential is larger than the binding potential. Collisional heating is the dominant electron ionization process after the first few cycles with intensity sufficient for ATI [6, 93, 96, 108, 110-113]. Most or all (for low-Z atoms) electrons can be removed completely from small clusters by collisional heating on the timescale of the laser pulse.

This picture changes when the photon energy of the applied light is significantly above the ionization potential of the cluster components. The dominant process at early times or low intensities will be single photon ionization. If the intensity is sufficiently high, multiphoton processes will occur, but well within the perturbative regime as described in Chapter 1. Residual electron energy after single photon ionization may be large enough that the ionized electron can ionize another atom immediately, without additional ‘help’ from the laser field. The ponderomotive energy an electron can acquire from the XUV laser field is far too low to contribute to ionization. Auger processes may contribute if the photon energy is sufficiently high. Multiple cluster effects have been described which contribute to ionization in the high photon energy, low ponderomotive potential limit [114-122]. If the electron density reaches $3^{-1/2}n_{crit}$ during the pulse, the Mie cluster plasma resonance condition may be achieved [G. Mie and T. Tajima], leading to a spike in absorption rate. The weak ponderomotive force tends to limit the overall degree of ionization of the cluster after the pulse has passed.

5.1.2.1 Continuum Lowering in Dense Plasmas

When the kinetic energy of the cluster electrons remains low, their density remains high, and the ionization potentials of cluster atoms/ions are reduced due to plasma screening. This 'continuum lowering' results from the fact that plasma electrons are more likely to be found near an ion than in the gaps between ions. It is most significant when the Debye length is short with respect to the atomic spacing in the cluster, the 'ion-sphere' regime [125]. In this regime the electric fields are shielded over distances larger than half an interatomic spacing. The shift in ionization potential can be estimated by assuming that the electron distribution is uniform in a sphere of radius R_{is}:

$$\boldsymbol{R_{is} = \left(\frac{3}{4\pi n_i}\right)^{1/3}} \tag{5.5a}$$

$$\boldsymbol{n_e = \frac{3Z}{4\pi R_{is}^3}} \tag{5.5b}$$

The electrons within the ion sphere experience an attractive force due to the ion at the center, and a repulsive force due to the other electrons:

$$\Delta E_{ion} = \frac{1}{4\pi\varepsilon_0}\int_0^{R_{is}}\left(\frac{Ze}{r}\right)\left(\frac{3Ze}{4\pi R_{is}^3}\right)4\pi r^2 dr = -\frac{1}{4\pi\varepsilon_0}\frac{3Z^2e^2}{2R_{is}} \qquad (5.6a)$$

$$\Delta E_{electron} = \frac{1}{4\pi\varepsilon_0}\int_0^{R_{is}}\left(\frac{Zer^3}{R_{is}^3}\right)\left(\frac{3Ze}{4\pi R_{is}^3}\right)4\pi r^2 dr = \frac{1}{4\pi\varepsilon_0}\frac{3Z^2e^2}{5R_{is}} \qquad (5.6b)$$

Summing (5.6a) and (5.6b) gives the net reduction in ionization potential for a cluster of average charge Z (eqn. 5.7). This should be considered an approximation, because the electron distribution is not totally uniform. For a Xenon cluster of average charge Z=2, this value is ~25 eV.

$$\Delta E_{net} = \frac{1}{4\pi\varepsilon_0}\frac{9Z^2e^2}{10R_{is}} \qquad (5.7)$$

5.1.3 Coulomb explosions

If enough energy is delivered to a cluster in a sufficiently short pulse, all the electrons may be removed “to infinity” before the ions have a chance to move significantly. In this extreme case, analysis of the subsequent ion motion becomes a simple electrostatic problem. The resulting ion kinetic energy spectrum is determined by the radial distribution of the cluster ions, with a sharp cutoff at the maximum energy for ions on the cluster surface:

$$E_{\max} = \frac{4q^2e^2R^2n_0}{3\varepsilon_0} \qquad (5.8)$$

When convolved with the cluster size distribution (5.4), this results in an ion kinetic energy distribution which rapidly rises from zero at the low-energy side (corresponding to ions near the cluster centers, which are not accelerated much.) The energy distribution peaks at a value proportional to the value of E_{max} at the average cluster radius, then falls off at high energy roughly as

$$N(E) = N_{Peak} Exp\left[-{(E - E_{peak})} \big/ {E_{peak}} \right] \qquad (5.9)$$

Substituting the cluster radius as a function of cluster size N into (5.5) and solving for N gives the size N_E (in atom number) of the cluster as a function of its maximum ion energy:

$$N_E = \frac{q^2 e^2 n_i}{3\varepsilon_0} (4\pi n_i)^{-2/3} \qquad (5.10)$$

The kinetic energy distribution of ions from Coulomb explosions averaged over cluster size is then obtained by integrating (5.4) for all clusters which can contribute ions with kinetic energy E as in eqn. 5.7. The averaged spectrum obtained in this fashion is plotted in Fig. 5.2.

$$g(E)dE = \int_{N_E}^{\infty} n_C(N) dN \qquad (5.11)$$

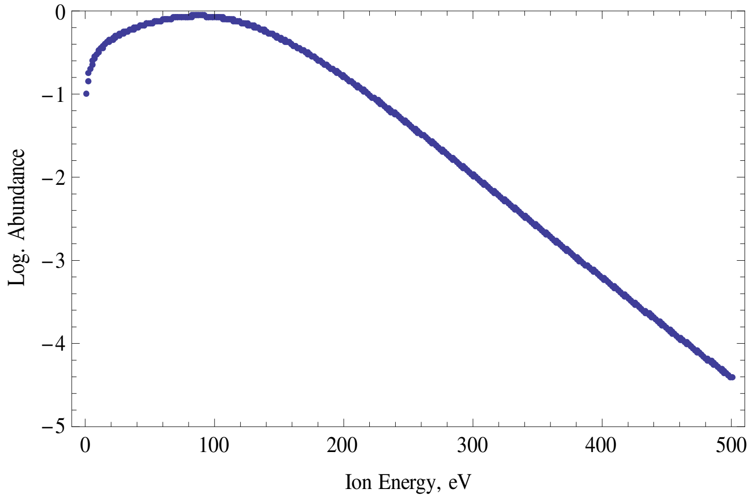

Figure 5.2: Ion kinetic energy spectrum from Coulomb explosion of a log-normal distribution of xenon ions with <N> ≈ 100 and charge 1+.

5.1.4 Hydrodynamic expansion

For large clusters or low laser intensity, not all electrons will be removed from the clusters before the cluster begins to expand. In this case, energy is deposited in the cluster as electron thermal motion via inverse bremsstrahlung [132]. The electron cloud expands due to the added energy, and as it does so creates an ambipolar electric field, dragging the ions along in a hydrodynamic expansion. [6,110,111] If the expansion is energetic enough, the rapid drop in density of electrons and ions will suppress recombination. The quasineutral expansion of a plasma into vacuum has been treated in many papers [91,92, 129-131]. The approach here follows Schmalz [91].

The expansion begins with static ions in the initial geometry of the cluster, but the initial conditions are forgotten at late times. The late time expansion admits self-similar solution in terms of the adiabatic index and a spatial coordinate normalized to the initial sound speed:

$$\xi = {}^{r}\!/\!{}_{c_s t} \tag{5.12}$$

Two differential equations describe the time evolution of normalized number density N and velocity field V in terms of ζ:

$$\frac{dN}{d\xi}(V-\xi)+N\left(\frac{dV}{d\xi}+\frac{\alpha-1}{\xi}V\right)=0 \tag{5.13a}$$

$$\frac{dV}{d\xi}(V-\xi)+\gamma N^{\gamma-2}\frac{dN}{d\xi}=0 \tag{5.13b}$$

Initial conditions in terms of the normalized quantities:

$$V=\sqrt{\gamma}+\xi_0+U \tag{5.14a}$$

$$N=e^{-U/\sqrt{\gamma}} \tag{5.14b}$$

$$U=\left[(\alpha-1)\ \sqrt{\gamma}\ \left(\sqrt{\gamma}+\xi_0\right)/\xi_0\right]^{1/2}(\xi-\xi_0)^{1/2} \tag{5.14c}$$

These equations can be solved for the ion kinetic energy distribution at late times (what we see at the detector) by assuming an initial plasma sound speed c_s and adiabatic index $\gamma = 5/3$ for ideal gas. The late-time ion kinetic energy distribution for xenon, with sound speed c_s corresponding to 8eV electron temperature, is plotted in Fig. 5.3. The ion spectrum diverges at low energy; this divergence should be taken with a grain of salt, because ions with such low energy are likely to recombine without being detected. At high energy, the ion abundance drops off more slowly in a hydrodynamic expansion than in a Coulomb explosion (for equal mean ion kinetic energy.) The drop in ion abundance between 200eV and 400eV is less than an order of magnitude; this contrasts with the Coulomb explosion model of Fig. 5.2, where the drop between 200eV and 400eV is more than two orders of magnitude.

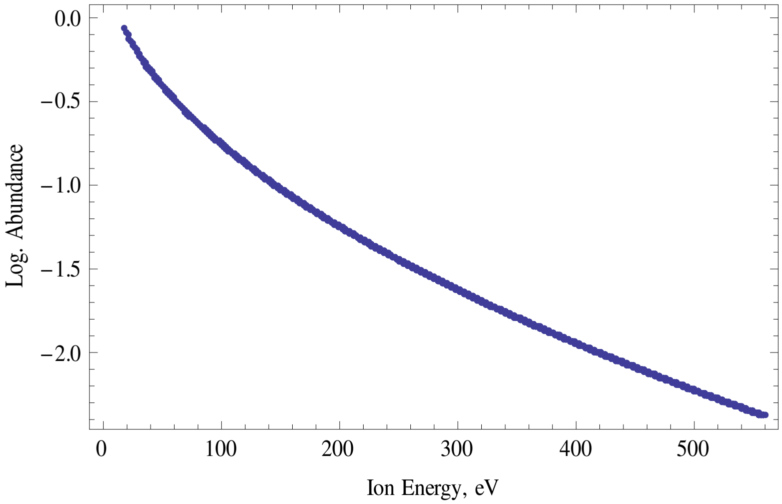

Figure 5.3: Ion kinetic energy spectrum from hydrodynamic expansion of a cluster with initial electron temperature T_e = 8 eV.

5.1.5 Intermediate cases

Purely Coulombic or purely hydrodynamic cluster expansions represent extremes; in the general case, some combination of these effects contribute to the ion kinetic energy spectrum. Complete treatment of the dynamics of the XUV-cluster interaction requires extensive modeling [119,122,126,127]. Qualitatively, the intermediate cases involve a hot quasineutral plasma core surrounded by unshielded charge 'shells' which explode by Coulomb forces, but at much lower energy than the pure case because only ions in the shells contribute to the Coulomb potential. At fixed laser intensity, smaller clusters are more easily stripped of charge, and will be more subject to Coulomb explosion; larger clusters will not be ionized to such a high degree, and will expand hydrodynamically. It is possible to distinguish between the two expansion types by examining the distinct ion kinetic energy signatures.

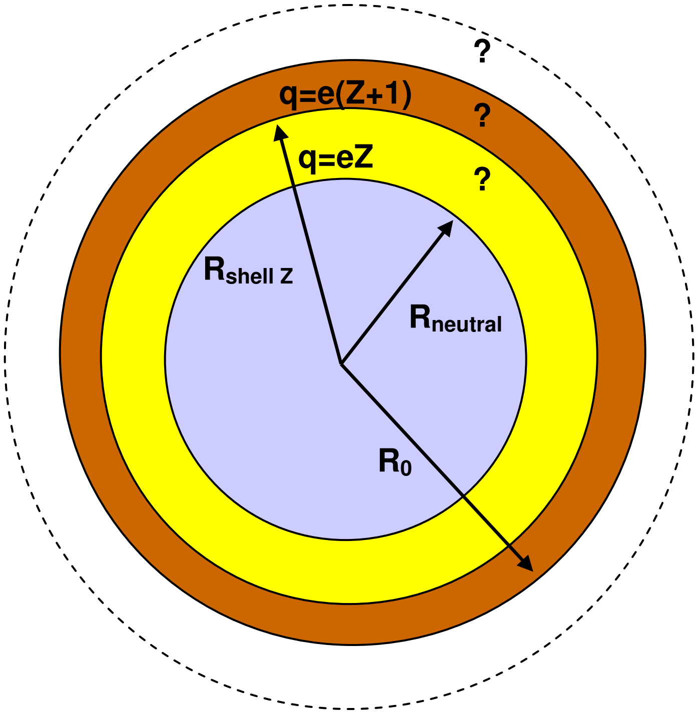

Figure 5.4: Shell model cartoon.

5.2 XUV-cluster interactions on THOR HHG beamline

Target clusters are delivered to the XUV focus by a pulsed valve [General Valve Series 9, Parker Hannefin Corp.] and conical nozzle backed with high purity compressed gas. Experiments were performed with the nozzle mounted either directly above the TOF grids, or above a molecular beam skimmer in a differentially pumped expansion chamber. Gas lines were evacuated to mTorr levels before being filled with target gas. The stagnation pressure in the gas lines is set to produce clusters of the desired average size using a transducer pressure sensor, according to the cluster size model of eqns. 5.2 and 5.3. The maximum line pressure and valve repetition rate are limited by the vacuum requirements to prevent arcing in the MCP, which begins for pressures above ~4 x 10^{-5} Torr. Employing the molecular beam skimmer greatly reduces the gas load on the target chamber, improving TOF resolution at a cost of gas/cluster density in the focus.

The charge-to-mass spectrometry results presented here were obtained using a linear Wiley-McLaren time-of-flight spectrometer [123]. The geometry of the spectrometer with respect to the XUV beam and cluster source is shown schematically in Fig. 5.5. A solid aluminum plate and an annular aluminum plate with 90% transmission gold mesh are held at positive voltage to extract and temporally bunch ions generated in region D_1 by charge to mass ratio q/m. After leaving the acceleration region D_2 ions drift through field-free region D_3 before arriving at a dual microchannel plate (MCP) chevron configuration coupled to a digitizing oscilloscope. The front face of the first MCP is held at 2.2kV for ion detection. The back face of the first MCP is held at 1.1kV potential. Electrons exiting the back face of the first MCP are accelerated across a short (~1 mm) gap to the second MCP, whose front and back face voltages are 1.0kV and 100V, respectively. Electrons exiting the back face of the second MCP impact a collection anode which is conically shaped to reduce capacitative ringing. Appropriate choice of extraction voltages V_1 and V_2 causes ions of identical q/m generated from different locations within region D_1 to arrive at the MCP at the same time ('first-order focusing.') As long as the extraction potential $(V_1 - V_2)/2$ is large compared to the kinetic energy of the ions, the ion collection efficiency can approach 100%.

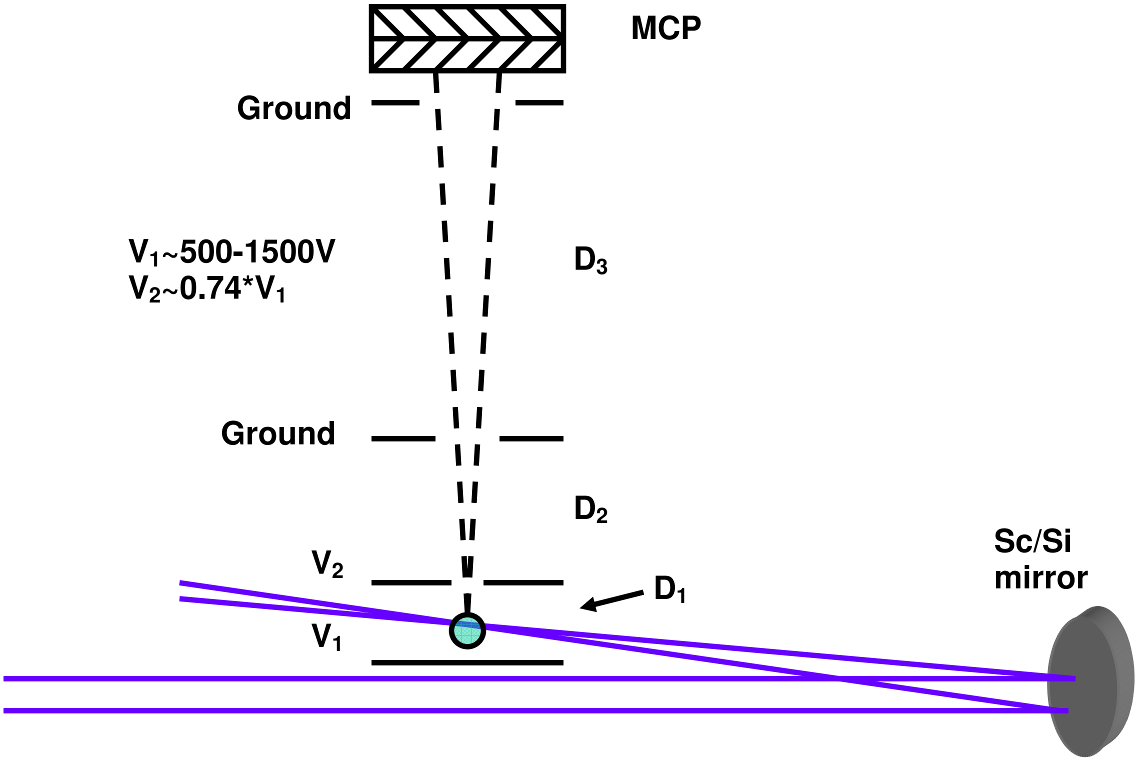

Figure 5.5: Time-of-flight spectrometer schematic.

5.2.1 Ion charge state spectra

In a first series of measurements, xenon cluster charge state TOF spectra were acquired by focusing the 21st harmonic beneath the cluster nozzle without a skimmer. The cluster size was varied by changing the stagnation pressure. The ion signal as a function of mean cluster size is plotted in Fig. 5.6. At low stagnation pressure, ions up to Xe^{3+} are created, consistent with single-photon ionization. As the pressure is increased, ions up to Xe^{5+} appear in significant number, with a much smaller number of higher charge ions up to Xe^{8+}. At the highest pressures a long tail develops in the lowest charges, which we attribute to ion-ion and ion-neutral charge exchange events in the acceleration region

[102-104,106]. The XUV intensity for these measurements is about 10^{11} Wcm^{-2} as discussed in Chapter 4.

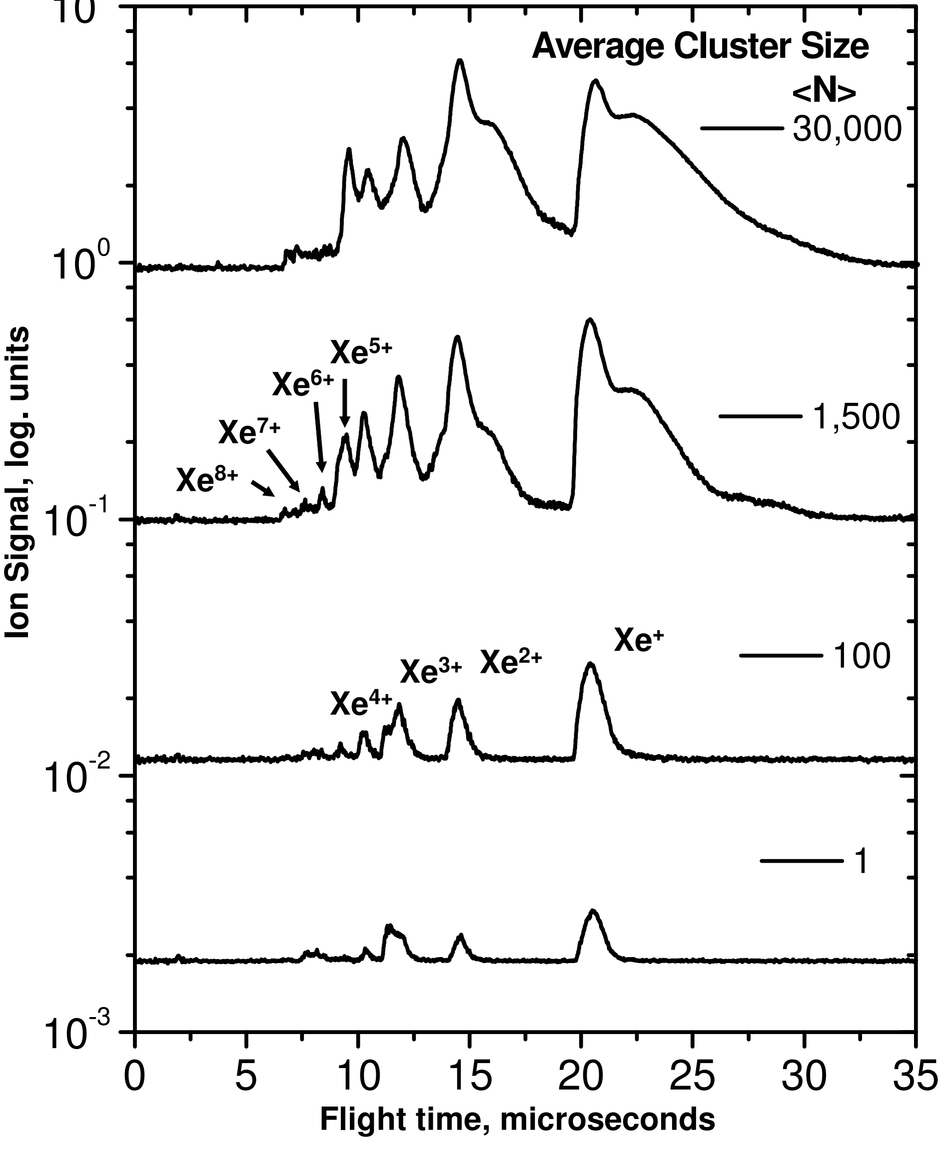

Figure 5.6: Xenon cluster ion species TOF versus cluster size, unskimmed beam.

5.2.2 Ion KE spectra

To observe the ion kinetic energy spectrum, the TOF grids and plates were removed entirely, leaving a field-free region extending from the interaction point to the ground plate in front of the MCP. Without extraction fields, the cluster ions expand spherically. This reduces the ion collection efficiency to the fraction of the solid angle subtended by the detector, in this case about 1%. In order to overcome this loss of signal, the nozzle was positioned directly above the XUV focus for ion kinetic energy TOF measurement. Ion 'hits' on the MCP were read out with a time-delay-counter (TDC) and discriminator in place of the digitizing oscilloscope. Very few ions hit the detector on each shot, so the spectrum was integrated over tens of thousands of shots to obtain an accurate TOF trace. The TDC outputs counts versus bin number, with 1 nanosecond bin size; to obtain an energy spectrum, the ions are rebinned in 1eV intervals. The ion kinetic energy spectrum for xenon clusters with <N>=30,000 is plotted in Fig. 5.7.

The measured ion spectrum peaks at around 80eV, with a long tail including ions above 400eV kinetic energy. Attempts to fit this distribution with a pure Coulomb model as in 5.1.3 were not successful. For the cluster size involved in our experiment, a pure Coulomb explosion with z=1 would result in electron kinetic energy peaking above 2keV (solid red line); no ions with this much energy were observed. Smaller cluster sizes would result in lower energy, but cannot match the observed curve over more than a narrow range. A pure hydrodynamic fit with T=8eV (solid blue line) matches the data over a broad range, only deviating for ion energy below 100eV. We attribute the missing ions to recombination of the slowest ions in exploding large clusters. For comparison, a pure Coulomb explosion of clusters with <N>=100 is plotted as well (dashed red line.) This fits the curve of the low-energy tail well, and may result from the more complete ionization of the smallest clusters [115].

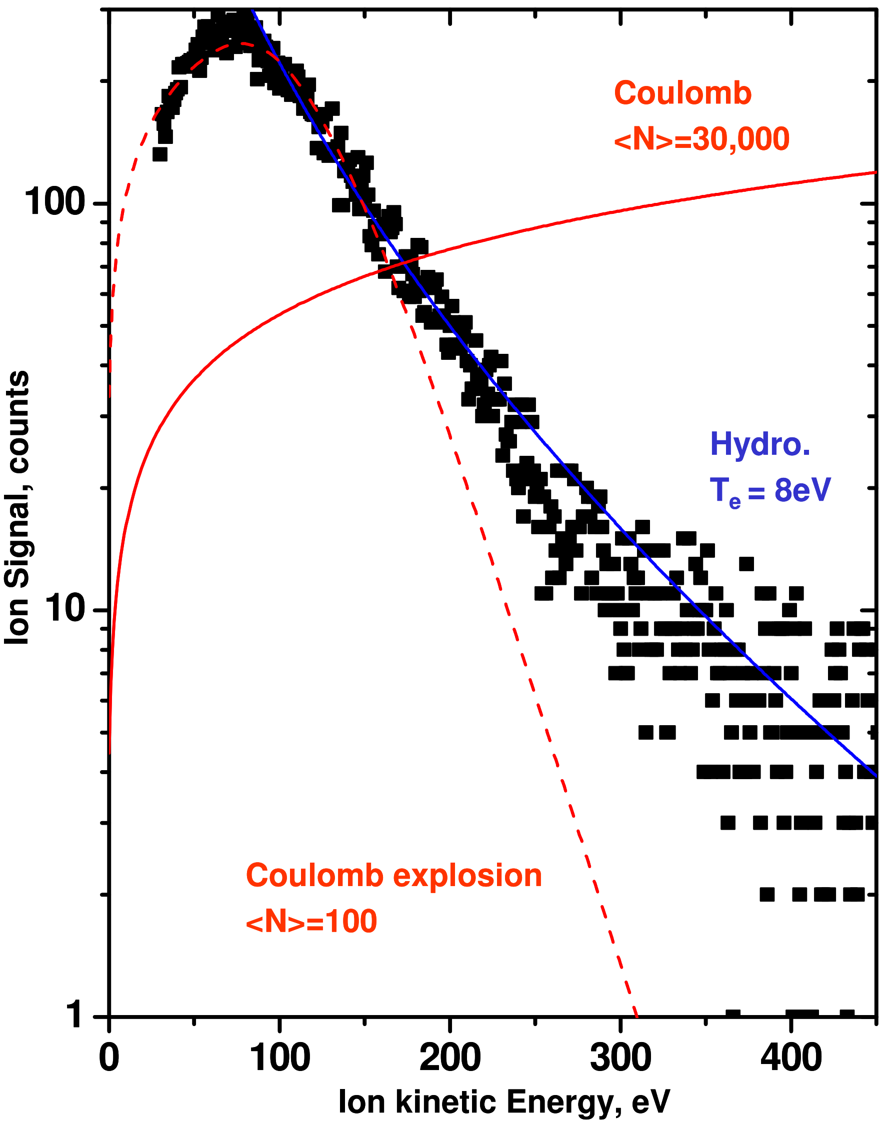

Figure 5.7: Ion kinetic energy spectrum of exploding xenon cluster, <N> = 30.000 atoms. The hydrodynamic fit (blue) increases beyond the plot scale at low energy.

5.2.3 Skimmed Xenon Cluster Spectra

The collisional broadening in the ion charge state TOF spectrum of figure 5.7 prevents direct analysis of ion kinetic energy from peak shapes. To reduce this broadening, a modified cluster beam source was implemented. The modified source consists of the same jet and nozzle used in sections 5.2.1 and 5.2.2, mounted on a vacuum XYZ translation stage in a reentrant chamber above a 250 micron electroformed molecular beam skimmer [Beam Dynamics Inc]. The reentrant chamber is evacuated to ~10 microTorr by a small turbomolecular pump. The nozzle was positioned 1cm above the skimmer, close enough to avoid turbulence at the Mach disk; and the transverse position was optimized to deliver the largest gas impulse to the target chamber on each shot. The skimmer produces a molecular beam of ~1.5mm diameter at the XUV focus (Fig. 5.8). This collimation limits the ionization region, reducing the collection of ions generated outside the XUV focus. The cluster beam is still larger than the XUV confocal parameter, so ions are collected in both high- and low-intensity regions.

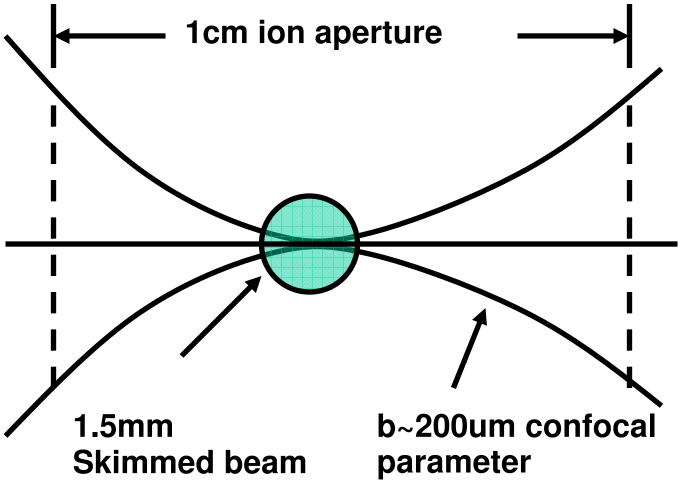

Figure 5.8: Ion extraction aperture, XUV focus and cluster beam intersection.

Employing the skimmer reduced the background pressure in the target chamber by more than an order of magnitude. Typical background pressure consisted of 4 microTorr of argon leakage from the HHG generation region, and 20 microTorr peak target chamber pressure when the target jet is fired at 1200 PSI stagnation pressure. The improvements from the skimmer come at a slight cost, as background gas in the chamber is not 'pushed' out of the way by the start of the cluster pulse.

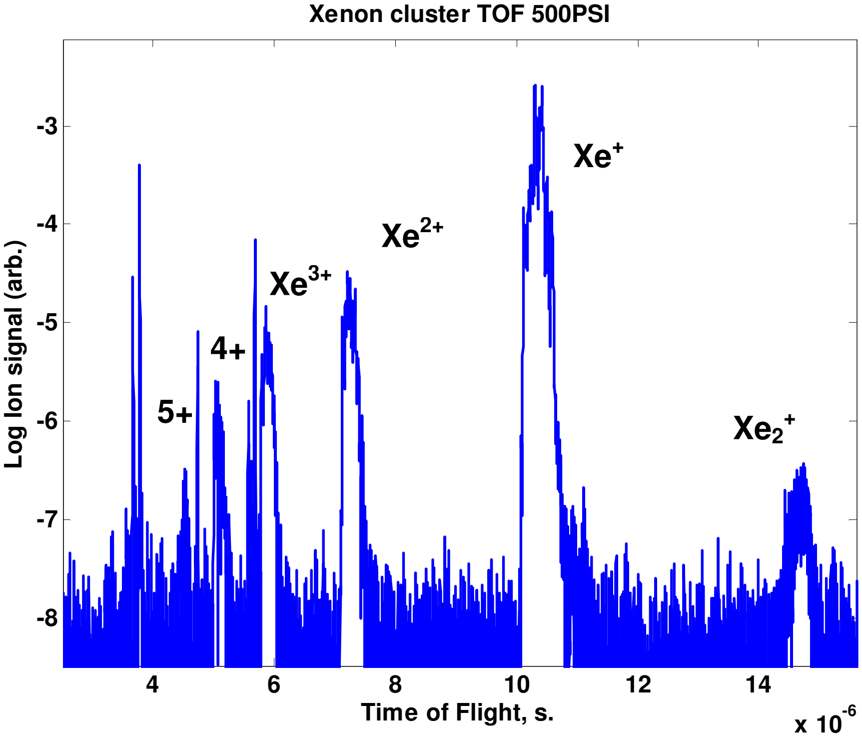

Figure 5.9: Xenon cluster ion species TOF, skimmed beam, 38nm light.

The ion species TOF spectrum of xenon clusters (N ~ 10^5) in the XUV focus is presented in Figure 5.9. With the skimmer in place, we are able to resolve charge states up to Xe^{5+}, and also to observe the Xe_2^+ dimer. Charge states above Xe^{5+} are not resolved above the background gas. Examining the Xe^{1+} peak, isotope structure is clearly resolved (Fig. 5.10, blue line). A Monte Carlo simulation of room-temperature Xe gas with the natural isotope abundance plotted along with the data (black line) reveals that the isotopes are accompanied by side-peaks which do not correspond to any isotope.[14] These peaks appear to result from low-energy Coulomb explosions, possibly from shells as described in 5.1.5. The shift in arrival times of the side peaks corresponds to an ion kinetic energy of ~1eV.

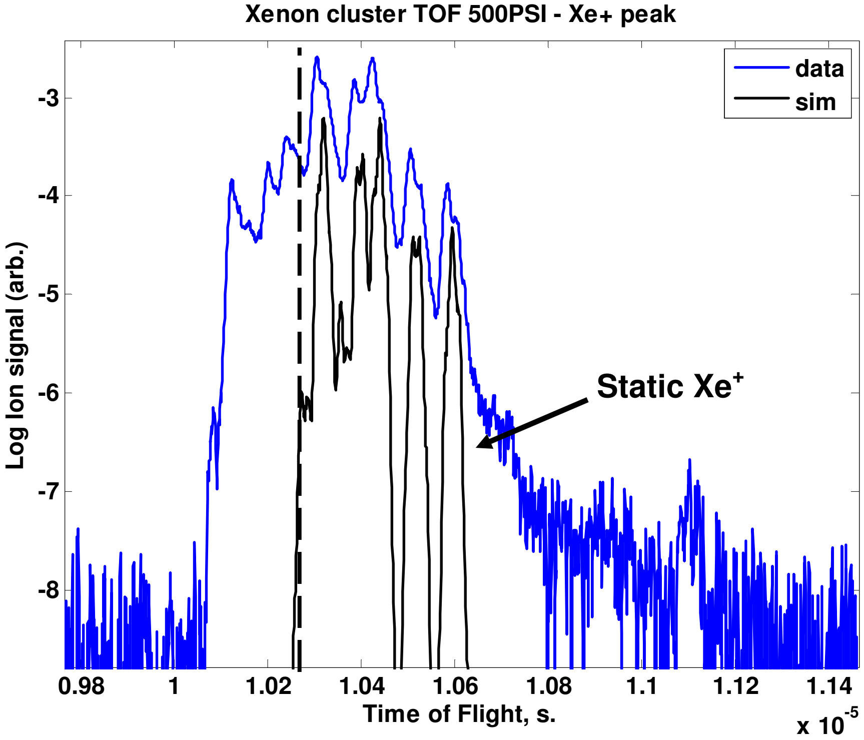

Figure 5.10: Xenon 1+ peak with isotopes and additional side-peaks, 38nm light.

---

[14] See Matlab code in Appendix D.

5.2.4 Infrared Laser-Cluster Ion Charge States

For comparison, charge state TOF spectra were obtained using 800nm light in the same TOF and skimmed cluster source.[15] Because a nonlinear response is necessary to produce even Xe^{1+}, the onset of ionization with laser intensity is far more abrupt than for XUV illumination. The onset of ion production in Xe clusters with <N>=30,000 is shown in Fig. 5.11.

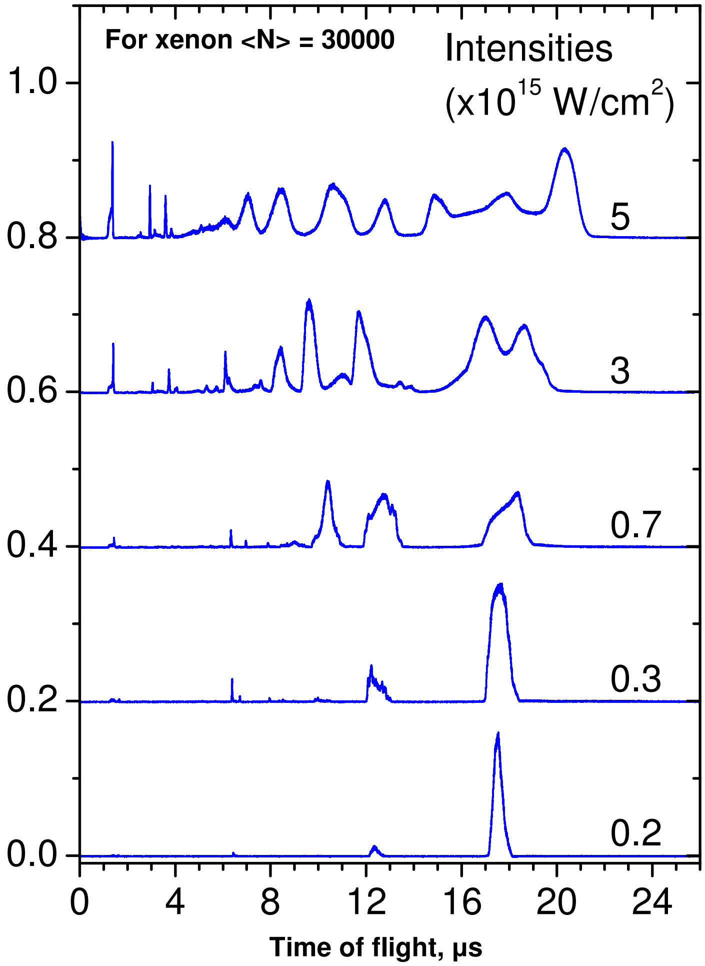

Figure 5.11: Xenon cluster ion species TOF versus cluster size, skimmed beam, infrared light.[16]

---

[15] Data acquired by K. Hoffmann and B. Erk

[16] Figure by B. Erk

As the infrared intensity increases, the narrow Xe^{1+} peak broadens due to ion kinetic energy and eventually splits into three peaks. Ions launched toward the detector with significant energy produce an early 'forward' peak near 15 microseconds in Fig. 5.11. Ions launched away from the detector produce a late 'backward' peak near 20 microseconds. Several ion populations contribute to the central peak at 18 microseconds: monomer gas which ionizes with little KE, cluster ions which are not near the cluster surface, and ions generated at lower intensity away from the focus. A hollow 'center' (3 x 10^{15} Wcm^{-2}) is characteristic of Coulomb explosion, due to the loss of ions launched at large angles with respect to the spectrometer axis. When the intensity is sufficient to produce Xe^{5+} peak, the peak splitting has become so pronounced that the peaks overlap, complicating ion charge identification.[17] The absence of a central peak for the highest ion charge states is typical of Coulomb explosion, because these ions are generated only on the surface of the clusters and gain large KE.

At the highest ion kinetic energies, the observed spectrum is distorted significantly due to the geometrical acceptance of the spectrometer. A 'backward' ion of charge q with kinetic energy greater than $q(V_1 - V_2)/2$ will impact the first TOF extraction plate and will be lost, also ions with too much velocity transverse to the TOF axis. Backward ions occupy the interaction region far longer than forward ions, and are thus more prone to collision with other ions and electrons producing charge exchange or neutralization; this is apparent in Fig. 5.11 for Xe^{1+} and Xe^{2+}, which initially is biased in favor of forward ions (0.3 x 10^{15} Wcm^{-2}) but at higher intensity favors backward ions (0.7 x 10^{15} Wcm^{-2}). In general, the higher an ion's energy the more likely it is to hit a surface other than the MCP detector when the extraction grids are employed.

---

[17] The peak overlap can be suppressed by using larger exstaction voltages V_1 and V_2. The voltages in Fig. 5.11 are the same as those in Fig. 5.6.

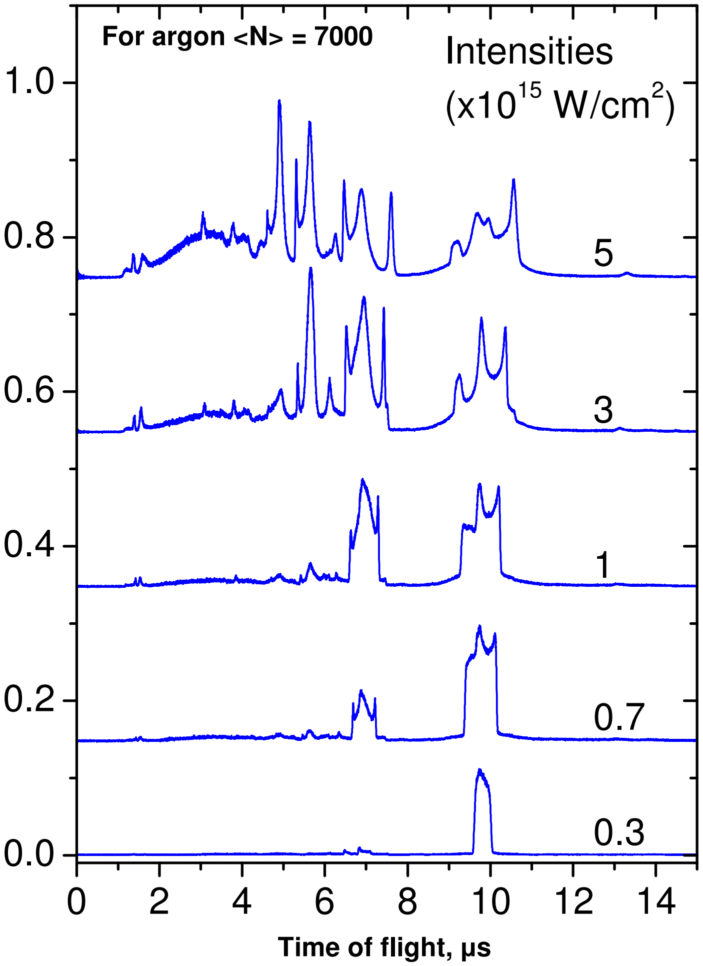

Figure 5.12: Argon charge state spectrum with Coulomb splitting. 800nm excitation.[18]

The trends in cluster ion kinetic energy observed in infrared interactions with xenon are also seen in argon clusters. Ion charge state spectra of argon clusters were obtained as a function of infrared intensity (Fig. 5.12). At the threshold for the production of Ar^+ and Ar^{2+}, the spectrum is biased in favor of the 'forward' peak. At higher intensity, charge exchange interactions bias the peak shape of the lowest ion charges in favor of the

---

[18] Figure by B. Erk

‘backward’ peaks. The loss of ions launched with large radial velocity is large compared to xenon; this is seen in the isolated on-axis backward ions into a distinct peak at the highest intensities. Recombination of backward-directed ions Z^{n+1} causes the enhancement of the backward peak of ions Z^{n}.

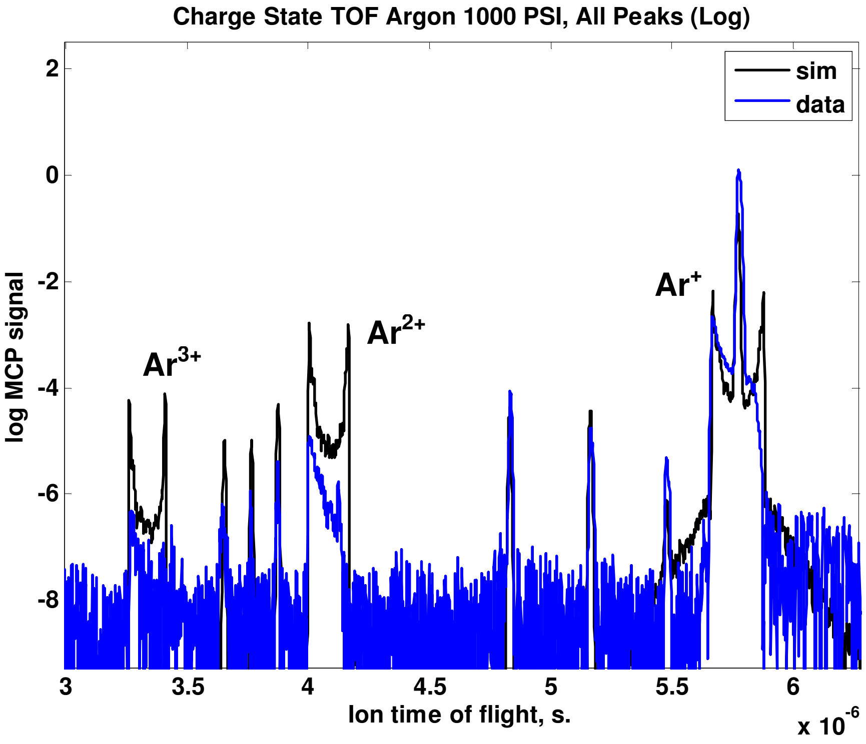

Figure 5.13: Argon cluster ion species TOF versus cluster size, skimmed beam, XUV excitation.

5.2.5 Argon Ion Charge State Spectra

Argon clusters simplify the analysis of peak spread, due to the dominance of the ^{40}Ar isotope (99.6%). The highest charge state observed in significant quantity in our measurements is Ar^{2+}, whose production from neutral Ar requires more than 43eV total energy (Fig. 5.13). A weak peak at the correct arrival time for Ar^{3+} was not conclusively resolved over the background ion signal. Figures 5.14 and 5.15 focus on the Ar^{1+} and Ar^{2+} peaks, respectively. The $^{36}Ar^{1+}$ isotope is seen at the left in figure 5.14; the peak to the left in Fig. 5.15 comes from H_2O at q/m=18. The black lines in Figures 5.13-5.15 are the results of TOF simulations using the Matlab code in Appendix D.

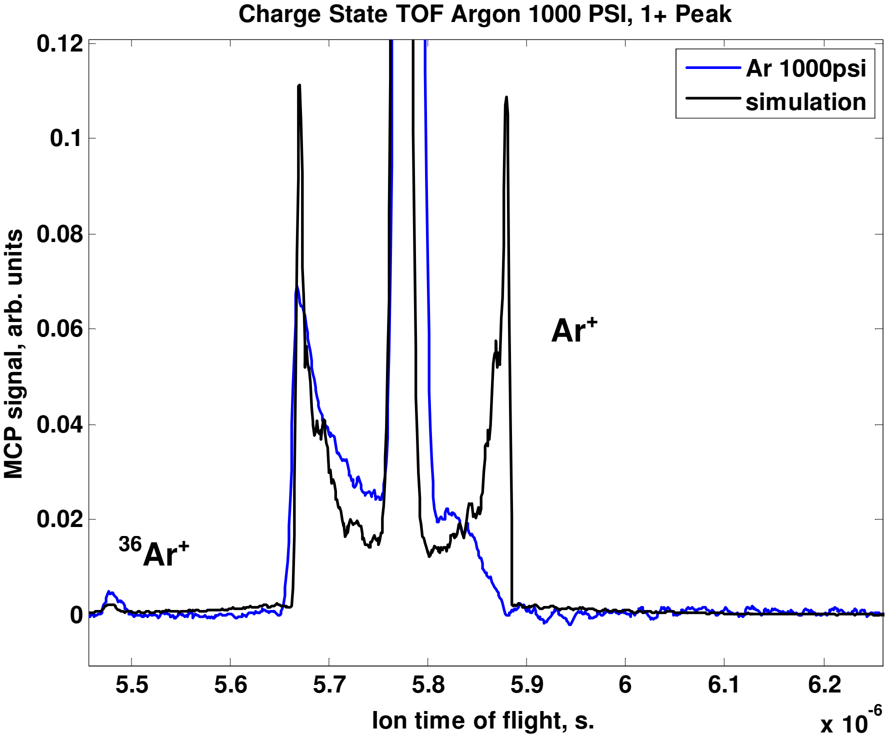

Figure 5.14: Argon 1+ peak with isotopes and additional side-peaks. XUV excitation. 36Ar isotope visible on left side of figure.

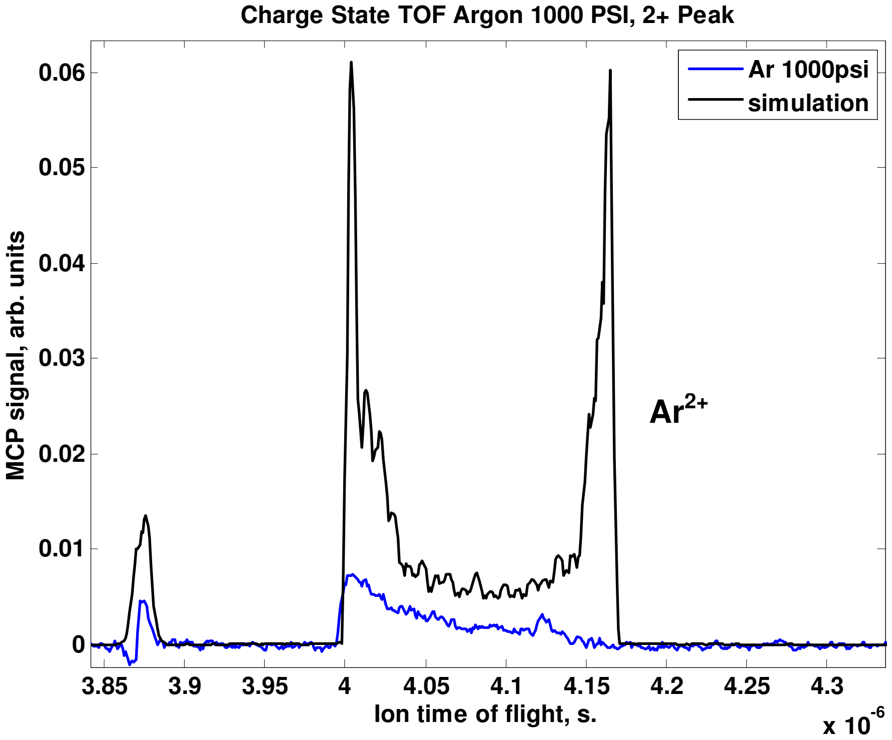

Figure 5.15: Argon 2+ peak with isotopes and additional side-peaks. XUV excitation.

5.2.6 Electron KE spectra

For electron kinetic energy mesurements, the gold mesh was removed, but the plates were left in place. The first plate blocks the large number of electrons generated by single photon ionization of background gas by the XUV beam before it hits the Sc/Si multilayter. The second, annular plate limits the extraction region to a cylinder of ~1 cm length and 200 micron diameter. The extraction region is defined by the intersection of the annular plate acceptance with the XUV beam path, and has the XUV focus at its center. A cone of 10 layers of rolled Mu-metal foil [MuShield Co.] suppresses the earth's magnetic field in the drift region.

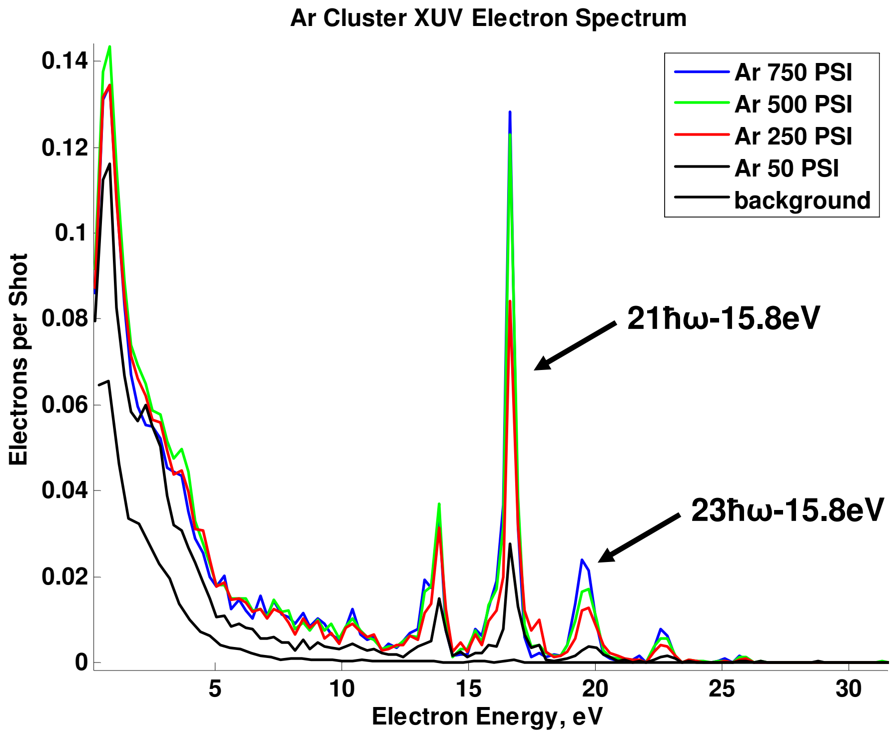

Figure 5.16: Argon cluster electron spectrum. XUV excitation.

The electron kinetic energy spectrum of argon clusters reveals the presence of sideband harmonics in the XUV focus, as the reflectivity of the Sc/Si mirror is significant for harmonics adjacent to the 21st (Fig. 5.16). A large, low-energy background below 5eV could not be distinguished from the background signal when no target gas was injected (black dashed line.) No electrons above 30eV are observed. Because the TOF is mounted in the plane of the polarization of the laser, electrons from monomer ionization may dominate the cluster signal.[19]

---

[19] Electrons from monomer ionization are scattered primarily along the polarization of the ionizing radiation, while electrons from cluster interactions are expected to be emitted isotropically.

Xenon cluster electron kinetic energy spectra tell the same story as argon, with more to learn about the harmonics present in the focus than about the cluster interaction. In this case, the peak resulting from each harmonic is split in two due to the 5s/5p ground state energy level splitting in xenon. Again, no electrons with energy significantly higher than (N*ħω-I.P.) are observed. The electron spectrometer resolution in the 10-30eV range is between 0.2 and 1.32eV, bounded by the peaks observed in Figs. 5.16 and 5.17.

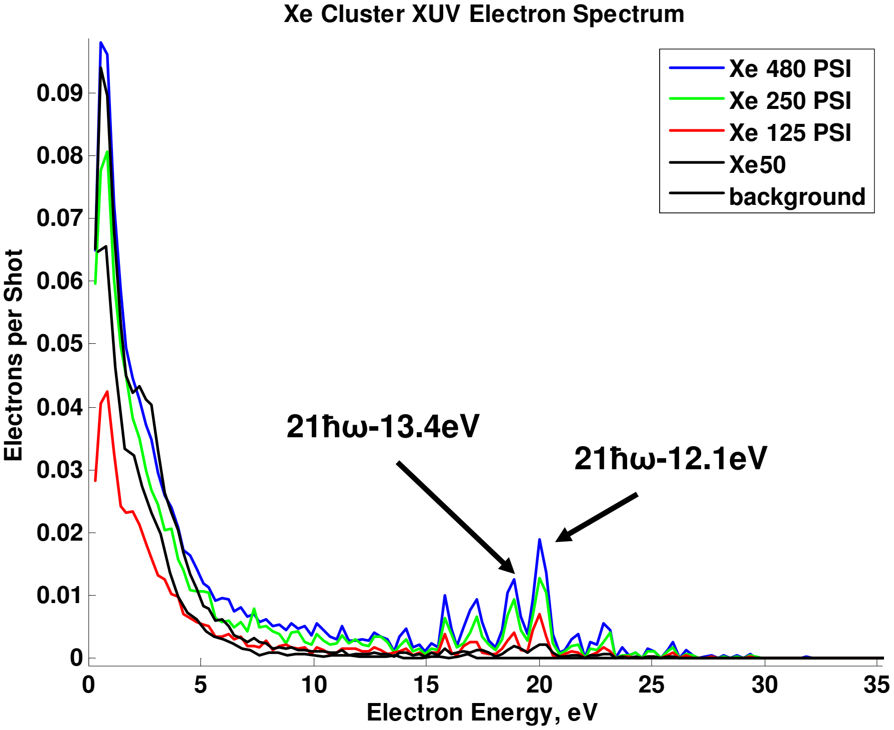

Figure 5.17: Xenon cluster electron spectrum. XUV excitation.

5.3 Comparison of ion charge states with ion kinetic energy spectrum

This ion energy spectrum is strong evidence that near quasi-neutral nanoplasmas are formed in our XUV pulse irradiation of the Xe clusters and that the explosion mechanism is not Coulomb explosion but instead hydrodynamic expansion. A temperature of 8 eV is consistent with the amount of heating we expect by inverse bremsstrahlung (IB) in the XUV field, which we have estimated by calculating the electron heating using the usual IB formulae for high energy photons [94,132]. More mysterious is the production of high charge states under these conditions. The equilibrium charge state distribution found by numerical solution of the Saha equations for this density and 8 eV temperature is Z~2.4. The calculated charge state distribution has no significant number of ions with charge greater than 3+. So it seems that collisional ionization alone cannot explain our observations. When this average charge state is applied to the ion-sphere regime continuum lowering formula eqn 5.7, the ionization potential will be lowered by about 35eV. This would be sufficient to lower the ionization potential of Xe^{4+} sufficiently (where $I_p \approx 60$ eV) to allow direct photo ionization up to Xe^{5+} (as well as the charge states up to this point). An estimate of the photoionization cross section of the continuum lowered potential of Xe^{4+} indicates that a high degree of photo-ionization is possible in our XUV pulse. Likewise, the production of Ar^{2+} is made possible when continuum lowering is considered.

The presence of a small number of charges states with Z=6-8+ can then be explained by non-equilibrium collisional ionization of the Xe^{5+} ions produced rapidly (~20 fs) by photoionization during the XUV pulse by the hot tail of the 8 eV electron distribution. Using the usual Lotz formula for the collisional ionization cross section of the ions [97] with ionization potentials corrected by continuum lowering and integrating this cross section over an 8 eV Maxwellian, we calculate that roughly 5% of Xe^{5+} ions can be collisionally stripped up to Xe^{8+} during the ~1.5 ps time period after the the XUV pulse has passed (the time for our 15 nm, 8 eV clusters to expand hydrodynamically to roughly twice their initial radius.) So the presence of small numbers of Xe 6+ to 8+ in our data can be explained by electron collisional ionization from the photo-ionized Xe^{5+}.

5.4 Conclusions

In summary, we have observed experimentally studied the explosions of large Xe clusters when irradiated by intense, femtosecond pulses of XUV radiation produced by high order harmonic conversion of a Ti:sapphire laser. We find that the ion spectrum of the explosion is completely consistent with that of the expansion of a quasi-neutral plasma with electron temperature of 8 eV and inconsistent with a Coulomb explosion. We find that charge states up to 5+ observed in these explosions are produced by photoionization of ions whose ionization potentials have been depressed by plasma continuum lowering and that a small fraction of ions are further stripped by non-equilibrium electron collisional ionization.

By exposing clusters of noble gases to intense XUV pulses, we have produced ions with charge states and kinetic energy far above the single-photon limit. These interactions result from the collective response of nanoscale clusters to the intense applied field. Ion kinetic energy spectra reveal that a hydrodynamic model is appropriate for the expansion of clusters exposed to intense short-wavelength radiation. This result indicates that a thermalized-electron model is more appropriate than a vertical-ionization model for ion dynamics in the short wavelength limit.

Appendix A: Mathematica modeling of Harada VLS grating

```
Ω=1/(1200000);R=5649;b2=-20;b3=455.8;b4=-11840;d=50;α0=87;

σ=(Ω) /(1+2 b2w/R+3b3w^2/R^2+4b4w^3/R^3);

β=(180/Pi) ArcSin[λ/σ-Sin[α]];

βtest=β/.{w→0,λ→ 20 10^-9,α→ α0 Pi/180}//N

β1=.254+β/.{w→-d/2,α→ (α0+.298-.254) Pi/180};

β2=-.254+β/.{w→d/2,α→ (α0-.339+.254) Pi/180};

y=(1/Tan[β1 Pi/180]+1/Tan[β2 Pi/180])/(1/Tan[β1 Pi/180]-1/Tan[β2 Pi/180]) (d/2);

x=(-1/Tan[β2 Pi/180])(y+d/2);

ParametricPlot[{y,x},{λ,5 10^-9,50 10^-9},PlotRange→{{233,237},{25,75}},
 AspectRatio→ 1/GoldenRatio,AxesLabel→{"z, mm","y, mm"}]
```

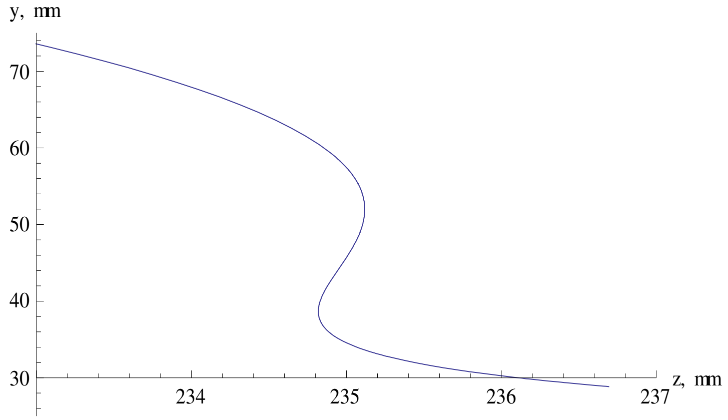

Appendix B: Mathematica modeling of Coulomb Explosions

```
(*define fundamental constants of nature*)

c=2.998*10^8;
hbar=1.054*10^-27;
Navo=6.023*10^23;
echarge=1.602*10^-19;
epsilon=8.854*10^-12;
masse=9.109*10^-31;
kboltz=1.381*10^-23;

(*properties of Xe clusters*)

MXe=0.131/Navo;
rvander=0.216 10^-9;
nliquid=0.74 (4 Pi/3)^-1 rvander^-3;

(*Hagena parameter and cluster size*)

k=5554;
d=750;                    (*nozzle diameter in micron*)
T=300;                    (*Temperature in Kelvin*)
P=8 (1000/14);    (*pressure in mbar = (1000/14)*(pressure in PSI) *)

gammastar=k (d)^0.85( T^-2.29) P

Naverage=38.5(gammastar/1000)^1.65

radius=(3 Naverage/(4 Pi nliquid))^(1/3);

q=1;  (* ion charge *)

Emax = (q^2 echarge (2 radius)^2 (nliquid))/(3 epsilon)
(*Max Ion energy of average cluster, in Electron Volts*)

alpha=(q^2 echarge^2 nliquid)/(3 epsilon) (4 Pi nliquid/3)^(-2/3);

μ=Log[Naverage];

σ=μ/10;

nTot=1000000;
```

```
numcluster=(nTot/(natoms σ (2 Pi)^0.5)) Exp[-(Log[natoms]-μ)^2 (2 σ^2)^-1]

Plot[Log[10,numcluster],{natoms,5,0.8 10^3}, {AxesLabel→{Atoms/cluster, Log. Abundance}}]
```

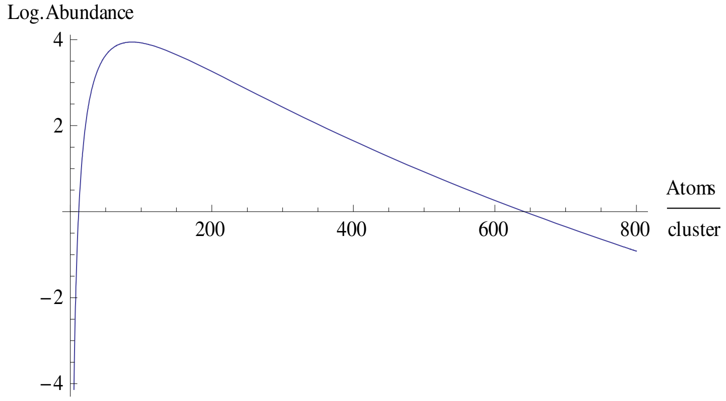

```
NIntegrate[numcluster,{natoms,10,Infinity}]

Estep=echarge;

Gee=Table[NIntegrate[numcluster,{natoms,(j Estep/alpha)^1.5,Infinity}],{j,5}];

Feed=Table[2.4+Log[10,(i Estep)^0.5 NIntegrate[numcluster,
      {natoms,(i Estep/alpha)^1.5,Infinity}]],{i,500}];

ListPlot[Feed,PlotRange→{Full,{0,-5}}, Frame→True,
 FrameLabel→{"Ion Energy, eV","Log. Abundance"}]
```

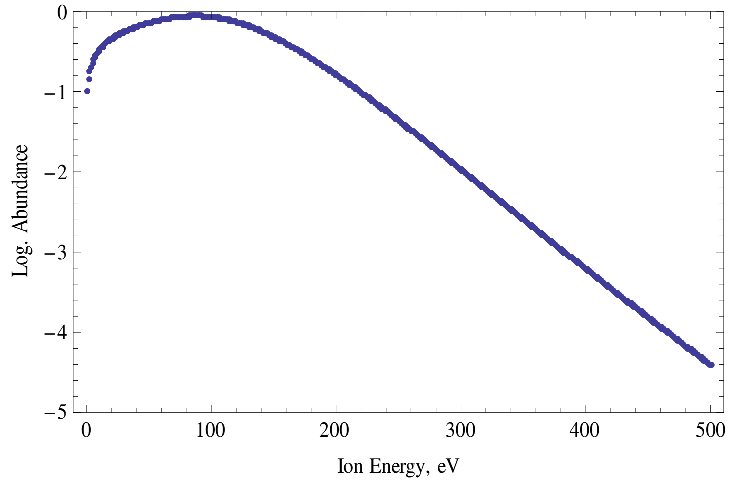

```
Export["clustrjr.txt",Feed,"CSV"]
```

Appendix C: Mathematica modeling of Hydrodynamic Expansion

```
(*  Ion charge state and cold/hot temps*)

z=2;
tc=100 1.602 10^-19 ;
th=800 1.602 10^-19 ;

(*  Ion Mass*)

mi=N[0.1313/(6.02 10^23)];

(*   The following is Schmalz' 1985 Phys. Fluids paper eqns 15-17             *)
(*   Initial conditions; adiabatic index g, dimensionality a, sound speed cs  *)

g=5./3.;
a=3.;
temp= 8 1.602 10^-19 ;

(*   Sound speed taken from temp                                              *)

cs=(z temp/mi)^(1/2);
so=1/10^8;
d=0.1` so;

u[s_]:=N[((2 g^0.5 (g^0.5+so))/so)^0.5 (s-so)^0.5];

vi[s_]:=N[g^0.5+so+u[s]];

ni[s_]:=N[Exp[-u[s] g^-0.5]];
```

```
Plot[{u[s],vi[s],ni[s]},{s,so,10 so},{AxesLabel→{"s","value"}}]
```

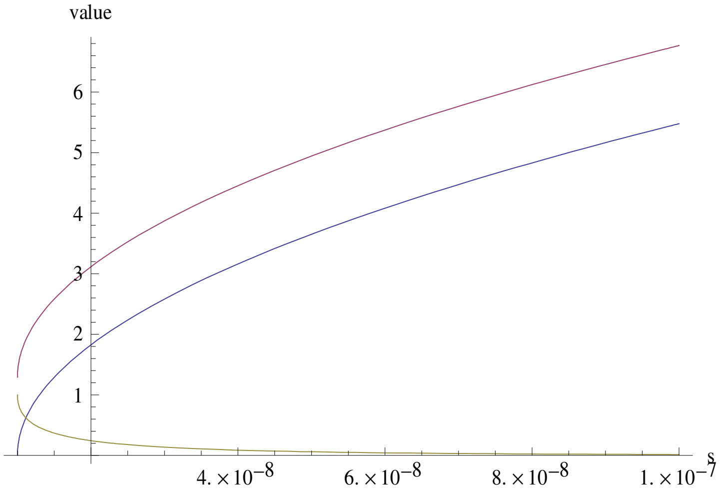

```
(*  define a useful time scale related to cluster size    *)

diameter=5 10^-9;
tau=diameter/cs;
sf=5;

(*   Integrating the equations from R.F. Schmalz 1985 PoF paper              *)
(*   these are equations 3-4 and 15-16, spherical nonisothermal and s~so     *)
(*   s:=x/(cs t) is the self-similar parameter                                        *)
(*   fv is velocity field normalized to the sound speed cs                          *)
(*   fn is the normalized density field                                               *)

sol=NDSolve[{fn'[s] (fv[s]-s)+fn[s] (fv'[s]+(2/s) fv[s])==0,
   fv'[s] (fv[s]-s)+g fn[s]^(g-2) fn'[s]==0,
   fv[so+d]==g^.5+so+u[so+d],
   fn[so+d]==Exp[-u[so+d]/g^.5]},{fv,fn},{s,so,sf}];

(*  Export the energy and F (E)dE for the solution near so               *)

stepsize=so/100;

Energ=Table[(0.5 mi cs^2(vi[stepsize i+so])^2)/(1.602 10^-19),{i,1500}];
Abund=Flatten[Table[Re[ni[stepsize i+so]]/.sol,{i,1500}]];

Export["hydroenergy.txt",Energ,"CSV"];
Export["hydroabund.txt",Abund,"CSV"];

LogIonKEspectrum=Transpose[{Energ,Log[10,Abund]}];
```

```
ListPlot[LogIonKEspectrum,Frame→ True,FrameLabel→{"Ion Energy, eV","Log. Abundance"}]
```

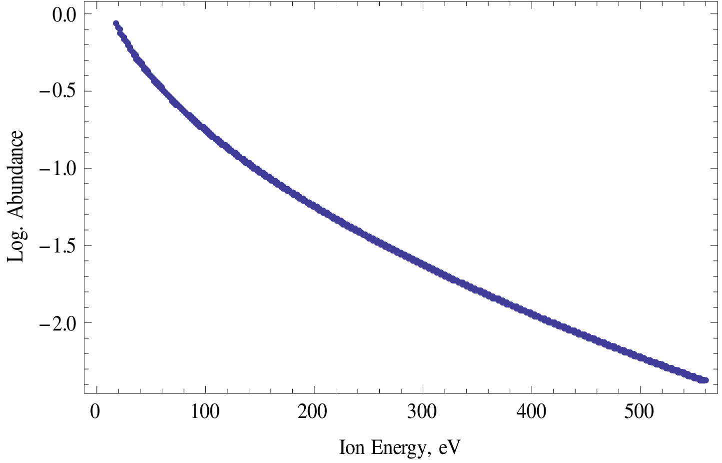

Appendix D: Matlab modeling of TOF ion propagation

```
% physical constants
e=1.602e-19;
u=1.661e-27;
k=1.381e-23;
epsilon=8.854e-12;
% TOF parameters
d1=20e-3;d2=51e-3;d3=317e-3;
V1=1437;V2=1173;
% timestep and tfinish
tstep=1e-9;
numsteps=2e4;
tfinish=tstep*numsteps;
numsets=5;
results=[tstep*(1:numsteps);zeros(1,numsteps)];
%initials=zeros(sum(popmat(:,6)),2);
for h=1:numsets,
   % I) Ion population of TOF
   % popmat(i,:)=[centroid width (temp or coul..radius) mass charge N switch]
   popmat=[8e-3 1e-3  2.5e-2   40 1 2e5  0;...
      8e-3 1e-3  2.5e-2   80 1 1e3  0;...
      8e-3 1e-3  2.5e-2   36 1 670  0;...
      8e-3 1e-3  2.5e-2   38 1 130  0;...
      8e-3 1e-3  3.4e-2   1  1 2e3  0;...
      8e-3 1e-3  3.0e-2   2  1 2e2  0;...
      8e-3 1e-3  2.5e-2   32 1 4e3  0;...
      8e-3 1e-3  2.5e-2   28 1 4e3  0;...
      8e-3 1e-3  2.5e-2   16 1 2e3  0;...
      8e-3 1e-3  2.5e-2   17 1 2e3  0;...
      8e-3 1e-3  2.5e-2   18 1 4e3  0;...
      8e-3 1e-5  18+h     40 1 2e5  1;...
      8e-3 1e-5  18+h     40 2 8e4  1;...
      8e-3 1e-5  18+h     40 3 2e4  1;...
      8e-3 1e-5  5       40 1 4e4  2;...
      8e-3 1e-5  5       40 2 2e3  2;...
      8e-3 1e-5  5       40 3 1e3  2;...
      ];
   % Turn ion population popmat into statistical representative set
   % inition
   % Fill up mass and charge column
   N=popmat(:,6);
```

```
Ndone1=0;
Ndone2=0;
mqcount=0;
inition=zeros(sum(N),5); % inition=[x0 v0 q m vradial]
tic
for j=1:size(popmat,1),
   % Fill up mass and charge columns
   inition((1+mqcount):sum(N(1:j)),4)=popmat(j,4);
   inition((1+mqcount):sum(N(1:j)),3)=popmat(j,5);
   mqcount=mqcount+N(j);
   %
   % Fill up position column
   Ntot=popmat(j,6);            % how many ions in j
   Nfull1=0;
   x0=popmat(j,1);             % Centroid positon of j
   x1=popmat(j,2);             % 1/e^2 halfwidth of ion population
   i=1;
   while Nfull1<Ntot
      x=(rand(1)-0.5)*6*x1;p1=rand(1);
      P1=exp(-0.5*x^2/x1^2);
      if P1>p1,
         inition(i+Ndone1,1)=x+x0;
         Nfull1=Nfull1+1;
         i=i+1;
      end
   end
   Ndone1=Ndone1+Ntot;
   %
   % Fill up velocity columns for thermal distributions
   if popmat(j,7)==0,
      Nfull2=0;
      m=u*popmat(j,4);
      T=popmat(j,3)*e/k;           % Temperature of j population in eV
      vtherm=(3*k*T/m)^0.5;        % thermal velocity
      l=1;
      B=(2*k*T/m)^-0.5;
      while Nfull2<Ntot
         v=(rand(1)-0.5)*6*vtherm;p2=rand(1);
         vradial=(rand(1)-0.5)*6*vtherm;pr=rand(1);
         P2=exp(-(B*v)^2);Pradial=exp(-(B*v)^2);
         if P2>p2,
            if Pradial>pr
               inition(l+Ndone2,2)=v;
               inition(1+Ndone2,5)=vradial;
               Nfull2=Nfull2+1;
```

```
              l=l+1;
           end
        end
     end
  end
  %
  % Fill up cluster Coulomb explosion columns
  if popmat(j,7)==1,
     Nfull2=0;
     m=u*popmat(j,4);
     q=e*popmat(j,5);
     r_guess=popmat(j,3);
     rVdW=0.188e-9;
     ni=(0.75*(4*3.14*rVdW^3)/3)^-1;
     %
     % this is a very simple simulation of one cluster size
     % cluster charge Q and shell radius r are guesses
     %
     qshell=[1 2 3];          % shell charge states,  inner to outer
     rshell=[r_guess-4 r_guess-2 r_guess-1 r_guess];  % shell radius
     r=(rshell(qshell(popmat(j,5)))+rshell(qshell(popmat(j,5))+1))/2;
     Qshell(1)=(4*3.14*e/3)*(0.3185)*qshell(1)*(rshell(2)^3-rshell(1)^3);
     Qshell(2)=(4*3.14*e/3)*(0.3185)*(qshell(1)*(rshell(2)^3-rshell(1)^3)+...
        qshell(2)*(rshell(3)^3-rshell(2)^3));
     Qshell(3)=(4*3.14*e/3)*(0.3185)*(qshell(1)*(rshell(2)^3-
rshell(1)^3)+qshell(2)*...
        (rshell(3)^3-rshell(2)^3)+qshell(3)*(rshell(4)^3-rshell(3)^3));
     Q=Qshell(qshell(popmat(j,5)));
     debye_length=2.8+0.2*h;                    %Debye Length in atomic radii
     Potential=exp(-r/debye_length)*Q*q/(4*3.14*epsilon*r*rVdW);    % Coulomb
potential
     vcoulomb=(2*Potential/m)^0.5;                              % Coulomb velocity
     l=1;
     PotleV=Potential/e
     while Nfull2<Ntot
        theta=3.1416*rand(1);
        phi=6.283*rand(1);
        vx=sin(theta)*cos(phi)*vcoulomb;
        vy=cos(theta)*vcoulomb;
        inition(l+Ndone2,5)=vx;
        inition(l+Ndone2,2)=vy;
        Nfull2=Nfull2+1;
        l=l+1;
     end
  end
```

```
    %
    % Hydrodynamic expansion velocities
    if popmat(j,7)==2,
      Nfull2=0;
      m=u*popmat(j,4);
      q=e*popmat(j,5);
      Te=popmat(j,3);
      % Need to add flexibility here
      load argon_hydro;
      %         rVdW=0.188e-9;
      %         ni=(0.74*8*rVdW^3)^-1;
      if Te==5,
        [A,B]=polyfit(hydro_argon_5eV(:,2),hydro_argon_5eV(:,1),9);
        hydrofit_error=B;
      end
      if Te==10,
        [A,B]=polyfit(hydro_argon_10eV(:,2),hydro_argon_10eV(:,1),9);
        hydrofit_error=B;
      end
      if Te==20,
        [A,B]=polyfit(hydro_argon_20eV(:,2),hydro_argon_20eV(:,1),9);
        hydrofit_error=B;
      end
      l=1;
      while Nfull2<Ntot
        E=rand(1)*max(hydro_argon_5eV(:,2));
        p2=rand(1);

P2=A(1)*E^9+A(2)*E^8+A(3)*E^7+A(4)*E^6+A(5)*E^5+A(6)*E^4+A(7)*E^3+A(8)*
E^2+A(9)*E+A(10);
        if P2>p2,
          theta=3.1416*rand(1);
          phi=6.283*rand(1);
          vx=sin(theta)*cos(phi)*(2*E*e/m)^0.5;
          vy=cos(theta)*(2*E*e/m)^0.5;
          inition(l+Ndone2,2)=vx;
          inition(1+Ndone2,5)=vy;
          Nfull2=Nfull2+1;
          l=l+1;
        end
      end
    end
    Ndone2=Ndone2+Ntot;
  end
  toc
```

```
size(inition)
clear B Ndone* Nfull* Ntot P1 P2 T
%
% II) Ion propagaion
tic
% Calculate TOF distribution for matrix inition
count=zeros(1,numsteps);
ionfailed=[0 0];
for i=1:size(inition,1),
   x0=inition(i,1);
   v0=inition(i,2);
   q=e*inition(i,3);
   m=u*inition(i,4);
   vradial=inition(i,5);
   xI=0;xII=0;xIII=0;vI=0;vII=0;
   % propagate ions through extraction region
   for t=0:tstep:tfinish,
      xI=x0+v0*t+0.5*t^2*(q/m)*(V1-V2)/d1;
      vI=v0+t*(q/m)*(V1-V2)/d1;
      ionfail1=0;
      if xI<0
         ionfail1=1;
         ionfailed=ionfailed+[1 0];
         break
      end
      if xI>d1,
         TauI=t;
         break
      end
   end
   % propagate ions through acceleration region
   if ionfail1==0,
      ionfail2=0;
      if abs(vradial)>(0.002/TauI)
         ionfail2=1;
         ionfailed=ionfailed+[0 1];
      end
      if ionfail2==0,
         for t=0:tstep:tfinish,
            xII=d1+vI*t+0.5*t^2*(q/m)*(V2/d2);
            vII=vI+t*(q/m)*(V2/d2);
            if xII>(d1+d2),
               TauII=t+TauI;
               break
            end
```

```
                end
            end
        end
        % propagate ions through drift region
        if ionfail2==0,
            for t=0:tstep:tfinish,
                xIII=d1+d2+vII*t;
                if xIII>d1+d2+d3,
                    TauStop=t+TauII;
                    break
                end
            end
            % bin ions by arrival time
            for j=1:numsteps,
                if TauStop==tstep*j,
                    count(j)=count(j)+1;
                end
            end
        end

    end
    ionfailed
    toc
    results=results+[0*(1:numsteps);count];
    %initials=[initials ;[inition(:,1) inition(:,2)]];
end
% Now make a histogram of ion arrival times TauStop
A=zeros(7,1);A(1)=1;B=[1/12 1/8 1/6 3/12 1/6 1/8 1/12];
posfilter=filter(B,A,inition(:,1));
velfilter=filter(B,A,inition(:,2));
resfilter=filter(B,A,results(2,:));
%figure(1);hist(posfilter,1000);
%figure(2);hist(velfilter,1000);
figure(3);plot(results(1,:),resfilter);
```

References

[1] T. Maiman, "Stimulated Optical Radiation in Ruby," Nature 187, 493 (1960)

[2] Franken, P. A., et al. "Generation of Optical Harmonics," Phys. Rev. Lett. 7, p. 118–119 (1961)

[3] D. Strickland and G. Mourou "Compression of amplified chirped optical pulses," Opt. Comm. 56, 219 (1985)

[4] T. Ditmire, E.H. Gaul, M. Martinez, "Conceptual Design Report For the Texas Petawatt Laser" http://www.ph.utexas.edu/~utlasers/papers/Petawatt_CDR.pdf

[5] A. McPherson, C.K. Rhodes et al. "Multiphoton-induced X-ray emission at 4-5keV from Xe atoms with multiple core vacancies," Nature 370, 631 (1994)

[6] T. Ditmire, M.D. Perry et al. "Interaction of intense laser pulses with atomic clusters," Phys. Rev. A 53, 3379 (1996)

[7] T. Ditmire, M.H.R. Hutchinson et al. "High-energy ions produced in explosions of superheated atomic clusters," Nature 386, 54 (1997)

[8] C. Spielmann et al. "Near-keV Coherent X-Ray Generation with Sub-10-fs Lasers," IEEE Journal of Selected Topics in Quantum Electronics, 4 249 (1998)

[9] T. Ditmire, M.H.R. Hutchinson et al. "Explosion of atomic clusters heated by high-intensity femtosecond laser pulses," Phys. Rev. A 57, 369 (1998)

[10] T. Ditmire, K.B. Wharton et al. "Nuclear fusion from explosions of femtosecond laser-heated deuterium clusters," Nature 398, 489 (1999)

[11] T. Brabec and F. Krausz "Intense few-cycle laser fields: Frontiers of nonlinear optics" Rev. Mod. Phys. 72, 545 (2000)

[12] V.P. Krainov and M.B. Smirnov "Cluster beams in the super-intense femtosecond laser pulse," Phys. Rep. 370, 237 (2002)

[13] L. V. Keldysh “Ionization in the field of a strong electromagnetic wave,” Sov. Phys. JETP 20, 1307 (1965)

[14] M.V. Ammosov, N.B. Delone, and V.P. Krainov "Tunnel Ionization of Complex Atoms and of Atomic Ions in an Alternating Electromagnetic Field," Sov. Phys. JETP 64, 1191 (1986)

[15] M.D. Perry et al. "Nonresonant multiphoton ionization of noble gases: Theory and experiment," Phys. Rev. Lett. 60, 1270 (1988)

[16] C. Wahlstrom, A. L'Huillier et al. "High-order harmonic generation in rare gases with an intense short-pulse laser," Phys. Rev. A 48, 4709 (1993)

[17] P.B. Corkum et al. "Theory of high-harmonic generation by low-frequency laser fields," Phys. Rev. A 49, 2117 (1993)

[18] E. Takahashi, K. Midorikawa et al. "Generation of 10-uJ coherent extreme-ultraviolet light by use of high-order harmonics," Opt. Lett. 27, 1920 (2002)

[19] J.-F. Hergott, P. Salieres et al. "Extreme-ultraviolet high-order harmonic pulses in the microjoule range," Phys. Rev. A 66, 021801 (2002)

[20] R. Neutze, J. Hajdu et al. "Potential for biomolecular imaging with femtosecond x-ray pulses," Nature 406, 752 (2000)

[21] T. Pfeifer et al. "Femtosecond x-ray science," Rep. Prog. Phys. 69, 443 (2006)

[22] H. Wabnitz et al. "Multiple ionization of atom clusters by intense soft X-rays from a free-electron laser," Nature 420, 482 (2002)

[23] L. G. Gouy "Sur une propriete nouvelle des ondes lumineuses," C. R. Acad. Sci. Paris 110, 1251 (1890)

[24] F. Lindner, F. Krausz et al. "Gouy Phase Shift for Few-Cycle Laser Pulses," Phys. Rev. Lett. 92, 133001 (2004)

[25] P. Balcou and A. L'Huillier "Phase-matching effects in strong-field harmonic generation," Phys. Rev. A 47, 1447 (1993)

[26] M. Lewenstein, P. Salieres, A. L'Huillier "Phase of the atomic polarization in high-order harmonic generation," Phys. Rev. A 52, 4747 (1995)

[27] P. Salieres, A. L'Huillier, and M. Lewenstein "Coherence Control of High-Order Harmonics," Phys. Rev. Lett. 74, 3776 (1995)

[28] J. Peatross, D.D. Meyerhofer "Intensity-dependent atomic-phase effects in high-order harmonic generation," Phys. Rev. A 52, 3976 (1995)

[29] P. Balcou, A. L'Huillier et al. "Quantum-path analysis and phase matching of high-order harmonic generation and high-order frequency mixing processes in strong laser fields," J. Phys. B: At. Mol. Opt. Phys. 32, 2973 (1999)

[30] M.B. Gaarde and K.J. Schafer "Quantum path distributions for high-order harmonics in rare gas atoms," Phys. Rev. A 65, 031406 (2002)

[31] Z. Chang "Single attosecond pulse and xuv supercontinuum in the high-order harmonic plateau," Phys. Rev. A 70, 043802 (2004)

[32] W.M. Wood, C.W. Siders, M.C. Downer, "Measurement of Femtosecond Ionization Dynamics of Atmospheric Density Gases by Spectral Blueshifting," Phys. Rev. Lett. 67, 3523 (1991)

[33] H.J. Shin, C.H. Nam et al. "Nonadiabatic blueshift of high-order harmonics from Ar and Ne atoms in an intense femtosecond laser field," Phys. Rev. A 63, 053407 (2001)

[34] P. Salieres, M. Lewenstein et al. "Angular distributions of high-order harmonics generated by a femtosecond laser," J. Phys. B: At. Mol. Opt. Phys. 29, 4771 (1996)

[35] J. Peatross, D.D. Meyerhofer "Angular distribution of high-order harmonics emitted from rare gases at low density," Phys. Rev. A 51, R906 (1995)

[36] T. Ditmire, M.H.R. Hutchinson et al. "Spatial Coherence Measurement of Soft X-Ray Radiation Produced by High Order Harmonic Generation," Phys. Rev. Lett. 77, 4756 (1996)

[37] J. Peatross, D.D. Meyerhofer et al. "High-order harmonic generation with an annular laser beam," Opt. Lett. 19, 942 (1994)

[38] C.F.R. Caron and R.M. Potvliege "Phase matching and harmonic generation in Bessel-Gauss beams," J. Opt. Soc. Am. B 15, 1096 (1998)

[39] R. Lopez-Martens, A. L'Huillier et al. "Amplitude and Phase Control of Attosecond Light Pulses," Phys. Rev. Lett. 94, 033001 (2005)

[40] T. Ditmire et al. "Calculation and measurement of high-order harmonic energy yields in helium," J. Opt. Soc. Am. B 13, 406 (1996)

[41] J.W.G. Tisch et al. "Measurement of the Spatiotemporal Evolution of High-Order Harmonic Radiation Using Chirped Laser Pulse Spectroscopy," Phys. Rev. Lett. 80, 1204 (1998)

[42] C. de Lisio et al. "Harmonic generation in an ionized gas medium with a 100-femtosecond, high repetition rate laser source at intermediate intensities," Appl. Phys. B 64, 323 (1997)

[43] M. Bellini et al. "Neutral depletion and beam defocusing in harmonic generation from strongly ionized media," Phys. Rev. A 64, 023411 (2001)

[44] T. Ditmire, M.D. Perry et al. "Energy-yield and conversion-efficiency measurements of high-order harmonic radiation," Phys. Rev. A 51, R902 (1995)

[45] E. Constant et al. "Optimizing High Harmonic Generation in Absorbing Gases: Model and Experiment," Phys. Rev. Lett. 82, 1668 (1999)

[46] S. Kazamias, P. Balcou et al "Global Optimization of High Harmonic Generation," Phys. Rev. Lett. 90, 193901 (2003)

[47] K. Midorikawa et al. "Phase-matched high-order harmonic generation with self-guided intense femtosecond laser pulses," RIKEN Review 31, 38 (2000)

[48] K. Midorikawa et al. "Generation of high-brightness high-order harmonics," RIKEN Review 33, 10 (2001)

[49] S. Kazamias, P. Balcou et al. "High order harmonic generation optimization with an apertured laser beam," Eur. Phys. J. D 21, 353 (2002)

[50] S. Kazamias, P. Balcou et al. "Optimization of the focused flux of high harmonics," Eur. Phys. J. D 26, 47 (2003)

[51] L. Le Deroff, P. Salieres, and B. Carre "Beam-quality measurement of a focused high-order harmonic beam," Opt. Lett. 23, 1544 (1998)

[52] Z. Liu, R. Li, Z. Xu "Intensity limits in phase-matched high-order harmonics generation," Appl. Phys. B 70, S203 (2000)

[53] P. Balcou, M. Lewenstein et al. "Generalized phase-matching conditions for high harmonics: The role of field-gradient forces," Phys. Rev. A 55, 3204 (1997)

[54] H. Mashiko, A. Suda, K. Midorikawa "Focusing multiple high-order harmonics in the extreme-ultraviolet and soft-x-ray regions by a platinum-coated ellipsoidal mirror," Appl. Opt. 45, 573 (2006)

[55] M. Schnurer et al. "Few-cycle-driven XUV laser harmonics: generation and focusing," Appl. Phys. B 70, S227 (2000)

[56] G. Tempea and T. Brabec "Optimization of high-harmonic generation," Appl. Phys. B 70, S197 (2000)

[57] F. Brandi, et al. "High-Order Harmonic Generation Yielding Tunable Extreme-Ultraviolet Radiation of High Spectral Purity," Phys. Rev. Lett. 91, 163901 (2003)

[58] G. Vaillancourt, G.A. Mourou et al. "Operation of a 1-kHz pulse-pumped Ti:sapphire regenerative amplifier," Opt. Lett. 15, 317 (1990)

[59] P.S. Banks, M.D. Perry et al. "Novel all-reflective stretcher for chirped-pulse amplification ofultrashort pulses," IEEE Journ. of Quant. Elect. 36, 268 (2000)

[60] C.G. Durfee, H.C. Kapteyn et al. "Phase Matching of High-Order Harmonics in Hollow Waveguides," Phys. Rev. Lett. 83, 2187 (1999)

[61] W.R. Grigsby Dissertation, The University of Texas at Austin (August 2007)

[62] R. Szipocs, F. Krausz et al "Chirped multiplayer coatings for broadband dispersion control in femtosecond lasers," Opt. Lett. 19,201 (1994)

[63] F. Salin, P. Georges, G. Roger, and A. Brun "Single-shot measurement of a 52-fs pulse", Appl. Opt. 26, 4528 (1987)

[64] A.E. Siegman "Lasers," University Science Books, Sausalito (1986)

[65] J. A. R. Samson and D.L. Ederer "Vacuum Ultraviolet Spectroscopy," Academic Press, London (2000)

[66] J.H. Moore, C.C. Davis, M.A. Coplan "Building Scientific Apparatus 3rd ed.," Westview Press, Boulder (2003)

[67] A.V.Vinogradov and B.Y.Zeldovich "X-ray and far uv multilayer mirrors: principles and possibilities," Appl. Opt., 16, 89, 1977

[68] Uspenskii, Vinogradov et al. "Sc–Si normal incidence mirrors for a VUV interval of 35–50 nm," Neucl. Inst. Meth. A 448, 21 (2000)

[69] E. Takahashi et al. "High-throughput, high-damage-threshold broadband beam splitter for high-order harmonics," Optics Letters 27 1920, (2002)

[70] T. Harada and T. Kita, "Mechanically ruled aberration-corrected concave gratings," Appl. Opt. 19, 3987 (1980)

[71] P. M. Paul, et al. "Observation of a Train of Attosecond Pulses from High Harmonic Generation" Science 292, 1689 (2001)

[72] Y. Mairesse, et al. "Attosecond Synchronization of High-Harmonic Soft X-rays," Science 302, 1540 (2003)

[73] L.C. Dinu, P. Agostini et al. "Measurement of the Subcycle Timing of Attosecond XUV Bursts in High-Harmonic Generation," Phys. Rev. Lett. 91, 063901 (2003)

[74] T. Sekikawa, S.Watanabe et al. "Pulse Compression of a High-Order Harmonic by Compensating the Atomic Dipole Phase," Phys. Rev. Lett. 83, 2564 (1999)

[75] E. S. Toma et al. "Ponderomotive streaking of the ionization potential as a method for measuring pulse durations in the XUV domain with fs resolution," Phys. Rev. A 62, 061801 (2000)

[76] A. Flettner, G. Gerber et al. "High harmonic generation at 1kHz repetition rate with a pulsed valve," Appl. Phys. B 73, 129 (2001)

[77] E. W. Becker, K. Bier, and W. Henkes, Z. Phys. 146, 333 (1956)

[78] O.F. Hagena and W. Obert "Cluster Formation in Expanding Supersonic Jets: Effect of Pressure, Temperature, Nozzle Size, and Test Gas," Journ. Chem. Phys. 56, 1793 (1972)

[79] O.F. Hagena "Nucleation and growth of clusters in expanding nozzle flows", Surface Science 106, 101 (1981)

[80] J. Wormer, T. Moeller et al "Fluorescence Excitation Spectroscopy of Xenon Clusters in the VUV" Chem. Phys.Lett. 159, 321 (1989)

[81] O.F. Hagena "Cluster ion sources," Z. Phys. D: At. Mol. Clusters 4, 291 (1987); Rev Sci Inst 63, 2374 (1992)

[82] F. Dorchies, V. A. Gasilov et al. "Spatial distribution of cluster size and density in supersonic jets as targets for intense laser pulses," Phys. Rev. A 68, 023201 (2003)

[83] U. Buck and R. Krohne "Cluster size determination from diffractive He atom scattering," J. Chem. Phys. 105, 5408 (1996)

[84] R. A. Smith, T. Ditmire, and J. W. G. Tisch "Characterization of a cryogenically cooled high-pressure gas jet for laser/cluster interaction experiments," Rev. Sci. Inst. 69, 3798 (1998)

[85] A.S. Boldarev, E.N. Ragozin et al. "Measurements of the xenon density in a pulsed jet from absorption of monochromatic soft X-rays," Quant. Elec. 34, 679 (2004)

[86] R.Karnbach, T. Moeller et al "CLULU: An experimental setup for luminescence measurements on van der Waals clusters with synchrotron radiation," Rev. Sci. Inst. 64, 2838 (1993)

[87] S. Kakuta, J. Matsuo "Size and energy distribution of gas cluster ion beam measured by energy resolved time of flight mass spectroscopy," Surf. & Coat. Tech. 196, 198 (2005)

[88] D. Proch and T. Trickl "A high-intensity multi-purpose piezoelectric pulsed molecular beam source," Rev. Sci. Inst. 60, 713 (1989)

[89] K.W. Madison, T. Ditmire et al. "Investigation of fusion yield from exploding deuterium-cluster plasmas produced by 100-TW laser pulses," J. Opt. Soc. Am. B 20, 113 (2003)

[90] K.W. Madison, T. Ditmire et al. "Fusion neutron and ion emission from deuterium and deuterated methane cluster plasmas," Phys. of Plasmas 11, 270 (2004)

[91] R.F. Schmalz "New Self-similar solutions for the unsteady one-dimensional expansion of a gas into a vacuum," Phys. Fluids 28, 2923 (1985)

[92] D.S. Dorozhkina and V.E. Semenov "Exact Solution of Vlasov Equations for Quasineutral Expansion of Plasma Bunch into Vacuum," Phys. Rev. Lett. 81, 2691 (1998)

[93] B.N. Breizman, A.V. Arefiev, and M.V. Fomyts'kyi "Nonlinear physics of laser-irradiated microclusters," Phys. of Plasmas 12, 056706 (2005)

[94] J.F. Sealy and E.G. Harris "Heating of a Plasma by Multiphoton Inverse Bremsstrahlung," Phys. Rev. A 7, 1064 (1973)

[95] R.D. Jones and K. Lee "Kinetic theory, transport, and hydrodynamics of a high-Z plasma in the presence of an intense laser field," Phys. Fluids 25, 2307 (1982)

[96] T.M. Antonsen, H.M. Milchberg et al. "Resonant heating of a cluster plasma by intense laser light," Phys. of Plasmas 12, 056703 (2005)

[97] W. Lotz "An Empirical Formula for the Electron-Impact Ionization Cross-Section," Zeit. fur Phys. 206, 205 (1967)

[98] M. Richter, S.V. Bobashev et al. "Photoionization Cross Sections of Kr and Xe from Threshold up to 1000 eV," X-Ray and Inner-Shell Processes: 19th Intnl. Conf. on X-Ray and Inner-Shell Proc., pp.165-171 (2003)

[99] J. A. R. Samson and L. Yin, "Precision measurements of photoabsorption cross sections of Ar, Kr, Xe, and selected molecules at 58.4, 73.6, and 74.4 nm," J. Opt. Soc. Am. B 6, 2326 (1989)

[100] H. Date, M. Shimozuma "Electron collision processes in gaseous xenon," Nucl. Inst. Meth. in Phys. Res. B 207, 373 (2003)

[101] K. Stephan and T.D. Mark "Absolute partial electron impact ionization cross sections of Xe from threshold up to 180 eV," J. Chem. Phys. 81, 3116 (1984)

[102] A.V. Phelps, "The application of scattering cross sections to ion flux models in discharge sheaths," J. Appl. Phys. 76, 747 (1994)

[103] J.S. Miller, R. Dressler et al. "Xenon charge exchange cross sections for electrostatic thruster models," Journ. of Appl. Phys. 91, 984 (2002)

[104] N.G. Adams, D. Smith, and D. Grief "Single-charge transfer reactions of the ground and metastable states of Xe(2+) at 300 K," J. Phys. B: At. Mol. Phys. 12, 791 (1979)

[105] L. Allen, D.G.C. Jones, and D.G. Schofield "Radiative lifetimes and Collisional Cross Sections for Xe I and II," Journ. Opt. Soc. Am. 59, 842 (1969)

[106] J.B. Hasted and M. Hussain "Electron capture by multiply charged ions," Proc. Phys. Soc. 83, 911 (1964)

[107] J.A.S. Barata and C.A.N. Conde, "Calculation of Drift Velocities and Diffusion Coefficients of Xe+ Ions in Gaseous Xenon," Nucl. Sci. 52, 2889 (2005)

[108] T. Ditmire, M.D. Perry et al. "Strong X-Ray Emission from High-Temperature Plasmas Produced by Intense Irradiation of Clusters," Phys. Rev. Lett. 75, 3122 (1995)

[109] Y.L. Shao, M.H.R. Hutchinson et al. "Multi-keV Electron Generation in the Interaction of Intense Laser Pulses with Xe Clusters," Phys. Rev. Lett. 77, 3343 (1996)

[110] T. Ditmire, M.H.R. Hutchinson et al. "High Energy Ion Explosion of Atomic Clusters: Transition from Molecular to Plasma Behavior," Phys. Rev. Lett. 78, 2732 (1997)

[111] H.M. Milchberg, S.J. McNaught, E. Parra "Plasma hydrodynamics of the intense laser-cluster interaction," Phys. Rev. E 64, 056402 (2001)

[112] V. Kumarappan, D. Mathur "Two-dimensional effects in the hydrodynamic expansion of xenon clusters under intense laser irradiation," Phys. Rev. A 66, 033203 (2002)

[113] S. Zamith, M.J.J. Vrakking et al. "Control of the production of highly charged ions in femtosecond-laser cluster fragmentation," Phys. Rev. A 70, 011201 (2004)

[114] T. Laarmann, T. Moeller et al. "Interaction of Argon Clusters with Intense VUV-Laser Radiation: The Role of Electronic Structure in the Energy-Deposition Process"

[115] B.F. Murphy, T. Ditmire et al. "Explosion of Xenon Clusters Driven by Intense Femtosecond Pulses of Extreme Ultraviolet Light," Phys. Rev. Lett. 101, 203401 (2008)

[116] C. Bostedt, T. Moeller et al. "Multistep Ionization of Argon Clusters in Intense Femtosecond Extreme Ultraviolet Pulses," Phys. Rev. Lett. 100, 133401 (2008)

[117] C. Siedschlag and J.M. Rost "Enhanced ionization in small rare-gas clusters," Phys. Rev. A 67, 013404 (2003)

[118] S. Namba, K. Nagashima et al. "Enhancement of Double Auger Decay Probability in Xenon Clusters Irradiated with a Soft-X-Ray Laser Pulse," Phys. Rev. Lett. 99, 043007 (2007)

[119] B. Ziaja, T. Moeller et al. "Atomic clusters of various sizes irradiated with short intense pulses of VUV radiation," Eur. Phys. Lett. 82, 24002 (2008)

[120] I. Georgescu, U. Saalmann, J.-M. Rost "Attosecond Resolved Charging of Ions in a Rare-Gas Cluster," Phys. Rev. Lett. 99, 183002 (2007)

[121] A.A. Sorokin, M. Richter et al. "X-ray-laser interaction with matter and the role of multiphoton ionization: Free-electron-laser studies on neon and helium," Phys. Rev. A 75, 051402 (2007)

[122] G.M. Petrov and J. Davis "Impact of the laser wavelength on the dynamics of Xe cluster plasma produced by an intense ultrashort laser pulse," Phys. of Plasmas 13, 0333106 (2006)

[123] W.C. Wiley and I.H. MacLaren "Time-of-Flight Mass Spectrometer with Improved Resolution," Rev. Sci. Inst. 26, 1150 (1955)

[124] M. Lewerenz. J.P. Toennies et al "A new scattering deflection method for determining and selecting the sizes of large liquid clusters of 4He," Chem. Phys. Lett 206, 381 (1993)

[125] R.P. Drake "High Energy-Density Physics," Springer (2006)

[126] U. Saalman and J.-M. Rost "Ionization of Clusters in Strong X-ray Laser Pulses," Phys. Rev. Lett. 89, 143401 (2002)

[127] C. Siedschlag and J.-M. Rost "Small Rare-Gas Clusters in Soft X-ray Pulses," Phys. Rev. Lett. 93, 043402 (2004)

[128] A.A. Sorokin, M. Richter et al. "Photoelectric Effect at Ultrahigh Intensities," Phys. Rev. Lett. 99, 213002 (2007)

[129] S.J. Gitomer et al. "Fast ions and hot electrons in the laser-plasma interaction," Phys. Fluids 29, 2679 (1986)

[130] L.M. Wickens, J.E. Allen, P.T. Rumsby "Ion Emission from Laser-Produced Plasmas with Two Electron Temperatures," Phys. Rev. Lett 41, 243 (1978)

[131] R. Decoste, B.H. Ripin "High-Energy Ion Expansion in Laser-Plasma Interactions," Phys. Rev. Lett. 41, 24 (1978)

[132] Y. Shima and H. Yatom "Inverse bremsstrahlung energy absorption rate," Phys. Rev. A 12, 2106 (1975)

Vita

Brendan Francis Murphy was born in 1976 in Ithaca, New York, the son of Peter and Mary Murphy. After graduating Reed College in Portland, Oregon in 1997, Brendan worked in the accelerator control room of the Stanford Linear Accelerator Center (SLAC) during the final operations of the SLC and the commissioning and operations of the PEP-II storage rings. In 2001 Brendan joined the Gun Task Force RF photocathode electron gun effort at SLAC in support of LCLS photoinjector development. In 2003 Brendan joined Todd Ditmire's research group at The University of Texas at Austin.

Permanent address: 5514 Woodrow Ave, Austin, TX 78756

This dissertation was typed by the author.